UNIVERSITY OF BELGRADE

FACULTY OF MECHANICAL ENGINEERING

Mohamed Abduljawad Higaeg

OPTIMIZATION OF COMPOSITE HORIZONTAL AXIS WIND TURBINE BLADE ON THE BASIS OF FLUID-STRUCTURE INTERACTION ANALYSIS

DOCTORAL DISSERTATION

BELGRADE, 2020

УНИВЕРЗИТЕТ У БЕОГРАДУ

МАШИНСКИ ФАКУЛТЕТ

Мохамед Абдуљавад Хигаег

ОПТИМИЗАЦИЈА КОМПОЗИТНЕ ЛОПАТИЦЕ ВЕТРОТУРБИНЕ СА ХОРИЗОНТАЛНОМ ОСОВИНОМ НА ОСНОВУ АНАЛИЗЕ ИНТЕРАКЦИЈЕ ФЛУИДА И СТРУКТУРЕ

ДОКТОРСКА ДИСЕРТАЦИЈА

БЕОГРАДУ, 2020

SUPERVISOR :

Dr. Aleksandar Grbović, full professor
University of Belgrade, Faculty of Mechanical Engineering

BOARD OF COMMISSION

Dr. Aleksandar Simonović, full professor
University of Belgrade, Faculty of Mechanical Engineering
.....

Dr. Igor Balać, full professor
University of Belgrade, Faculty of Mechanical Engineering
.....

Dr. Petar Uskoković, full professor
University of Belgrade, Faculty of Technology and Metallurgy
.....

Data of defence ……

DEDICATION

To my father's immaculate spirit, my mother, my wife, my daughters, sons, to my brothers and sisters for their boundless support, my teachers, and
to spirits Libyan rebels and heroes,
I dedicate this thesis

ACKNOWLEDGMENT

I would first to thank the God without whom nothing is possible.

I would like to express my sincere gratitude and fully thanks to my supervisor **Dr. Aleksandar Grbovic**, full professor for his offers continuous support to the thesis guides and revision of my research.

I would like to thank **Dr. Igor Balać**, full professor for sharing his knowledge and experience.

I would also like to extend my gratitude to the staffs of Mechanical Engineering faculty and my friends whose help was very valuable in this research.

Finally, my deep appreciation is addressed to whole my family my mother, wife, daughters and sons for their patience and supporting me during the period of my study.

Abstract

Recently, the world demand has been increased of the energy through a rise of human life level. The results of the oil price raise and its environment influence, the scientific researches have been performed on the renewable energy as the alternatives of fossil fuels which are the wind energy one of renewable energy applications and it is the most promising sources of the renewable energy.

The wind energy is converted into mechanical power through blades which are the most vital component of wind turbine. Blades play a major part in wind turbines and they have more potential of the wind turbine efficiency/performance improvement to capture a more energy from wind. The efficiency of wind turbine blades depends on the number of factors (such as the blade shape and material) where the blade shape controls the aerodynamic characteristics and the pressure distribution in service. The most important parameters of the blade material are to be high stiffness, low density and long hypothetical life. Nowadays, the composite materials have been used for a fabrication of the wind turbine blades to reduce the blade weight in turn decreasing the gravity effect load.

A fluid flows over the blades structure surface creates a pressure loads result in the blade structures to deform. This deformation leads new boundary for the domain of flow. A numerical modelling technique is applied to estimate flow induced deformation and its sequel, so the system coupling simulations of fluid-structure interaction are required for optimization composite wind turbine blades. In addition, wind turbine blades should be a focus as they are faced with deformation in the real implementations. In this thesis, the wind turbine blades are discussed comprehensively. a computational fluid dynamics (CFD), finite element analysis (FEA), the one-way and two-way system coupling of fluid-structure interaction (FSI) simulations of the composite wind turbine blade are implemented.

The CFD simulations are implemented by selection of the k-w shear stress transport (SST) turbulence model for the CFD simulation of initial pressure load and the fluid-structure interaction (FSI) simulation. The one-way FSI simulations were conducted for the five predefined composite materials at cut-out wind speed 25 m/s (when pressure load acting on the wind turbine blades is maximum) to compare the results and define the optimum composite material based on the values of stress and deformation obtained. It was found that the most appropriate composite material is the Aramid (kevlar49)/Epoxy 5505. The finite element analysis was then used to test the tensile stiffness of composite laminate of the Aramid (kevlar49)/Epoxy 5505 based on the lay-up's sequences of composite material at the maximum and minimum thickness the blade sections. The models of specimens used in this simulation were created according to ASTM standard D638-14 and the results of the simulation showed that both specimens have enough tensile stiffness.

The finite element analysis was again applied to study the effect of micro-scale structural low-level porosity on strength of structural materials using the 3-D unit cell numerical model (UCNM). The comparison has been performed of the obtained values for the stress concentration factor (SCF) for different size and shape of pore with available experimental data in literature. The values of normalized strength obtained by utilizing UCNM agree with available experimental data published in literature. It was confirmed that material porosity in form of closed pores has notable influence on strength of structural materials. Less porosity in the material microstructure generally leads to higher values of material strength. For fixed porosity volume fraction, shape of pores has an impact on strength of structural material.

For selected composite material, the one-way system coupling FSI simulations were then performed for several speeds between the cut-in and the cut-out wind speed, and then results of simulations were analysed through the comparison of normal stresses, shear stresses, blade deformations, force reactions, and moment reactions. The results are presented in the terms of the

normal stress distribution, shear stress distribution, and blade deformation with defined positions of the maximum values on the blade structure. While the force and moment reaction are demonstrated the maximum values and directions. Then these analyses of the simulations results were plotted for each parameter separately to describe the trend lines of those parameters and how are represented the trend line of parameter through increasing the wind speed. The maximum values of the normal stress and shear stress were compared with the ultimate strength of the composite laminate and found reasonable. The maximum tip blade deformation was obtained at the maximum pressure load which occurs in the cut-out wind speed 25 m/s less than the recommended allowable deformation value of 10% of the blade length. According to the simulations results this wind turbine blades work in the safety mode for the operating conditions applied in this study.

Finally, the two-way fluid-structure interaction simulation was implemented only at the cut-out wind speed because the maximum pressure load occurs at this wind speed; moreover, this kind of simulation needs a computer with high specifications (such as huge amount of space on hard disc during the computations and a big space for results' storage). Obtained results for two-way simulation were compared to the results from the one-way fluid-structure interaction simulation results. The two-way FSI simulation results show the distribution of the normal stress, shear stress, and blade deformation on the structural blade surface are the same in the one-way FSI simulation results but the maximum values have been raised a little. Based on the fluctuations charts obtained from the values of the normal stress, shear stress, and blade deformation it can be noticed that values fluctuated over the complete time step and that maximum fluctuations occurred during first 40% of simulated time and then values varied much less during next 60% of time, reaching more or less stable values. However, the maximum normal stress and shear stress values obtained in the two-way FSI are reasonable compared to the ultimate strength of laminate composite material applied; also, the maximum tip deformation is less than the recommended allowable deformation value of 10% the blade length. So, the wind turbine blade is on the safety side with respect to operating conditions utilized in this study.

The comparison of the FSI/FEA results and values from the literature/experiments showed good agreement, with room for further improvements in both directions: experimental and numerical.

Keywords: Fluid-Structure Interaction (FSI), Finite Element Analysis (FSA), Strength of Composites, Numerical Modelling, Porosity of Structural Materials, Stresses, Deformation.

Scientific discipline: Mechanical engineering

Scientific subdiscipline: Wind Turbine Design

UDK number: 621.548:66.018.9(043.3)

АПСТРАКТ

Последњих је година дошло до повећања потражње за енергијом махом због пораста животног стандарда људи широм света. Услед поскупљења нафте и њеног лошег утицаја на животну средину, научна истраживања се данас усмеравају ка обновљивим изворима енергије који би требало да замене фосилна горива, а међу њима се енергија ветра издваја као најперспективнији извор обновљиве енергије.

Енергија ветра се претвара у механичку снагу помоћу лопатица које представљају најважније компоненте ветротурбина. Уз то, лопатице имају највише „потенцијала“ да се путем њиховог правилног пројектовања и оптимизовања побољшају ефикасност и перформансе ветротурбина у смислу добијања што више енергије од ветра. Ефикасност лопатица ветротурбине зависи од бројних фактора (међу којима су главни геометрија и материјал лопатице), при чему облик лопатице највише утиче на аеродинамичке карактеристике, тј. расподелу оптерећења у виду притиска. Материјал лопатице мора имати високу крутост, малу густину (масу) и, пожељно је, дуг век. Данас су композитни материјали најчешће користе за израду лопатица ветротурбина како би се добила што мања маса, а тиме и мање оптерећење услед инерцијалних сила.

Ваздух који опструјава површине лопатица ствара еластичне деформације њихове структуре. Услед ових деформација распоред струјница се мења, а тиме и расподела притиска током времена. За процену вредности деформација лопатица изазваних протоком ваздуха данас се примењују нумеричке методе, а за оптимизацију композитних лопатица ветротурбина неопходно је спровести сложене симулације интеракције самог флуида и структуре. Стога је у овој докторској тези понашање композитне лопатице ветротурбине са хоризонталном осовином детаљно истражено коришћењем прорачунске динамике флуида (ПДФ) и методе коначних елемената (МКЕ) коришћењем једносмерно и двосмерно спрегнутих симулација интеракције флуида и композитне структуре.

ПДФ симулације спроведене су коришћењем к-ω модела турбуленције (енг. *shear stress transport model (SST)*) и за симулацију почетног оптерећења у виду притиска и за симулацију интеракције флуида и структура (ИФС). Пет једносмерних ИФС симулација за пет дефинисаних композитних материјала лопатице је спроведено, а за брзину ветра је усвојено 25 м/с јер се тада појављује максимално оптерећење у виду притиска, па се при тој брзини ветротурбина мора искључити. Резултати су упоређени и на основу добијених вредности нормалних напона и напона смицања, те еластичних деформације лопатице, усвојен је најоптималнији случај. Композитни материјал који је усвојен је Арамид (Кевлар 49)/Епокси 5505. Потом је коришћењем МКЕ испитана зависност затезне чврстоћа композитног ламината од Арамид (Кевлар 49)/Епоксија 5505 од начина слагања слојева композитног материјала у областима максималне и минималне дебљине лопатице. Моделиране су стандардне епрувете према АСТМ стандарду Д638-14 и нумеричка анализа је показала да ламинати на оба места узорка показују задовољавајућу затезну чврстоћу.

Анализа коначних елемената је поново примењена је да би се проучио и утицај (на микро нивоу) степена порозности на чврстоћу изабраног композитног материјала коришћењем 3-Д нумеричког модела јединичне ћелије (енг. *3-D unit cell numerical model UCNM*). Упоређене су добијене вредности фактора концентрације напона (ФКН) за различите величине и облик пора са доступним експерименталним подацима из литературе. Вредности нормализоване чврстоће добијене употребом UCNM -а слажу се са доступним експерименталним подацима објављеним у литератури. Потврђено је да порозност материјала у облику затворених пора има приметан утицај на чврстоћу композитног материјала. Мања порозност у микроструктури материјала обично доводи до већих

вредности чврстоће материјала. За фиксни запремински удео порозности, и облик пора има утицај на чврстоћу композитног материјала.

За изабрани композитни материјал потом су спроведене једносмерне ИФС симулације за неколико изабраних брзина ветра између брзине укључивања и брзине при којој се прекида рад ветрогенератора, а затим су анализирани резултати симулација путем поређења вредности нормалних напона, напона смицања, еластичних деформација лопатице и реакција ослонаца. Резултати су приказани у виду расподеле нормалних напона, напона смицања и еластичних деформација лопатице са јасно назначеним положајима максималних вредности на структури лопатице. Реакције веза (силе и моменти) приказану су преко максималних вредности и праваца деловања. За поменуте резултате направљени су графови њихових вредности у функцији брзине ветра да би се идентификовале и описале линије трендова са повећањем брзине ветра. Максималне вредности нормалног напона и напона смицања упоређене су са затезном чврстоћом композитног ламината и утврђено је да су у дозвољеним границама. Максимална деформација врха лопатице је добијена за максимално оптерећење при брзини ветра од 25 м/с и мања је од препоручене вредности деформације (10% од дужине лопатице). Према резултатима нумеричких симулација, пројектована лопатица ветротурбине ради у безбедном режиму за радне услове примењене у овом истраживању.

Коначно, двосмерна симулација интеракције флуида и структуре спроведена је само при брзини ветра када се ветротурбина искључује јер је тада највеће оптерећење лопатице; штавише, за овакву врсту симулације потребан је рачунар супер карактеристика са великим простором на тврдом диску током прорачуна и довољно великим простором за складиштење резултата, па је и из тог разлога симулација изведена само за максималну брзину ветра. Добијени резултати су упоређени са резултатима из једносмерних симулација интеракције флуида и структуре лопатице. Резултати двосмерне ИФС симулације показују сличну расподелу нормалног напона, напона смицања и еластичних деформација лопатице као код једносмерних ИФС симулација, али су максималне вредности нешто више. На основу добијених графикона промена вредности напона и деформација током посматраног временског интервала може се рећи да веће флуктуације вредности постоје током првих 40% времена, а да су потом доста мање, те да напони и деформације достижу више-мање стабилне вредности. Максималне вредности нормалног напона и напона смицања напона добијене у двосмерној ИФС анализи су у дозвољеним границама у односу на затезну чврстоћу примењеног композитног материјала ламината, док је максимална деформација врха лопатице поново мања од препоручене вредности деформације (10% дужине лопатице). На основу тога је изведен закључак да се је пројектована лопатица потпуно безбедна у радним условима ветротурбине.

Поређење резултата ИФС анализе, као и анализе коначним елементима, са постојећим подацима из литературе и експеримента показује добра поклапања, са простором за даља унапређења како у погледу нумерике, тако и у погледу експерименталних истраживања.

Кључне речи: међусобна интеракција флуида и структуре (ИФС), анализа коначним елементима, чврстоћа композита, нумеричко моделирање, порозност структурних материјала, напони, деформације.

Научна дисциплина: Машинско инжењерство

Научна под дисциплина: Пројектовање ветрогенератора

List of Contents Page

List of Figures

List of Tables Page

CHAPTER ONE
INTRODUCTION AND LITERATURE REVIEW

1.1 Introduction

1.1.1 Global Wind Capacity

Wind energy is the ones of the renewable energy applications, it is an abundant and permanent resource, compared solar energy, and utilization couldn't be affected by environment. Wind turbine is a machine to extract wind energy and transforming to mechanical energy and later convert to electrical energy. Figure (1.1) demonstrates the growth rate of wind energy generating capacities, which has significantly risen in the last ten years. The total capacity of wind power generators installation was 539,581 MW at the end of 2017 (World Wind Energy Report 2017).

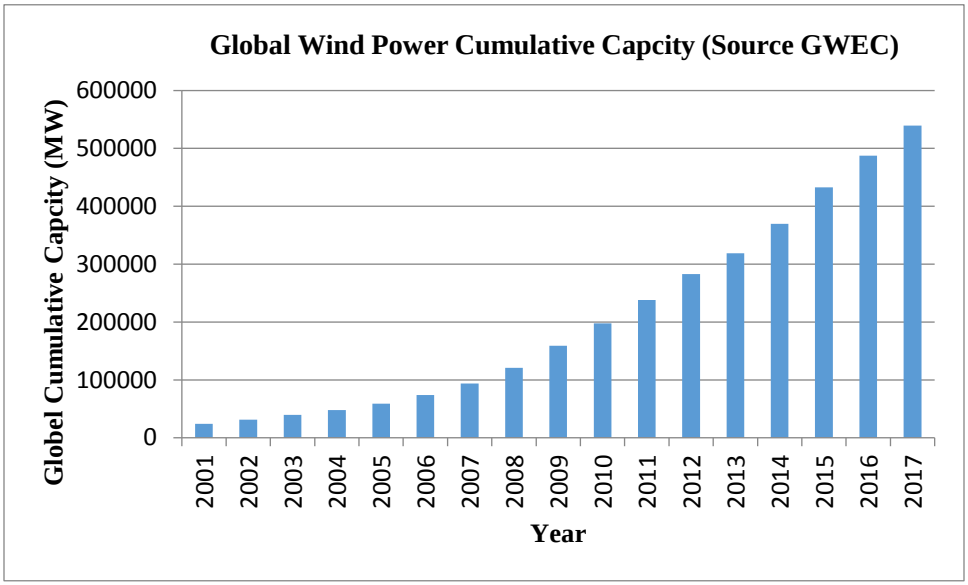

Figure (1.1) Global Wind Power Cumulative Capacity [1]

In additional, the cumulative wind energy capacity of main countries by December 2017 is described in figure (1.2). From that figure, it is a clear shown that the China is the first country which using renewable energy then the USA comes in the second step. Moreover the American Wind Energy Association, the current installed capacity of wind energy by the end of 2015 in the US is approximately 73992 MW (U.S.A, 2016).

1.2 Technology Wind Turbine History

Wind energy has accompanied mankind for most of its history. At about 3100 B.C. Egyptians were using sails of linen or papyrus to propel small boats southward against the stream of river Nile, and sailboats were replaced only many centuries later by steamboats [2]. From this initial use as boat propulsion, wind energy later became also source of mechanical power. The first windmills appeared in the Persian region of Sistan, between seventh and ninth century [3]. From there windmills spread to central Asia and later in China and India [4]. Windmills started to be used in northwestern Europe during the twelfth century [5].

The first windmill in Europe was built in England in 1137 by William of Almoner, of leicester. The original design, called post-mill, where the whole tower rotates to face the wind, is thought to be developed independently from the carousel design used in Persia and most likely inspired by the design of waterwheels. From England, post-mills spread in the rest of Europe in a west-to-east direction; in the

1300s windmills were used in Spain, France, Belgium, the Netherlands, Denmark, the German principalities and the Italian states. As they became more common, windmills became also bigger and their design had to be improved for that; hence the tower-mill design was developed, where only the upper part of the tower with the sails, the wind shaft and the brake wheel rotate to the wind [2].

In American windmill design was developed during the 19th century by D. Halladay (1854) and by Reverend L. H. Wheeler (1867) [5]. Light, small, movable self-regulating, cheap and easy to maintain, these windmills were used for grain grinding and water pumping across the West plains. Railroad companies were the first users of Halladay's windmills, used to supply water to steam locomotives [2].

About two decades later, in winter 1887-1888 in Ohio, US Professor Charles F. Brush built a massive 12 kW wind turbine, with a rotor diameter of 50 meters and 144 rotor blades figure (1.2).The machine served for twenty years, until Brush decided to take down the sails in 1908 [2].

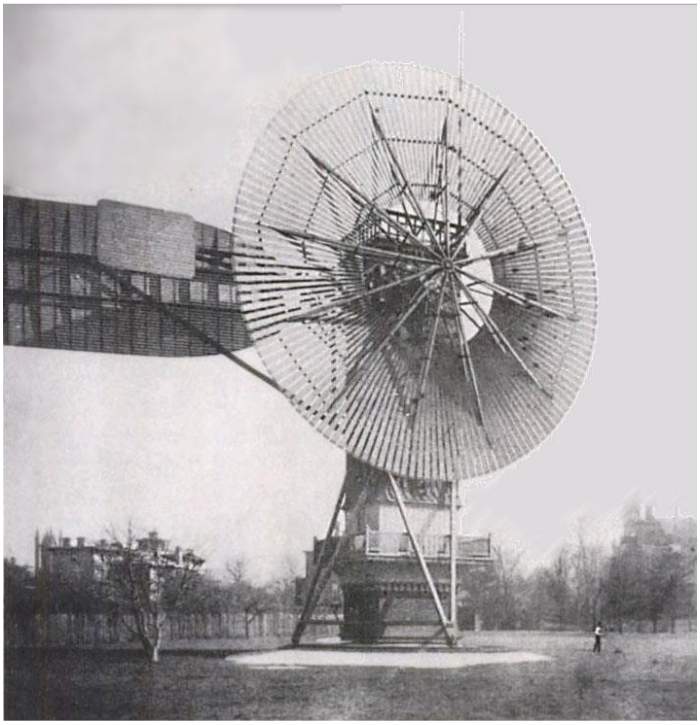

Figure (1.2): C. Brush's wind turbine [2]

In 1890s, danish scientist Poul la Cour began test on wind turbines, he was the first to discover that a fast rotating wind turbine with fewer blades is more efficient in electricity production. In 1903 he founded the Society of Wind Electrician, with the first course held the following year [7]. Commercial use of wind power had to wait until 1927, when Joe and Marcellus Jacobs opened in Minneapolis the Jacobs Wind factory, selling wind turbines used on farms to charge batteries and power lighting.

Year 1941 saw the first megawatt-size wind turbine, the Smith-Putnam wind turbine, installed at Grandpa's Knob, Castelton,Vermont. It was a two-bladed, variable pitch, downwind wind turbine, with a 53-meters diameter rotor and 1.25 MW power output as shown in the figure (1.3).

In 1956 la Cour's student Johannes Juul built in Gedser, Denmark a three-bladed, upwind wind turbine capable of 200 kW inspiring the design of later wind turbines. He is also the inventor of the emergency aerodynamic tip brake. The turbine run for eleven years and was refurbished in the mid1970s at the request of NASA.

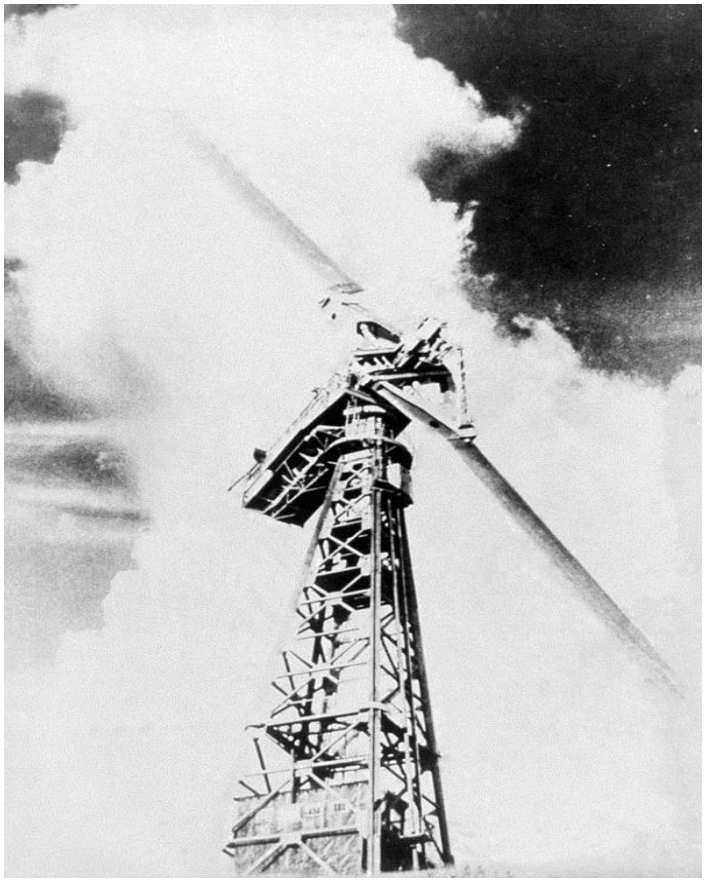

Figure (1.3): Smith-Putnam wind turbine [8]

At these days, the Vestas V164 8.0 MW is the world's biggest offshore wind turbine, the turbines were installed in early 2016 in Maade, Denmark. With height of 220 meters and three blades for its 164-meters wide rotor [9].

1.3 The Wind Turbine Classification

Wind turbines are the most important part of the wind energy industry. A wind turbine is a machine which is converted the wind kinetic energy to electrical power [10]. The horizontal axis wind turbine (HAWT) and the vertical axis wind turbine (VAWT) are classified or differentiated by the axis of rotation of the rotor shafts. Horizontal axis wind turbines, also known as HAWT type turbines have a horizontal rotor shaft and an electrical generator which is both located at the top of a tower. Vertical Axis wind turbines- abbreviated as VAWTs, are designed with a vertical rotor shaft, a generator and gearbox which are placed at the bottom of the turbine, and a uniquely shaped rotor blade that is designed to harvest the power of the wind no which direction is it blowing [11]. Figure (1.4) and figure (1.5) show examples of Horizontal axis wind turbine (HAWT) and Vertical axis wind turbine (VAWT) respectively. Figure (1.4) is a wind farm installed with three-bladed HAWTs and figure (1.5) is a VAWT wind farm using Darius type VAWTs [11].

Figure (1.4) An example of on-shore HAWT wind farm [12]

Figure (1.5) an example of Darius type VAWT wind farm [13]

1.4 Wind Turbine Blade

1.4.1 Blade Airfoil Selection

For horizontal axis wind turbines, it is recommended to have a higher lift but lower drag airfoil. There are many kinds of airfoil including the general aviation airfoil, such as NACA series, which are still used in some wind turbines. However, with the development of wind turbines, the dedicated airfoil came about. The S series designed by NREL in USA, is mostly used in stall-regulated wind turbines for its gentle behavior in stall conditions; the FFA W series designed in Sweden and RIS series designed in Denmark, are preferable for lower Reynolds applications, and the DU series designed in Netherland, is popular in High Reynolds for large wind turbines. Each of these series has its own airfoil shape with different thickness-to-chord ratio of 18%-40%. The thicker airfoil shapes are often located at the inner part (close to rotor center) of the blade while the thinner ones are set in the outer part of the blade due to ease of manufacturing and better strength and stiffness [14].

Several research and investigations have been conducted to design and improve the airfoil performance for wind turbine blades over the years by laboratories, scientists, and technical institutions such as: NREL, Risø, Delft, Martin Hepperle MH, Althaus AH, Wortman FX, and Selig Giguere SG. Below, brief information about some of the famous airfoil developers and their airfoil designs are discussed with key characteristics [15].

In Ref. [16] it was researched on "Aerodynamic Design 2.5 MW of Horizontal Axis of Wind Turbine Blade in Combination with CFD Analysis." The blade geometry of 2.5 MW was designed for length 47.096 m with the DU series and NACA 64-618 of airfoils. The main objective of this study was mentioned for improvement of the blade power performance. The blade model of the fluid dynamic design is used the BEM theory as the base. CFD modeling simulation was implemented by utilizing ANSYS fluent workbench V 13.0 in combination with the ANSYS ICEM CFD meshing tool. The results were obtained according to the tip speed ratio. The inlet air velocity was defined at 5 m/s and

the angular speed was applied at a varied speed range from 3 to 12.17 rpm. The results shew the generated power attained around 2.6 MW which is the rated of power generation at the rated angular speed 12.17 rpm. According to results obtained of the aerodynamic design, optimization can be confirmed in well done.

In Ref. [17] it was carried out a research on "a New Method for Horizontal Axis Wind Turbine (HAWT) Blade Optimization." this paper proposes optimization seven cases of wind turbine blades for small and medium scales in the different blade radius of each case, the rotor blade radius of seven case study are 4.5 m, 6.5 m, 8 m, 9 m, 10 m, 15.5 m and 20 m. the first studying stage is executed utilizing a single airfoil NACA 63-215 for whole the blade. For the second studying stage, each blade at cases study is split into three portions and each of the blade portions is used specific airfoil. Supplying all necessary data and appropriate of the airfoils inclusive 43 airfoils are elicited and their experimental data are used as input of the optimization procedure. The variable parameters in the optimization procedure are airfoil type, attack angle, and chord, where the studying goal is an estimation of maximum torque. The MATLAB code wrote for the design and optimization of the blade which was compared and confirmed that by the experimental data. The results describe a dramatic grow for the first studying stage which was the blade design with the single airfoil where the two-variable influences optimization 7.7% to 22.27 % raise and three-variable optimization causes (second studying stage) 17.91% up to 24.48% rise in output torque.

In Ref. [18] it was researched on "Aerodynamic optimal design of wind turbine blades using a genetic algorithm." The integrated Genetic Algorithm (GA) and modified blade element momentum theory have utilized to investigate the aerodynamic optimization of the wind turbine blade. For improvement of the generate power at the same blade length, the optimization method selected the GA. the design parameters such as chord length, twist angles and position of airfoils are deemed variables. The BEM theory applied for aerodynamic analysis of the wind turbine blades. The most important in this research is an aerodynamic analysis of the case study. unlike different aerodynamic studies which are an easy geometry of wind turbines, this case study of the wind turbine blade was designed with more complex, because it contained vary of airfoils type, where were twisted and tapered along the blade length. Results are obtained by selection optimized variables, the generated power can raise by 10% compared to the base design in corresponding wind speed.

In Ref. [19] it is a scientific paper research on "Modeling and aerodynamic analysis of small scale, mixed airfoil HAWT blade: A Review." in this scientific paper, the design steps compose of a choosing the proper airfoil and advantages of a mixed airfoil over a simple airfoil. Blade Element Momentum (BEM) theory is used to perform the aerodynamic analysis for the determination of the optimization torque and power. The techniques have used of decreasing weight and raising power performance by the selection of thin airfoil with a short chord length. The wind turbine blade is designed by mixed of three different airfoils which are SG6041, SG6050, and SG6043. the three airfoils were selected for this design and placed in the last third of the blade to be in the result a thick blade, the new design by the mixed airfoil has better than the simple design over blade length that gives the blade has increased in strength with raise of the tip speed ratio. The power coefficient curve was smoothly increased for the blade which used the mixed airfoils.

In Ref. [20] it was researched on **"**Investigation of blade performance of horizontal axis wind turbine based on Blade Element Momentum Theory (BEMT) using NACA airfoils". The chosen of an airfoil is the most significant goal of effective wind turbine blade designing. Grifith, (1977) presented that the power generated is influenced by the airfoil lift-to-drag ratio, however, Hassanein, (2000) advised the chosen airfoil should be based on its position along the blade to be sure it contributes the increasing overall performance. In this paper presents that, the investigation of blades elements have a constant

lift-to-drag ratio identically. In this study, two different NACA airfoils have been selected one is four-digit and the other five-digit. The results show the highest power coefficient for elements at vary of r/R ratio from 0.3 to 0.6.

In Ref. [21] it was conducted research on "Design and Performance Analysis of Small Scale Horizontal Axis Wind Turbine for Nano Grid Application." the selection of proper airfoil for small wind turbine blades has considered some parameters to be preserved like thickness, lift and drag coefficients, blade root stiffness,...etc. practically the wind tunnel is used of testing airfoils Reynolds numbers range and surface conditions. Usually, in small wind turbine applications are not used the mixed airfoils. While this research describes that, the mixed airfoils of wind turbine blades have succeeded to generate satisfying performance in small wind turbine systems.

In Ref. [22] it is scientific paper research on **"**Design of Multiple Airfoil HAWT Blade Using MATLAB Programming." The MATLAB code has used for the development of the three-blade wind turbine. The blade momentum theory has applied to the blade modelling code. The blade geometry was designed with mixed airfoils which are NACA 4412, NACA 2412 and NACA 1812 for the blade root, primary and blade tip respectively. The airfoils were selected for wind turbine blades because it is performance an excellent at low Renold's number. the wind turbine rotor diameter is 4.46m and the design of wind speed 5 m/s to achieve power coefficient 0.49 and rated power 560 W. the results of the analysis show that the power coefficient can be achieved as mentioned above at the tip speed ratio is 7 and the power generated is 583.4 W at rotational speed of 150 rpm.

In Ref. [23] it is scientific research carried out on **"**Aerodynamic Design and Structural Analysis Procedure for Small Horizontal-Axis Wind Turbine Rotor Blade." The small horizontal axis wind turbine (HAWT) blades combined the NREL S-Series airfoils, that airfoils are designed for small wind turbine blades and generator connected agreed with the CPWPRC specifications very well. The blade airfoils are selected with S822 and S823 airfoil for the outer and root sections of the new blade, respectively. The HAWT blade aerodynamic performance is affected by the tip speed ratio as the main design factor. The tip speed ratio has been selected around 7 for increasing the performance and at the same time does not create great centrifugal and aerodynamic stresses. In this procedure, the blades are patterned for achieving the suitable lift force desired for the generator to work at high capacity in conditions of low wind speed.

In Ref. [24] it is scientific research performed on "Blade Performance Analysis and Design Improvement of a Small Wind Turbine for Rural Areas." One's of the studying points in this research that, the airfoil chosen is a conclusive design variable and according to that four various configurations has defined within the NACA airfoil family. The results have been acquired with the generality of them negative excluding the configuration which uses the NACA 4415 for the entire blade, and that configuration has achieved 10.2% useful energy during a year.

1.4.2 Blade Materials

The composite is defined to combine two materials or more maintaining their macro-structure, produced material which combine by two or more material has used to improve properties as resultant for compared to the main constituents. Structure of composite materials is formed as a material of reinforcement and matrix. The reinforcement material supplies mechanical strength and transfers most loads in the composite, and the matrix material function to preserve alignment or spacing of reinforcement material and environment impact. a reinforcement material can combine with a proper matrix material for producing lightweight material or make other singular properties related to monolithic materials such as metals and supplying similar or better performance properties. There are

different processes can be used for the manufacturing of the composites because there are a variety of composite materials and their compositions. [25].

"Cellulose and lignin are combined to form wood and has been the prevalent building material for a long in many engineering applications. Woods have a good prospect for applied according to their low density, while woods stiffness is low which can be difficult for deflections limitation in the large rotor blades. Cellulosic fibers of the wood materials which have aligned in the direction of loads, reaching mostly the maximum performance of wood. for the reasons the wood is a natural material and attracting environmentally, however, it could not find in high quality and reproducible possibility, that is the needs of stable and economic manufacturing of wind turbine blades and making them economically attractive to wind energy. [26].

A wood has improved by thin sheets and it is not galvanized steel be common using. based on high weight and low fatigue to alloy steel has not been applied for wind turbine blades, in spite of, it was to be the optimal selection in the past for blade manufacturing. But undue steel weight has shown many problems in applications thence an Aluminum is used but through the applications shew many problems such as low fatigue resistance and high cost. Later, a composite of fiber-reinforced plastic (FRP) has been used widely for wind turbine blades. The wind turbine blade material should meet many requirements as properties in detail lightweight, high strength resistance and long fatigue life. Additional, material should have good resistance to aerodynamic inertia and environmental influence such as dust particles accumulation. [27].

In Ref. [28] it is research study on "Experimental Investigation on Mechanical Behaviour of E-Glass and S-Glass Fibre Reinforced with Polyester Resin." composites of glass fibre reinforced polyester has governed a role for a long time in a different of implementations because it has high specific strength, modulus, and stiffness. The E glass fibre and S glass fibre with random aligned reinforced polymer composite were improved with manual mode techniques at a different fibre volume fraction. The research investigation was implemented for E Glass-Polyester (E-P) and S Glass –Polyester (S-P) composite and comparing these results to mechanical properties with a composite is combined of E Glass and S Glass-Polyester (ES-P). The effect of glass fibre volume fraction on mechanical properties was surveyed for tensile strength, flexural strength, and impact strength. The results describe a noteworthy development in the mechanical properties of the manufactured composite with a raise in glass fibre contents. In addition, the results describe the better appropriate of fibre resin ratio relate to strength.

In Ref. [29] it was carried out research on "Design and Analysis of Horizontal Axis Windmill Turbine Blade." composite materials have been used widely in different Engineering applications because it has eminent mechanical properties such as high strength, lightweight, high stiffness, high fracture toughness, low thermal conductivity, high erosion resistance ....etc. the wind turbine blade exposed to different types of loadings during the operational and parking stage. Recently, the composite blades fabricate of glass fiber composites, however, the carbon fiber composite has been utilized in these years. In the research investigation, the wind turbine blade was designed by utilizing pro-E (creo-5.0) and the ANSYS software package executed for the static analysis. The analysis of four various composite material was counted as follows, carbon/Epoxy, E Glass/Epoxy, Carbon-Sic/Epoxy, and Al-Sic/Epoxy. Experimental Results of comparison of the investigation in terms of stresses, deformations, stiffness and percentage weight saving are emphasized that the Al-Sic/Epoxy shew superior results compared to the other materials.

In Ref. [30] it was researched on "Analysis on Wind Turbine Blade Using Composite Materials." The required blade cross-section can be achieved by proper blade design to get the maximum torque. In this research, four varieties of composites material studied their performance characteristics. The analysis of the wind turbine blade is implemented by utilizing the ANSYS Workbench based on Total

Deformation, Equivalent (Von-Mises) Stresses and Maximum Shear Stress. The results are shown the new polymer resins and reinforcement fibres of glass, carbon and aramid (Kevlar) have shown the efficient performance reinforced materials. additionally, the analysis of the results are demonstrated material Kevlar the best based on the deformation and Epoxy Carbon to equivalent (Von-Mises) and shear stresses furthermore, Carbon Fiber Reinforced Plastic according to Maximum Shear Stress(Pa).

In Ref. [31] it was conducted research on "A Light Material for Wind Turbine Blades." the research intends to explore a lightweight material that can be perfectly used in the fabrication of wind turbine blades and matched to its standard specifications. The studying was executed to rice straw fiber as a reinforcement factor in composite with polypropylene as a matrix. Then the composite manufacturing was tested for their mechanical behavior such as tensile, flexural and impact, also the density measurement, dynamic mechanical testing (DMA) and Scanning Electron Microscopy (SEM). The results gained from the testing mentioned above, the mechanical properties of the composite have improved by using rice straw fiber to the polypropylene matrix with less weight to be used to small scale horizontal wind turbine blades.

In Ref. [32] it was studied of "Materials for Wind Turbine Blades: An Overview." the blades are the main important parts among the wind turbines parts which are fabricated by composite materials, therefore, that blades are exposed to complicated, combined impact, static and random cyclic loading. On the one hand, to be a resistance of these loads during its life-time and hundreds of millions of loading cycles and on the other hand, decreasing the gravity load, the wind turbine blades are constructed from fiber-reinforced polymer composites. However, the existing obtainable solution is E glass/epoxy in the easiest case and fulfilling to most of these conditions. Carbon fibers appear to be the best promised alternate for the E glass fibers, and the other alternates are a high strength glass, basalt, aramid, and natural fibers. The carbon fibers have higher stiffness but on the other side, it has low compressive strength and high cost. Many researches are introduced helpful solutions by a combination of carbon and E-glass fibers to obtain high stiffness through carbon fibers with raise boundary of cost.

1.4.3 Aerodynamic Blade Design

In Ref. [33] it is scientific paper research on "Design Model of Horizontal Axis Wind Turbine Blade at Technological University (Thanlyin)." In this research, a horizontal axis wind turbine (HAWT) blade was designed to generate power of 1 KW, and the investigation of the airflow over blade has been implemented to obtain the blade aerodynamic behavior. The main ideal point of wind turbine power generation improvement is the blade design. The design of the wind turbine blade should be in its structure specifications enough strength, stiffness, elasticity, hardness, and stability. For that, the blade modeling and its strength. The most important step designing of the wind turbine blades is checked the blade modeling and strength. in this study shows to determine the design parameters calculations of the blade and its strength examine, the blade airfoil was chosen of NACA-4412, and applying in Comsol Multiphysics software and blade geometry in 3D was executed by SolidWorks software. The blade material was selected of Balsa wood and the blade strength checking was performed by numerical simulation and the results show the Von Mises Stress distribution over the blade is 6.6667 MPa and it is in the range of accepted stress compared to Balsa wood yield strength.

In Ref. [34] it is a scientific paper studied "Effects of Bend-Twist Coupling Deformation on the Aerodynamic Performance of Wind Turbine Blade." The bend-twist coupling deformation can be in benefit of improving the power generated, aerodynamic stability and on the other hand, decrease loads of the aerodynamic. The goal of this research is studied the phenomenon mentioned above into an existent blade design for investigation results of aerodynamic performance. The blade length is 41.25 m based on GE 1.5 GLX wind turbine. Blade Element Momentum (BEM) theory and Computational

Fluid Dynamics (CFD) simulation have applied to obtain the aerodynamic loads. The result value of torque and thrust are well agreed by using the two methods. Three different bend-twist couplings have applied for the blade composite skin of the Glass/Epoxy as follows: no coupling, low coupling, and high coupling. The deflection observations of the three types of the blades were a little the difference whilst the twist angles were extremely various. Then the deformed models were applied to make new 3D models for utilizing for its power coefficient prediction by CFD simulation. The results described that, at low wind speed, the power coefficient is greater than the baseline blade. Wind speed higher than the rated speed, the power coefficient is a reducing less than the baseline blade because the blades twisting occur too much.

In Ref. [35] it was researched on "Calculation of Optimum Angle of Attack to Determine Maximum Lift to Drag Ratio of NACA 632-215 Airfoil." The airfoil numerical simulation was proceeded to predict the optimum attack angle of the horizontal axis wind turbines applications. The simulation was implemented by the SST turbulence model for airflow over the NACA 632-215 airfoil. Aerodynamics parameters such as lift and drag coefficients, lift to drag ratio and power coefficient were computed and making a comparison with various wind speeds. The results are shown a raise on lift and drag coefficient at rising the wind speed and the lift to drag coefficient begins to grow for while then it drops again. The maximum value of the lift to drag ratio is obtained at four degrees. At the wind speed 10 m/s were computed the power coefficient and plotting a graph. According to the growing of the attack angle, the pressure difference between the upper and lower blade surface raises.

In Ref. [36] it is scientific investigation research on **"**Aero-Structural Optimization of a 5 MW Wind Turbine Rotor." The rotor blade of 5 MW founded on the NREL 5 MW wind turbine reference has improved the efficiency and reducing the hub flap-wise bending moment. The blade design is executed through eighty-three variables parameters including airfoil types according to Bézier curves, set at the root, mid-span, and tip sections; cord length and twist angle distributions; and bend-twist coupling value in the blade. An optimization is attained with a genetic algorithm. The new method is used relatively because it has less account compared with the finite element analysis for prediction of rotor bend-twist coupling behavior. Performance of airfoil is executed with XFOIL, the simulation of wind turbine has been done fast and the target is the energy cost (COE), set a rotor cost ($) AEP (MWh/yr), and annual energy production is namely (AEP). Techniques are utilized to reduce the cost of the rotor, in turn, supposed decreasing the flap-wise bending loads and blade surface area by decreasing the material. The simulation results are obtained the both of the flap-wise bending loads and blade surface area are minimized about 15% at no change of AEP and COE decreases by 6.8%.

In Ref. [37] it was researched on "Estimation of Wind Turbine Blade Aerodynamic Performances Computed Using Different Numerical Approaches." Models easier are demonstrated and performed whilst investigations of a different number of numerical methods for isolated horizontal axis wind turbine blade which is the content of three blades have implemented in ANSYS FLUENT 16.2 software. The field of flow is designed by using Reynolds Averaged Navier–Stokes (RANS) equations closed via two various models of turbulence. Simulation results involve universal parameters as thrust and the power coefficient, also the local distribution along the blade length estimated for the different models and comparing with the experimental data is available. The results comprise the fluid flow conception in the shape of velocity contours, pressure distribution in sections, and power generated value and thrust force coefficient for operation systems ambit. Though the estimating numerical results were different in accuracy, however, all of the current numerical settings appear to be less or higher referring to universal wind turbine parameters which are power and thrust force coefficients. The wind turbine aerodynamics are greatly influenced by turbulence, and it should consider at the design.

In Ref. [38] it was carried out research on "Aerodynamic, Structural and Aero-elasticity Modelling of Large Composite Wind Turbine Blades." the objective of this research is more improvement of models basis on aerodynamic, structural, and aero-elasticity analysis for large wind turbine blades fabricated by fiber-reinforced composite material. Developed blade element momentum (BEM) model has improved through the collection of combining the odd corrections with the classical BEM model. For comparison with other existing models, the current BEM model computes more accurate of the tip and root losses. In this case, the current BEM model of aerodynamic coefficients in static measurement 2D agrees with experimental measurements.
Model of TWCSCB improved is evolved in a new method can be applied for both single-cell and multicell closed sections fabricated of arbitrary composite laminates because it is found out a considerable lack in composite beam model (TWCSCB) analytical for the thin-walled which proposed by Librescu and Vo, and that has vastly utilized for structure modeling of wind turbine blades. the current TWCSCB is confirmed for a different of engineering models and arbitrary laminate layups, the numerical investigations are also implemented on actual wind turbine blade (NPS-100) for structural analyses. Between the current TWCSCB model and the ABAQUS finite element (FE) shell model discovered exact engagement.
In the end, integrated the developed BEM model and TWCSCB model use to evolve the static aero-elasticity model. The numerical simulation are performed on the NPS-100 wind turbine, while the interactions are calculated by the repeating operation. Results of numerical simulation describe important rectifications by modeling wind turbine blades with elastic coupling.

In Ref. [39] it was researched on **"**Design optimization of a wind turbine blade to reduce the fluctuating unsteady aerodynamic load in turbulent wind." This study was focused to decrease the fluctuation of the bending moment blade in turbulent wind. With a view to check the unsteady aerodynamic load of the wind turbine, a FAST code was utilized as the analysis code. The wind input model is considered turbulent wind in FAST code, a turbulent wind simulator applied by TurbSim. The chord length and twist angle represented the shape modeling function for dynamic engineering models representing of the aerodynamic shape of the wind turbine blade. The bending moment fluctuation at the root section of the blade was reduced while it preserves of required the power of wind turbines. In detail, through the reallocation of the segment force in the radial direction in between the primary and tip regions, the measure of the oscillated of the out-of-plane bending moment was minimized by around 20%, and the rated power of 1.5 MW was preserved.

In Ref. [40] it is an investigation research on "Optimal Performance of Horizontal Axis Wind Turbine for Low Wind Speed Regime." The most significant side of wind turbines design is developing the performance prediction. In this paper, an evolution methodology is utilized to prophesy the ideal performance of the horizontal axis wind turbine for the most important design parameters like tip speed ratio, pitch angle, number of blades and wind speed. A good plotting graph for the performance was performed. Results describe for low wind speed conditions, the pitch angle is recommended to be low. A tip speed ratio from 5 to 11 obtained as an ideal value according to constraints applied. Also, the influence of a cut in speed with enduring parameters is researched and its effect on the power and torque. Numerous results were introduced for wind turbines with three blades and it is a good chosen preferring from most producers and researchers.

In Ref. [41] it was carried out research on "Blade Design Optimization for Fixed-Pitch Fixed-Speed Wind Turbines." one of the advantages the Fixed-pitch fixed-speed (FPFS) wind turbines compared to other small wind turbines, especially for low wind speed sites. The blade design steps of Fixed-pitch fixed-speed (FPFS) wind turbines are completely various to fixed-pitch variable speed wind turbines blade design. The case studies of this research for a given baseline wind turbine and its blade airfoil. Aims of the research to show a functional optimization method for the blade design of FPFS small

wind turbines. The design optimization of the blade is concerned with the aerodynamic behavior of the airfoil, which is, the lift and drag coefficients, and the annual mean wind speed. The design parameters which influence the blade optimization such as the design of wind speed, design tip speed ratio, and design attack angle. Chain of design case studies utilizing several design parameters is researched for the wind turbine blade design. The comparison of the design results is performed to each other based on the power performance of the blade and annual energy generation. The results of the design for limited design cases show obviously which the blade design introduces the best performance.

In Ref. [42] it is a scientific paper research on "Optimized linearization of chord and twist angle profiles for fixed-pitch fixed-speed wind turbine blades." Objectives of this paper are to describe a new ideal blade design process for an FPFS wind turbine by reliant the linear radial profiles of the blade chord, twist angle and improving the slope of both of two lines. a radial shapes of the blade chord length and twist angle are plotted in linearity lines to help for discovering based on the constant values at the blade tip and flotation values at the blade root according to essential design, and the best result is selected through utilizing the elevated the value of AEP for the specific wind speed Weibull distribution as the optimization standard with constraints of the top limit power output of the wind turbine. The results show obviously the optimization method presents a perfect chance to introduce the best power performance and depressed industrialization cost. This method utilizing can apply for the FPFS wind turbine blade design and renew.

In Ref. [43] it is a scientific paper research on **"**Design Optimization and Aerodynamic Performance Analysis of a Small Wind Turbine Blade." the scientific paper aims to design the improvement of the small wind turbine blade of 5 kW for residential application. This paper considers investigation on the aerodynamic sector of a wind turbine blade and optimal conditions are counted to driving train and electrical generator. A conception of blade element momentum (BEM) theory is a basis and estimations of implementation for obtained the design parameters. The same calculations are performed by PROPID and the comparison and validation execute for performance features. In general, the power curve should be existing of a final performance parameter for a wind turbine, it has consisted of a cut-in speed, cut-out speed, and its identical power. Through the analyzed the aerodynamic properties, the power curve plots, and it shows the cut-in speed where the power starts to generate, then it continues to rise at the wind speed increasing. In fact, a generator produces only rated power as it is shown in figure (1.6). The design wind turbine capacity of 5 KW was set for wind speed design 9 m/s. according to an analysis of the improved blade, the 5 KW capacity was achieved at 8.1 m/s which is less than the design wind speed.

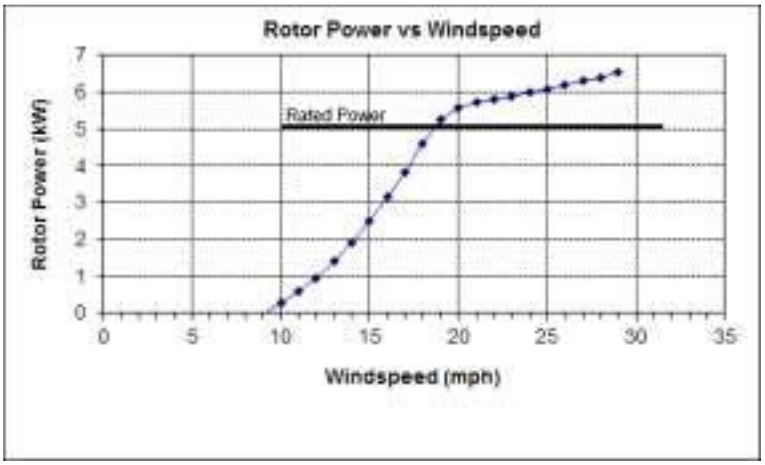

Figure (1.6) Power Curve

1.4.4 Structure Design (Optimization)

In Ref. [44], it is a scientific paper performed on **"**Composite Design Optimization and Weight Reduction for 10 KW (HAWT) Blades." Improvement of wind turbine blade structural performance was evaluated on various parameters which is one of them decreasing the blade weight and kept the same stiffness and strength of blade structure composite. The composite blade design improvement was tested on the whole of the blade parts. The figure of composite layers and their positions in all blade parts are deemed as design variables. The wind turbine blade is fabricated of carbon fiber laminate with epoxy resin. A collection of three carbon plies was utilized with fiber orientation at ± 45º, (Bidirectional fabric) and 0º, 90º (Unidirectional fabric). The best model configuration was selected with deflection 186 mm, and the deflection result is in the allowable range. The table (1.1) demonstrates the reduction of the blade weight of two different case studies of model configuration.

Table (1.1) Results of Weight Reduced

Component	Existing Model (Kg)	Proposed Model (Kg)	
		Model 1	Model 2
Top Pressure Shell	25.45	21.39	11.04
Bottom Pressure Shell	25.35	14.68	10.00
Shear Web	4.00	3.32	3.32
Shear Cap	15.00	14.00	10.76
Hub	15.00	15.00	15.00
Total	84.80	68.39	50.12

In Ref. [45] it was performed research on "Design and Material Optimization of 1.5MW Horizontal Axis Wind Turbine Blades with Natural Fiber Reinforced composites using the Finite Element Method." The research objective is decrease the wind turbine blades weight by using hybrid composites, 1.5 MW wind turbine blades which are mostly utilized in the area of Visakapattanam with a cut-out wind speed between 14 to 21 m/s. the blades designing are performed with a variety of natural fiber-reinforced composite materials and implemented the analysis of their static and dynamic performances then it is made comparison the results, also the blade weight. It has realized from results that the blades using natural fiber reinforced less weight than the blades using fiber glass with good performance competition. The blade modeling and analysis are executed utilizing UNIGRAFIC-NX (NX-CAD &NX-NASTRAN) software. The Dynamic Analysis Results of three different composite material shows in the figure (1.7) and figure (1.8) describe the Comparison of stress and the Blade Mass respectively.

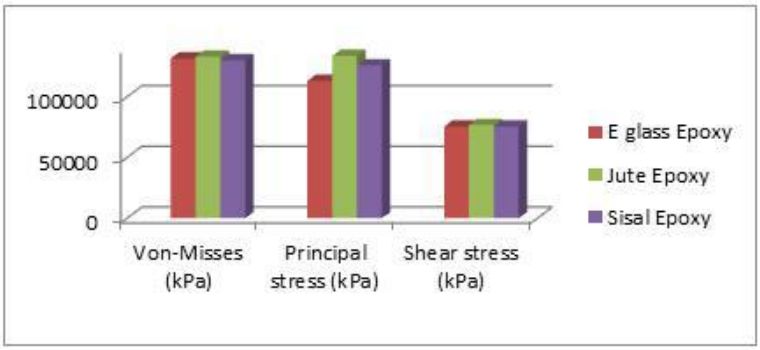

Figure (1.7) Dynamic analysis results

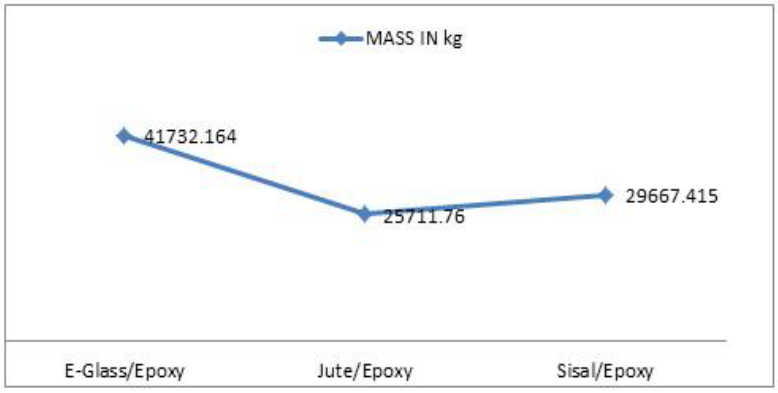

Figure (1.8) Comparison of the blade mass

In Ref. [46] it is a research study on "Research on Structural Lay-up Optimum Design of Composite Wind Turbine Blade." blade designing was executed for a variety of structure layups of 1.2 MW horizontal axis wind turbines based on theoretical computation result of stress, which can efficiently afford for different loads. the analysis of results show the lay-ups stress and strain, according to composite laminate theory and finite element method, the ideal layup sequence $[0°/\pm60°/90°]_S$ is emphasized. The analysis verification of stiffness and strength were implemented for maximum load conditions. The numerical computation results describe placement curve distribution is mostly linear. On the one hand, the highest deformation of blade tip accepted according to the required design stiffness, and on the other hand, the maximum stress criterion is selected, and the maximum first principal stress and shear stress of the blade root assert the required design strength.

In Ref. [47] it was carried out research on "effect of layup design on properties of wind turbine blades." the simulation software used is the ANSYS software to check composite structure blade layup and analyzed the model and its strength through the application of the composite laminate theory and finite element analysis method. Reduction of the interlayer shear stress between plies ±45° and 0° is applied dual laying of the ply ±45°, the symmetric model is selected. the composite material utilized is selected the glass fiber/epoxy of both sides with a density of 1950 kg/m3 and PVC shape board in the middle to retain resistance compression stability of the blades. two different conditions are applied for simulation operation: the first operating condition is applied fixed force in a flap-wise direction by 35 KN in distance 30 m from the blade root, and the second operating condition, four points forces are applied 59 KN, 37.2 KN, 24 KN, and 21 KN respectively from left to right, in distances from the root are 10 m, 4 m, 5 m, 8 m respectively. The results are obtained and compared with the experimental data for the blade mass and gravity center that show the blade design process of the lay-ups is applicable. The structural was analyzed and compared for various deformations on the flap wise and edge wise supplied the rules for blade lay-up optimization.

In Ref. [48] it was conducted research on "Fluid-structure Interaction and Multidisciplinary Design Analysis Optimization of Composite Wind Turbine Blade." the research was concerned with studying coupling structural and the aerodynamic performance by applying the MDAO process for the wind turbine blade, the studying is executed in three steps and the numerous design variables. the first step is to obtain the optimum attack angle of blade cross-sections along the blade span-wise direction, the second step is a selection of optimum composite material and their lay-up distribution by utilizing fluid-structure interaction system to obtain real loads pressure which influence on the blade. In the third step, both results of structural analysis, and CFD are utilized with the cost evaluation for the optimization method to find a proper result between the structural and aerodynamic performance.

Optimization method of aero-structure was implemented in 2D of aerodynamic analysis of SERI-8 blade utilizing Qblade, and for structural-aerodynamic analysis executes in 3D by utilizing ANSYS workbench. The results describe that the optimization method can use to obtain optimum in multidisciplinary objective optimization. The improvement of aerodynamic performance was raised by around 4% indicated to the baseline design. In addition, other results were obtained as follows: minimizing maximum deformation by 19.98%, maximum stress by 12.35%, blade mass by 23.67% and cost by 27.25%.

In Ref. [49] it is scientific paper research on "design of smart structures for wind turbine blades." Goals of this research to manage the reverse reaction structure of the blade profile with the different operational parameters like wind speed and material properties on the performance of blades. The wind turbine is designed for capacity 5 KW for the blade length 2.5 m and modeling in NACA 4412 airfoil for whole the blade. The blade fabrication is made by glass fiber reinforced plastic (GFRP) and the blade simulation is implemented according to plies sequence [0º /90º /-45º /+45º]. The finite element in Abaqus program is developed to estimate the blade deformation efficiently. Results of Abaqus are compared with the present experimental work, and it is a good agreed with the experimental data. It can be using finite element analysis in Abaqus for the deformation prediction of a wind turbine blades.

In Ref. [50] it was conducted research on "Structural Optimization Design of Horizontal-Axis Wind Turbine Blades Using a Particle Swarm Optimization Algorithm and Finite Element Method." this research introduces an optimizing process for the design structure of horizontal axis wind turbine blades on basis the particle swarm optimization algorithm (PSO) integrated with the finite element method (FEM). The main research objective is to found an optimizing tool and prospective improvement could be entered into the structure design of HAWT blades. The present blade is designed for capacity 1.5 MW by length 37 m and manufactured from composite material with a mass of 6,580.4 kg. The blade is considered as a cantilever beam with freedom degrees for fixed at the root section. The wind turbine blade classification is a class I with a reference wind speed of 50 m/s. the extreme flap-wise bending load is utilized for analysis of blade structure. More clarity, the load is decreased to specific concentrated loads are used to apply on the blade from the pressure side towards the suction side to be compatible with the experiment, the loads applied are shown in the figure (1.9).

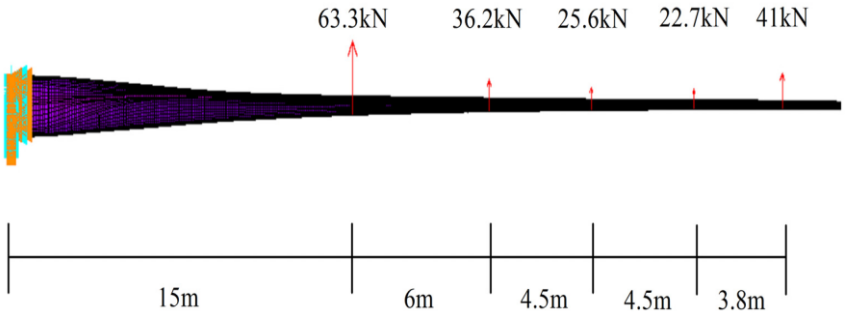

Figure (1.9) Loads distribution of the FEM model.

The process mention above is used effectively method for 1.5 MW HAWT blade. The results are shown a reduction in the blade mass is obtained and blade inclusive behavior is improved and achieved through reorganization of main composite material layups of both the spar cap and the positions of the shear webs according to the production and manufacturing opinion. Both results of simulation and

experimental are described in agree to each other for the deformation along the blade span-wise as in the figure (1.10).

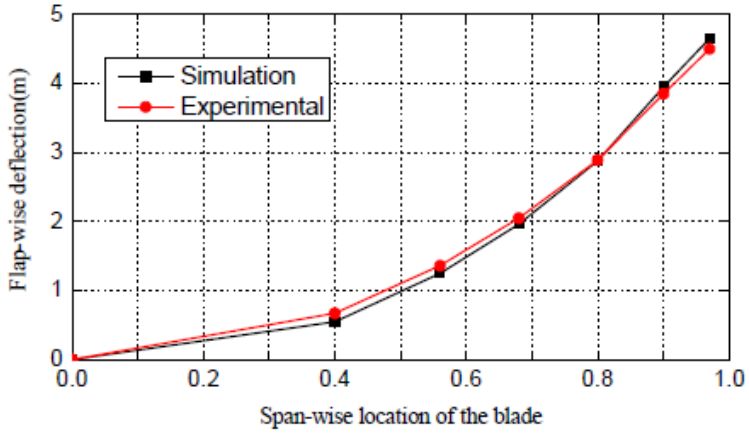

Figure (1.10) Flap-wise deflection along the span-wise of the blade.

In Ref. [51] it was performed research on "Structural Analysis and Design of the Composite Wind Turbine Blade." blades of the wind turbine support different types of loadings over the operation and also parking conditions. Wind turbine blades have increased in size to get more power produced, hence the arrangement of the composite materials in an efficient way is most important to be reached the optimum used of the material strength. The woven glass fiber reinforced epoxy is selected to be composite material in this study and it is deemed to be isotropic material and its ultimate strength 85 MPa. The blade is designed in the length 3.5 m and split into 11 sections. The composite blade is designed on a basis of failure criterion of the materials. The blade deformation raises from 140 mm to 160 mm of the initial and optimized designs respectively. The total mass of first designed is 30.375 kg. during the loading condition of the ultimate wind speed (59.5 m/s), the largest deflection in the blade tip is 140.2 mm and the highest principle stress 57.102 MPa, -3.7104 MPa for the leading side and the backside respectively. The blade deflection of the final design is around 160 mm with its weight 27.8 kg. The result is shown in the figure (1.11) are got by thickness

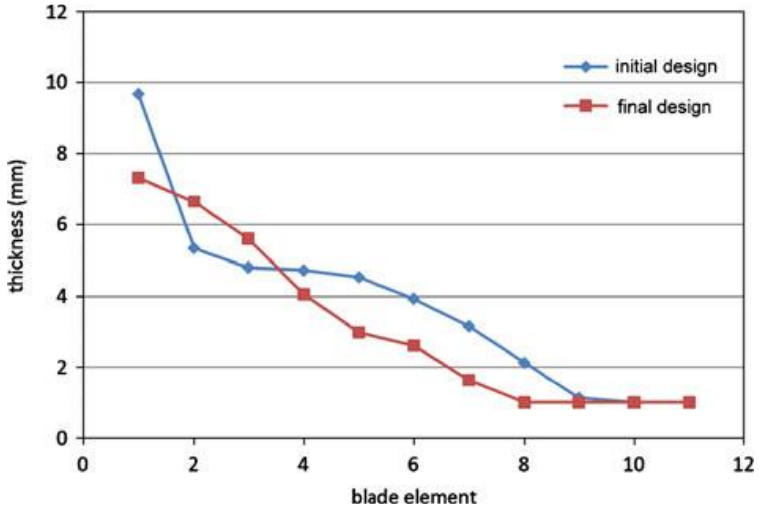

Figure (1.11) the thickness distributions of the composite blade skin for both the initial and final designs.

modification of composite blade skin. The most elements thickness are decreased while the elements 2 and 3 are growth to reinforce the strength at its areas. The ultimate principal stresses are described as in figure (1.12).

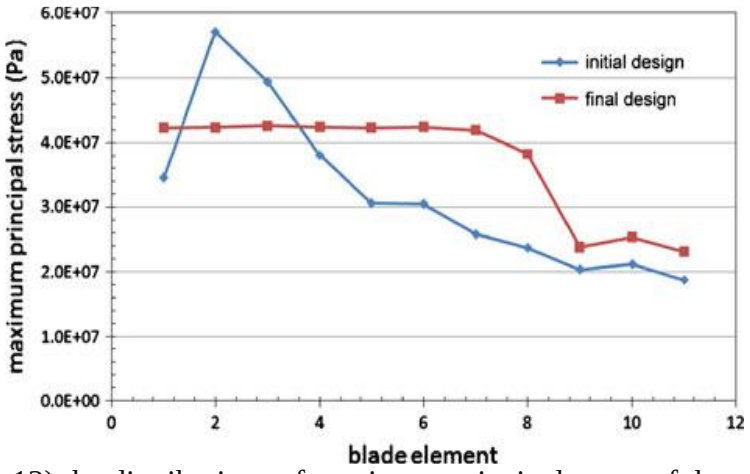

Figure (1.12) the distributions of maximum principal stress of the composite blade skin for both the initial and final designs

1.5 Aeroelasticity

Unsteady flows lead arise to a number of aero-elasticity problems that can influence wind turbine blades stabilization. Thus, aero-elastic problems are an important phenomenon to be knowing and took in consideration on the design stage. The aero-elasticity definition is the study of the interaction between mechanical and aerodynamic forces affecting a body [52].

The flexibility of blades is the main factor for rising the aero-elastic phenomenon in wind turbines. "Aero-elasticity is the study of the mutual interaction between the aerodynamic and elastic forces, and the influence of this interaction on blade design" [53].

Aeroelastic phenomena

Aero-elasticity points to the science of the interaction between the aerodynamic, inertial and elastic influences. Aero-elastic influences take place everywhere but are more or less critical. Any project that has a structure facing the aerodynamic forces needs to take consideration of the aero-elasticity.

In most cases, when a big structure that has flexibility is introduced to a high intensity variable flow, the deformations can easily exceed allowable levels. Most people are familiar with the "auto-destruction" of the Tacoma Bridge. The bridge was built in Washington State, USA, with 1.9 km long, and was the longest suspended bridges in that time. The bridge collapsed in a spectacular way on Thursday, November 7, 1940. While the wind speed was raised to reach 65-75 km/h, the oscillations of the bridge grew as the result of fluid-structure interaction and based on aero-elasticity, sudden the bridge collapsed. Recorded videos of the accident shew the motion of initial torsional of structure merged with very turbulent winds flow. Overlap both two influences, also insufficient structural dumping magnified the oscillations reaching failure level. Figure (1.13) illustrates the visual response of a bridge subject to aero-elastic effects due to variable wind regimes. The simulation was implemented using Multiphysics simulation on ANSYS-CFX software [54].

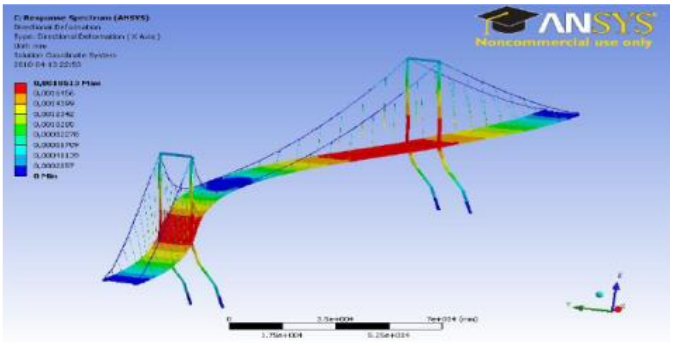

Figure (1.13) Aeroelastic response of a bridge [51]

The aero-elastic phenomena occur when the structure deformations induce part of additional aerodynamic forces which make produce some additional structure deformations in order to induce again more aerodynamic forces reaching in structure collapse. The dynamic aero-elasticity phenomena involve the interactions among all the inertial, aerodynamical and elastic forces, while the static aero-elastic phenomena involve the interactions between aerodynamical and elastic forces [54]. Figure (1.14) show the relationship between the all these forces.

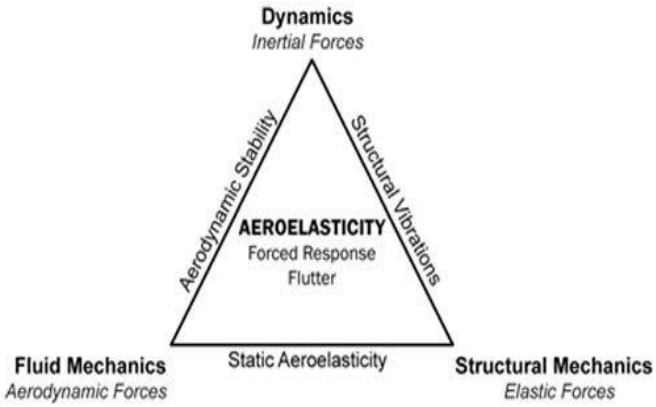

Figure (1.14) Aeroelasticity collar diagram. [56]

In an attempt to increase power production and reduce material consumption, wind turbines blades are becoming increasingly large yet, paradoxically, thinner and more flexible. The risk of occurrence of damaging aeroelastic effects increases significantly and justifies the efforts to better understand the phenomena and develop adequate design tools and mitigation techniques. Divergence and flutter on an airfoil will be used as introduction to aeroelastic phenomena. When a flexible structure is subject to a stationary flow, equilibrium is established between the aerodynamic and elastic forces (inertial effects are negligible due to static condition). However, when a certain critical speed is exceeded, this equilibrium is disrupted and destructive oscillations can occur [54].

In Ref. [57] it is a scientific paper research on CFD-FEA Coupled Simulation of the Dynamic Aeroelastic Response of a Large Scale Horizontal Axis Wind Turbine Rotor. In order to design reliable and effective blade wind turbines, the required perfect modeling of the blade aeroelastic response under the real of wind conditions to comprise the influence of the blade flexibility. This paper conducts the numerical simulation results of the flow field around a 3-bladed of horizontal axis wind turbine (HAWT) and the blade aeroelastic reaction utilizing a coupled computational fluid dynamic (CFD) and finite element analysis (FEA) approach. The blade has designed by airfoil type a NACA 64 profile with a spar-box strengthener. The wind shear entire the blade extent and influence of weak turbulence is

contained in the unsteady aerodynamic load computation. The velocity domain ahead and in the rotor weak is gained for various mean wind speeds at the entry. The time history of the flap-wise blade deformations is calculated at various positions of blade. The weak turbulence was inspected by calculating the turbulence intensity.

In Ref. [58] it was conducted research on Wind Turbine Aeroelastic Modeling: Basics and Cutting Edge Trends. The interaction system of fluid flow and dynamic of the structure is a necessary matter for the operation of mechanical equipment under their coupling. This paper shows the general view of aeroelastic applicance for wind turbines, the attempts achieved, disability, and future orientation set. one begins with the background of the matter, presentation of a case study to show the influence of fluid-structure interaction taking into account NREL blade 5 MW, and a short comparison of various of aero-elastic codes. Dealing with the efforts made in the region like as complicated inflow, the influence of geometrical nonlinear, and else stabilization issues and smart control are managed and derived by putting the disabilities and future orientation of aeroelasticity of wind turbines.

In Ref. [38] it was carried out research on Aerodynamic, Structural and Aero-elasticity Modelling of Large Composite Wind Turbine Blades. This research is focused on development aerodynamic, structural and aeroelasticity models for large wind turbine blades made of fiber reinforced laminated composite materials. While in aeroelasticity studying part that, the model of aeroelasticity is improved by integrating the improvement BEM model and TWCSCB model. The interactions are calculated through a repeated process. The numerical implementations are achieved on NPS-100 wind turbines. The numerical results describe some important rectifications by modeling wind turbine blades with elastic coupling.

In Ref. [59] it was carried out research on an Aeroelastic Behavior of a Wind Turbine Blade by a Fluid-Structure Interaction Analysis. A fluid simulation interaction (FSI) for the numerical model is improved to examine of the aero-elastic reaction of a single blade of the wind turbine. The Blade Element Momentum (BEM) theory was selected to compute the aerodynamic forces taking into account the influence of wind shear, as well as the tower shadow. The wind turbine blade was designed as a rotative cantilever beam separated utilizing the Finite Element Method (FEM) to resolve the deformation and vibration of the blade. The aeroelastic reaction of the blade was gained by coupling these aerodynamic and structural models utilizing a coupled BEM-FEM coded written in MATLAB. The dominating (FSI) equations of motion are repeatedly computed at each time step, over alternating data between structure and fluid by utilizing a Newmark's implicit time integration planner. The results gained in this paper describe that; the suggested modeling can be utilized for a fast estimation of the wind turbine blades considering the fluid-structure interaction, as well as it can be a valuable tool for the analyses of airplane propeller blades. The flap-wise deformation and stabilization after a time of interactions. The results of aerodynamic loads are so influenced by the blade elasticity which will affect power generating.

In Ref. [60] it was researched on Two-way Fluid-Structure Interaction Simulation of a Micro Horizontal Axis Wind Turbine. This paper describes that, a two-way of Fluid-Structure Interaction (FSI) analyses executed on a small scale horizontal axis wind turbine (HAWT) which made through the coupling of the CFX solver with Structural solver in ANSYS Workbench was proceeded. The study execution was by the partitioned approach-based non-conforming mesh methods and the k-ε turbulence model. The results of both the one-way and two-way FSI analysis were approached and made comparison with each other, and analyzed of variance of the results essently the mechanical properties. The most important to the results is grid convergence, which was executed, and the relation between the interior flow domain (rotational domain) and the number of grids (number of cells, elements) was confirmed for the first time. Dynamic analysis of wind turbine was performed utilizing the results of

torque value as reference, to prove reasonable model which control of the accuracy of results. The ideal case was confirmed and utilized to do the study, so the simulation results of the FSI are a precise and feasible.

In Ref. [61] it was conducted research on the growing size and elasticity large wind turbine blades cause major aeroelastic influences, which are happened by the fluid-structure interaction (FSI). These influences might be harmful to the blades because of aeroelastic instability problems, like as edgewise instability, and flutter, which may be destroyed the wind turbine blades. For that, precise FSI modelling of wind turbine blades is more important in the improvement of large wind turbines. In this study, an FSI model for wind turbine blades at the real scale is set. The aerodynamic loads are computed by utilizing a CFD (computational fluid dynamics) model performed in ANSYS FLUENT, and the blade structural responses are set utilizing a FEA (finite element analysis) model performed in ANSYS Static Structural module. The interface of CFD and FEA is relied on a one-way coupling, in which aerodynamic loads computed from CFD modelling are determined to FEA modelling as load boundary conditions. The one-way FSI model was applying to model of WindPACT 1.5 MW wind turbine blade. Five operational conditions are valued, found the worst-case near the rated wind speed. The results of high tensile/compressive stresses and tip deflections at all cases are located to be within the material and structural limits, as well as according to pertinent design standards.

In Ref. [62] it is scientific investigation research on The Evaluation of Aerodynamic Interaction of Wind Blade Using Fluid-Structure Interaction Method. This paper shows the estimation procedure of the aerodynamic load on the blade of wind turbines by utilizing the Fluid-Structure Interaction (FSI) process. Aerodynamic loads are set by 3D Computational Fluid Dynamics (CFD), and then it is enforced application to blade structure through using an interface which connects the FSI interaction. The interface partakes participate at the surface topology. The steady and transient CFD analyses are implemented using k-ω SST turbulence model for both of 1-way and 2-way interaction. The investigation of CFD results is implemented through the comparison of data experimental, which were done by NREL. The calculation and verification of aerodynamic loads are enforced to the modeling of the blade structure. The studied and investigated aerodynamic loads are applied to the blade structure. The efficient of structure stiffness was found from the analysis of frequency which rely on the eigenvalue. According to the study the sensitiveness mesh parameters. The wind power coefficient and torque value are obtained and highly influenced by the fluid mesh characteristics. The structural mesh characteristic was more important for aerodynamic load mapping in CFD to the structure.

Ref. [63] it was carried out research on Performance Prediction of a 5MW Wind Turbine Blade Considering Aeroelastic Effect. This study conducted for analysis of aeroelasticity response and performance of a 5 MW of the wind turbine blades which is made of composite material. Advanced process of coupled numerical rely on Computational Fluid dynamics (CFD) and Computational Flexible Multi-Body Dynamics (CFMBD) has been improved for the investigation of aeroelastic responses and performance characteristics of the composite rotor blade. Reynolds-Averaged Navier-Stokes (RANS) equations using (k-ω) with SST turbulence model were computed for unsteady flow cases on the rotary wind turbine blade model. As well, structure analyses taking into account rotary affect have been done utilizing the general nonlinear finite element process. A completely implied time progress planner rely on the Newmark through integration process is done to compute the coupling of aeroelastic dominate equations of the 3D wind turbine blade for Fluid-Structure Interaction (FSI) cases. The aeroelastic response is calculated in the time domain for the accomplishment of the investigation of aeroelastic characteristics of the 3D wind-turbine blade model. It is greatly described that the rated power of the blades may be considerably vary caused by the influence of aero-elastic deformation.

CHAPTER TWO

THEORETICAL BACK GROUND OF COMPOSITE WIND TURBINE BLADE DESIGN

2.1 Blade Element Momentum Theory

Blade element momentum (BEM) theory is the method which is most commonly used for computing induced velocities on wind turbine blades [64].The steady state aerodynamics of wind turbines analysis is used the momentum and blade element theory. A wind turbine blade structure contains airfoils that create a lift force based on the pressure difference across airfoil, leading the same change of pressure seen in the actuator disc type of analysis. An actuator disc has represented the flow field around a wind turbine rotor and was set utilizing the conservation of linear and angular momentum. Characteristic of the flow field around the wind turbine rotor can describe by axial and angular induction factors which are a function of the rotor power extraction and thrust and used for determination of air flow at the rotor airfoils. The blade geometry and the lift and drag coefficients of the airfoils can be utilized to set the rotor shape if specific performance parameters are known, or rotor performance if the blade shape has been known. Where lift force (F_L) is a perpendicular to the wind flow direction and the drag force (F_D) is a parallel to the wind flow direction [65], as is described in the figure (2.1)

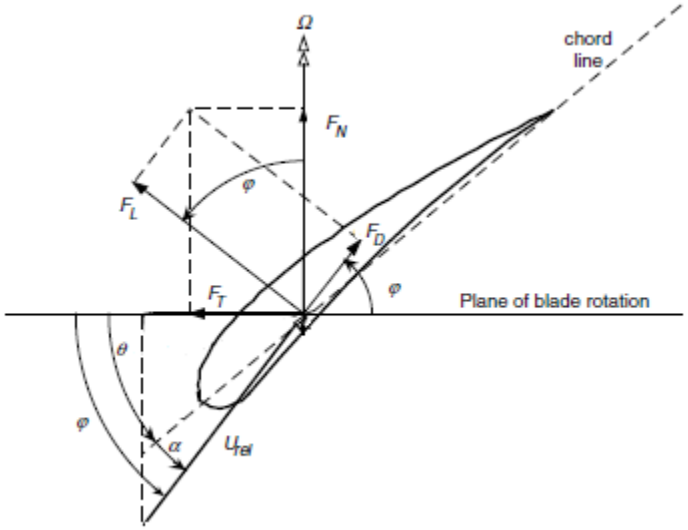

Figure (2.1) Forces acting on the blade from interaction with wind air flow [2]

Lift and drag properties of airfoils are generally obtained by load measurements on airfoils in wind tunnels [66]. , and presented by lift coefficient (C_L) and drag coefficient (C_D) as a function of the angle of attack (α). The angle of attack can be defining as the angle between the airfoil chord (C), and the relative direction of the wind speed (U_{rel}), where the chord is the length of a straight line between the leading and trailing edge of the cross section.

The analysis implement by the application of momentum theory and blade element theory. Momentum theory indicates a control volume analysis of the forces at the blade according to the conservation of linear and angular momentum. While Blade element theory indicates an analysis of forces at a section of the blade, as a function of blade geometry. The process results can merge into the blade element momentum (BEM) theory. This theory has been utilized to connect blade shape to capable the rotor for power extraction from the wind [2]. In BEM the swept area of the turbine is

discretized into number (N) of annular elements of width (dr), as can be shown in the figure (2.2). The lateral boundary of these elements.

There are two assumptions applied in the BEM method for those annular elements:

1. Annular elements are known by streamlines, thus air does not flow between each one of them, i.e. the elements are radially independent.

2. The flow is a constant in each annular element, which is the same assumption an infinite number of blades

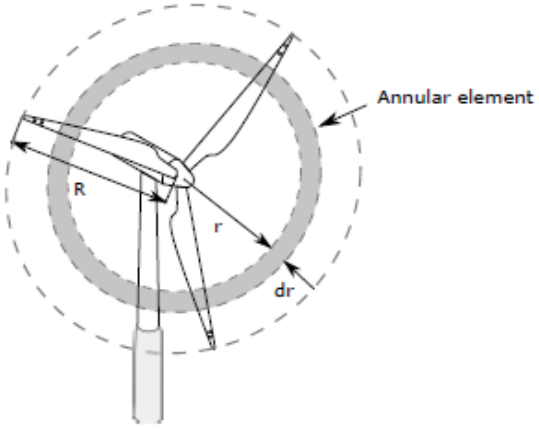

Figure (2.2) annular elements used for BEM method.

It can be seen from the figure (2.3) that the inflow angle (ϕ), the angle of attack (AOA) (α) and the velocities used for the calculations which are the tangential velocity $\omega r(1+a')$ and axial velocity $U_0(1-a)$ at the rotor plane, where ω is the rotor rotational speed, a is the axial induction factor, a' is the tangential induction factor and U_0 is the steady state wind speed ahead of the turbine. Moreover, U_{rel} is the wind relative velocity to the rotating turbine blade and defined as [67]:

$$U_{rel} = \frac{U_0(1-a)}{sin\phi} = \frac{\omega r(1+a')}{cos\phi} \quad (2.1)$$

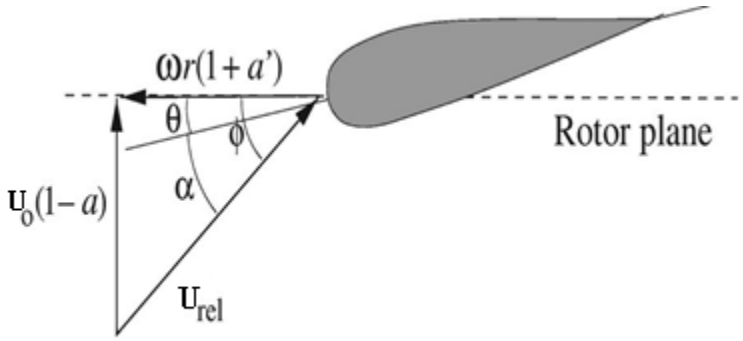

Figure (2.3) Velocities at the rotor plane

From the figure (2.3) it can be realized that the flow angle ϕ is equal:

$$\phi = tan^{-1}(\frac{V_0(1-a)}{\omega r(1+a')}) \quad (2.2)$$

And the attack angle α is the difference between the flow angle and the local pitch angle θ:

$$\alpha = \phi - \theta \quad (2.3)$$

The forces effecting on the blade can be seen in figure (2.1) and are indicated as F_N in the axial or the normal direction of the blade and F_T in the tangential direction of the blade. Both forces are the dropping of the lift and drag forces and can be defined as:

$$F_N = C_N \frac{1}{2} \rho C U_{rel}^2 \quad (2.4)$$

$$F_T = C_T \frac{1}{2} \rho C U_{rel}^2 \quad (2.5)$$

Where C_N and C_T can be found by dropping the lift and drag coefficients in the normal and tangential direction as:

$$C_N = C_L cos\phi + C_D sin\phi \quad (2.6)$$

And:

$$C_T = C_L sin\phi - C_D cos\phi \quad (2.7)$$

As it is mentioned before, the lift and drag coefficients are functionally relationship of the attack angle, and can be found from force measurements on airfoils in wind tunnels. Furthermore, a solidity is known as the fraction of the annular area in the control volume which is wrapped by wind blades.

$$\sigma(r) = \frac{c(r)B}{2\pi r} \quad (2.8)$$

Where, *B* is the number of blades, *c*(*r*) is the local chord length and *r* is the radial Position of the control volume.
The axial and tangential factors for BEM method are:

$$a = \frac{1}{\frac{4Fsin^2\phi}{\sigma C_N}+1} \quad (2.9)$$

$$a' = \frac{1}{\frac{4Fsin\phi cos\phi}{\sigma C_T}-1} \quad (2.10)$$

Where F is the correction factor.

As a result of the pressure on the suction part is lower than on the pressure part, the air trends to flows around the tip of the blade from lower to the upper surface, decreasing the lift force and therefore influence power generation near the tip. Numerous methods have been suggested to take into consideration the influence of the blade tip loss. The modest method for the usage which is improved by Prandtl (see de Vries, 1979). The correction factor (F) is a function of blades number, relative wind angle, and the blade position [68].

$$F = \frac{2}{\pi} cos^{-1}(\exp\left(-\left(\frac{B(1-r/R)}{2(r/R)sin\varphi}\right)\right)) \quad (2.11)$$

2.2 Numerical Modeling

A mathematical models and algorithms are required to perform numerical analysis for fluid -structure interaction. Computational fluid dynamics (CFD) is a section of the fluid mechanics which is used for numerical modelling and simulation of fluid flows. Finite element analysis is used for analysis of the structural behavior under various boundary conditions.

2.2.1Computational Fluid Dynamics (CFD)

1. Continuity and Momentum Equations

The evolution of a fluid element is governed by two conservation laws: the conservation of mass and the conservation of momentum. Mass conservation leads to the continuity equation and can be written as follows [69]:

$$\frac{\partial \rho}{\partial t} + \nabla \cdot (\rho \vec{u}) = 0 \tag{2.12}$$

The equation above is the general form of mass conservation equation and is valid for incompressible as well as compressible flows.

Conservation of momentum in an inertial (non-accelerating) reference frame can be described [70]:

$$\frac{\partial}{\partial t}(\rho \vec{u}) + \nabla \cdot (\rho \vec{u}\vec{u}) = -\nabla p + \nabla \cdot (\bar{\bar{\tau}}) + \rho \vec{g} + \vec{F} \tag{2.13}$$

Where p is the static pressure, $\bar{\bar{\tau}}$ is the stress tensor (described below), and $\rho \vec{g}\ and\ \vec{F}$ are the gravitational body force and external body forces respectively. $\vec{F}$ also contains other model-dependent source terms such as porous-media and user-defined sources.

The stress tensor $\bar{\bar{\tau}}$ is given by:

$$\bar{\bar{\tau}} = \mu[(\nabla \vec{u} + \nabla \vec{u}^T) - \frac{2}{3}\nabla \cdot \vec{u} I] \tag{2.14}$$

Where μ is the molecular viscosity, I is the unit tensor, and second term on the right hand side is the effect of volume dilation.

2. Reynolds Averaged Navier Stokes (RANS) Equations

The Reynolds-averaged Navier-Stokes (RANS) equations are related to the fluid flow motion of the time-averaged. These equations are utilized firstly during the application of the turbulent flow. These equations with approximation are utilized to obtain approximate average solutions to the Navier-Stokes equations depending on the knowledge of turbulence flow properties. The equations can be written in Cartesian tensor form as [71]:

$$\frac{\partial \rho}{\partial t} + \frac{\partial}{\partial x_i}(\rho u_i) = 0 \tag{2.15}$$

$$\frac{\partial}{\partial t}(\rho u_i) + \frac{\partial}{\partial x_j}(\rho u_i u_j) = -\frac{\partial p}{\partial x_i} + \frac{\partial}{\partial x_j}\left[\mu(\frac{\partial u_i}{\partial x_j} + \frac{\partial u_j}{\partial x_i} - \frac{2}{3}\delta_{ij}\frac{\partial u_I}{\partial x_I}\right] + \frac{\partial}{\partial x_j}(-\rho\overline{u_i' u_j'}) \tag{2.16}$$

These two equations (2.15) and (2.16) are called Reynolds-averaged Navier-Stokes (RANS) equations. In the instantaneous of solution variables in both Reynolds averaging and Navier-Stokes

equations are analysed into ensemble-averaged/time averaged and fluctuating components such as the velocity components:

$$u_i = \overline{u_i} + u_i' \tag{2.17}$$

Where $\overline{u_i}$ and u_i' are the mean and fluctuating velocity components (i=1,2,3).

Also the same, for pressure and other scalar quantities:

$$\varphi = \bar{\varphi} + \varphi' \tag{2.18}$$

Where φ symbolizes a scalar such as pressure, energy, or species concentration.

3. RANS Turbulence Models

For RANS turbulence models, (Scale-Adaptive simulation, detached eddy simulation, and shielded detached eddy simulation), the velocity scales V_m and V_k are determined as [72]:

$$V_m = \sqrt{k} \tag{2.19}$$

$$V_k = \left(\frac{\varepsilon\mu}{\rho}\right)^{0.25} \tag{2.20}$$

Where k is the turbulence kinetic energy, ε is the dissipation rate, μ is the molecular viscosity, and ρ is the density.

The time scales τ_m and τ_k are determined as follows:

$$\tau_m = \frac{k}{\varepsilon} \tag{2.21}$$

$$\tau_k = \sqrt{\frac{\mu}{\rho\varepsilon}} \tag{2.22}$$

In turbulence models based on the ω equation, the dissipation rate is computed utilizing the relation

$$\varepsilon = \beta^*\omega k \tag{2.23}$$

Where β^* is a model coefficient.

Using Reynolds stress models, the turbulence kinetic energy is determined as the trace of the Reynolds stress tensor:

$$k = \frac{1}{2}\overline{u_i'u_i'} \tag{2.24}$$

4. Boussinesq Approach

The Reynolds-averaged approach to turbulence modeling needs that, the Reynolds stresses in Equation (2.16) are suitably modeled. General method utilizes the boussinesq hypothesis to link the Reynolds stresses to mean gradients of velocity [71]:

$$-\rho\overline{u_i'u_j'} = u_t\left(\frac{\partial u_i}{\partial x_j} + \frac{\partial u_j}{\partial x_i}\right) - \frac{2}{3}(\rho k + u_t\frac{\partial u_k}{\partial x_k})\delta_{ij} \tag{2.25}$$

The Boussinesq hypothesis is utilized in many models such as the $k-\omega$ models.

The feature of this approach is the comparatively low computational cost related to the computation of the turbulent viscosity, u_t. In the case of the $k-\varepsilon$ and $k-\omega$ models, two more transport equations (for the turbulence kinetic energy, k, and either the turbulence dissipation rate, ε, or the specific dissipation rate, omega) are dissolved, and u_t is computed as a function of k and ε or k and ω.

5. Turbulence Models

The velocity fluctuation inducts the flow to be turbulent, these fluctuations generate a mixture of the transported quantities as momentum, energy, and species concentration, and also fluctuate the transported quantities. Since these fluctuations can be in the small scale form and high frequency, the simulation of this form is more computationally expensive. The instantaneous equations of continuity and momentum are accounted to be a time average, ensemble-averaged. These equations have additional contained flow unknown variables and turbulence models are applied to define these variables in turns known quantities [73]. The turbulent flow is defined by the Reynolds number.

The laminar flow can be considered when the Re number less than 1200, likewise the flow can be turbulent when the Re number is higher than that. The turbulent flow is described the fluid motion in a winding path. In this study, the design stream velocity is 8 m/s and based on the design velocity can be calculated Reynolds number which is ....., according to Reynolds number calculated, the flow is completely turbulent. Hence, the study assumption for the flow is to be incompressible flow.

There is different turbulence models in ANSYS fluent (CFD) can be chosen, such as:

- Spalart-Allmaras model
- *k-ε* models (standard, renormalization-group(RNG), realizable)
- *k-ω* models (standard, sheer-stress transport (SST))
- Transition SST models
- Reynolds Stress models (RSM)
- Detached eddy simulation (DES) model
- Large eddy simulation (LES) model

In this study, the turbulence model was chosen the shear stress transport *k-ω* model. The applications of a low of Reynolds number can use the k-ω SST model without extra damping functions. In the free stream, the SST formulation converts to a k-ϵ behavior to avoid that the k-ω problem that the model is very sensitive to the inlet stream turbulence properties. The turbulence model k-ω SST computes for its good behavior in adverse pressure gradients and flow separation [64].

6. Standard k-*ω* Models

As the k-ω model has been modified over the years, production terms have been added to both the k and ω equations, which have improved the accuracy of the model for predicting free shear flows.

The standard k-ω model uses transport equations of the turbulence kinetic energy and, the turbulence kinetic energy k, and the specific dissipation rate ω, which are developed by Wilcox (1988). These transport equations are [74]:

$$\frac{\partial}{\partial t}(\rho k) + \frac{\partial}{\partial x_i}(\rho k u_i) = \frac{\partial}{\partial x_j}\left(\Gamma_k \frac{\partial k}{\partial x_j}\right) + G_k - Y_k + S_k \qquad (2.26)$$

And

$$\frac{\partial}{\partial t}(\rho\omega) + \frac{\partial}{\partial x_i}(\rho\omega u_i) = \frac{\partial}{\partial x_j}\left(\Gamma_\omega \frac{\partial \omega}{\partial x_j}\right) + G_\omega - Y_\omega + S_\omega \quad (2.27)$$

In these equations, G_k represents the generation of turbulence kinetic energy due to mean velocity gradients. $G_{\boldsymbol{\omega}}$ represents the generation of ω. Γ_k and $\Gamma_{\boldsymbol{\omega}}$ represent the effective diffusivity of k and ω, respectively. Y_k and $Y_{\boldsymbol{\omega}}$ represent the dissipation of k and ω due to turbulence. All of the above terms are calculated as described below.

$$\Gamma_k = \mu + \frac{\mu_t}{\sigma_k} \quad (2.28)$$

$$\Gamma_{\boldsymbol{\omega}} = \mu + \frac{\mu_t}{\sigma_{\boldsymbol{\omega}}} \quad (2.29)$$

Where σ_k and $\sigma_{\boldsymbol{\omega}}$ are the turbulent prandtl numbers for k and ω, respectively. The turbulent viscosity μ_t is computed by combining k and ω as follows:

$$\mu_t = a^* \frac{\rho k}{\boldsymbol{\omega}} \quad (2.30)$$

$$a^* = a^*_\infty \left(\frac{a^*_0 + Re_t/R_k}{1 + Re_t/R_k}\right) \quad (2.31)$$

$$Re_t = \frac{\rho k}{\mu \omega} \quad (2.32)$$

$$R_k = 6 \quad (2.33)$$

$$a^*_0 = \frac{\beta_i}{3} \quad (2.34)$$

$$\beta_i = 0.072 \quad (2.35)$$

Note that for high Reynolds number form of the k-$\boldsymbol{\omega}$ model, $a^* = a^*_\infty = 1$.

The k-ω model is not needed to use damping functions near to a wall region.. As a result of the standard k-ω model has demonstrated to become more accuracy than the other models in the sub-layer of the boundaries. Moreover, its plainness yields a more strong numerical stability [12]. The standard k-ω model in ANSYS Fluent has sensitivity of the solutions to values of k and ω outside the shear layers. It has succumbed for several modifications to recompense for effectiveness of low-Reynolds number, compressibility, and shear flow spreading.

7. Shear-Stress Transport (SST) k-$\boldsymbol{\omega}$ Model

The k-ω Shear-Stress Transport (SST) model combines the standard k-ω and k-ε models and borrows the shear stress term from the Johnson-King model [75]. By this model the k-ω SST model implements a very well in the viscous sublayer and far wall regions. This is achievement by adding a blending functions are zero away from the surface in a k-ε model, and one in the near wall region in a k-ω model [76]. The transport equations for the k-ω SST model are:

$$\frac{\partial}{\partial t}(\rho k) + \frac{\partial}{\partial x_i}(\rho k u_i) = \frac{\partial}{\partial x_j}\left(\Gamma_k \frac{\partial k}{\partial x_j}\right) + G_k - Y_k + S_k \quad (2.36)$$

$$\frac{\partial}{\partial t}(\rho\omega) + \frac{\partial}{\partial x_i}(\rho\omega u_i) = \frac{\partial}{\partial x_j}\left(\Gamma_\omega \frac{\partial \omega}{\partial x_j}\right) + G_\omega - Y_\omega + D_\omega + S_\omega \quad (2.37)$$

In these equations, G_k represents the generation of turbulence kinetic energy, and is defined in the same manner as in the standard k-ω model. $G_{\boldsymbol{\omega}}$ represents the generation of ω. Γ_k and $\Gamma_{\boldsymbol{\omega}}$ represent the effective diffusivity of k and $\boldsymbol{\omega}$, respectively. Y_k and $Y_{\boldsymbol{\omega}}$ represent the dissipation of k and ω due to turbulence. D_ω represents the cross-diffusion term. S_k and S_ω are user defined source terms.

The effective diffusivities for k-ω model are given by

$$\Gamma_k = \mu + \frac{\mu_t}{\sigma_k} \tag{2.38}$$

$$\Gamma_{\boldsymbol{\omega}} = \mu + \frac{\mu_t}{\sigma_{\boldsymbol{\omega}}} \tag{2.39}$$

As explained by the successful model of the Johnson-King, consideration of turbulent shear stress could highly effect on accuracy in aerodynamic applications. The turbulent viscosity formulation was amended to implicate turbulent shear stress in limited wall flows, which was achieved by a blending function [75]. The turbulent viscosity is represented by:

$$\mu_t = \frac{\rho k}{\omega} \frac{1}{\max[\frac{1}{a^* a_1 \omega} SF_2]} \tag{2.40}$$

Where S is the strain rate magnitude and a^* is defined in equation (2.20).

$$\sigma_k = \frac{1}{F_1/\sigma_{k,1} + (1-F_1)/\sigma_{k,2}} \tag{2.41}$$

$$\sigma_\omega = \frac{1}{F_1/\sigma_{\omega,1} + (1-F_1)/\sigma_{\omega,2}} \tag{2.42}$$

The blending function $F_1$is given by:

$$F_1 = \tanh(\emptyset_1^4) \tag{2.43}$$

$$\emptyset_1 = \min[\max\left(\frac{\sqrt{k}}{0.09\omega y}\frac{500\mu}{\rho y^2 \omega}\right)\frac{4\rho k}{\sigma_{w,2} D_\omega^+ y^2}] \tag{2.44}$$

$$D_\omega^+ = \max[2\rho \frac{1}{\sigma_{\omega,2}} \frac{1}{\omega} \frac{\partial k}{\partial x_j} \frac{\partial \omega}{\partial x_j} 10^{-10}] \tag{2.45}$$

F_2 is given by :

$$F_2 = \tanh(\emptyset_2^2) \tag{2.46}$$

$$\emptyset_2 = \max[2\frac{\sqrt{k}}{0.09\omega y}\frac{500\mu}{\rho y^2 \omega}] \tag{2.47}$$

Where y is the distance to the next surface and D_ω^+ is the positive portion of the cross-diffusion term D_ω. F_1 and F_2 are the blending function.

2.3 Micromechanics Analysis of Unidirectional Lamina

Micro-mechanics concerns the studying of composite materials to consider the interaction of the constituent materials in detail. Micro-mechanics can permit the engineers to represent a

heterogeneous material as an equivalent homogeneous material, usually anisotropic. Micromechanics is used for the prediction of composite material stiffness and strength. Composite materials are fabricated by combinations of different fibers with different matrices. The relative amount of constituent for fiber and matrices can be controlled by engineers, and the geometry of the part, simultaneously [77].

2.3.1 Ultimate strengths of a unidirectional lamina

In this section, strength parameters can be calculated based on the respective properties of fibers and matrix using the mechanics of material method. The unidirectional lamina strength parameter predicts more difficult than the stiffnesses parameter because of the strengths have a sensitivity to the material and geometry inhomogeneous, the fiber-matrix interface, the manufacturing process, and the environment. Finally, the intensity of the experimental evaluation is very significant because it is direct and reliable [78].

1 Longitudinal Tensile Strength

Figure (2.4) presents of the simple model mechanics for materials approach.
Assume that;
. Both fiber and matrix are isotropic, homogeneous, it has linearly elastic behavior till the failure
. Matrix failure strain is higher than the fiber.

$(\sigma_f)_{ult}$ ultimate tensile strength of fiber

E_f Young's modulus of fiber

$(\sigma_m)_{ult}$ ultimate tensile strength of matrix

E_m Young's modulus of matrix

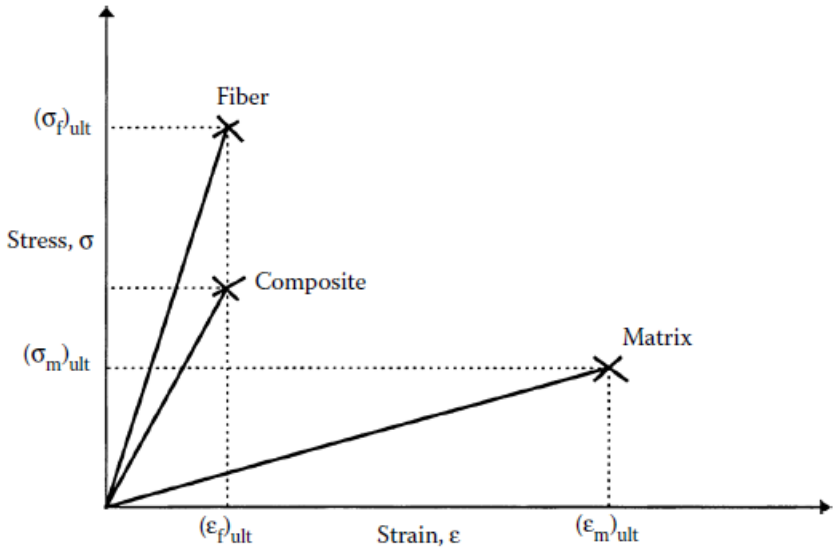

Figure (2.4) Stress–strain curve for a unidirectional composite under uniaxial tensile load along fibers.

Then the fiber ultimate strain failure is;

$$(\varepsilon_f)_{ult} = \frac{(\sigma_f)_{ult}}{E_f} \qquad (2.48)$$

And the matrix ultimate strain failure is,

$$(\varepsilon_m)_{ult} = \frac{(\sigma_m)_{ult}}{E_m} \quad (2.49)$$

For the reason of the fiber take most of the load in polymer matrix composites, can be assumed, if the fibers fail at the strain of $(\varepsilon_f)_{ult}$, the complete composite will fail. So, the composite tensile strength is presented by;

$$(\sigma_1^T)_{ult} = (\sigma_f)_{ult} V_f + (\varepsilon_f)_{ult} E_m (1 - V_f) \quad (2.50)$$

The moment that, the fibers have broken, does the composite able to take more load? The stress that the matrix can take alone is given by the term $(\sigma_m)_{ult}(1 - V_f)$. In the only case, if this stress is larger than $(\sigma_1^T)_{ult}$ in the equation (2.50), can it potential for the composite to carry more load. The fibers volume fraction at the possibility for happening this case is called the minimum fiber volume fraction $(V_f)_{\text{min}imum}$;

$$(V_f)_{\text{min}imum} = \frac{(\sigma_m)_{ult} - E_m(\varepsilon_f)_{ult}}{(\sigma_f)_{ult} - E_m(\varepsilon_f)_{ult} + (\sigma_m)_{ult}} \quad (2.51)$$

2 Longitudinal Compressive Strength

Longitudinal compressive strength cannot use the model of computing the longitudinal tensile strength because the failure modes are different. Assuming that, the magnitude σ1 of the longitudinal compressive stress is applied, then the longitudinal compressive strain magnitude is presented by;

$$|\varepsilon_1| = \frac{|\sigma_1|}{E_1} \quad (2.52)$$

The major Poisson's ratio is v_{12}, the transverse strain is tensile and is presented by

$$|\varepsilon_2| = v_{12} \frac{|\sigma_1|}{E_1} \quad (2.53)$$

By using the maximum strain failure theory, when the transverse strain overtakes the ultimate transverse tensile strain $(\varepsilon_2^T)_{ult}$, the lamina can be considered to have failed in the transverse direction. So;

$$(\sigma_1^c)_{ult} = \frac{E_1(\varepsilon_2^T)_{ult}}{v_{12}} \quad (2.54)$$

The value of $(\varepsilon_2^T)_{ult}$, can be using the empirical formula;

$$(\varepsilon_2^T)_{ult} = (\varepsilon_m^T)_{ult}(1 - V_f^{1/3}) \quad (2.55)$$

Or the mechanics of materials formula;

$$(\varepsilon_2^T)_{ult} = (\varepsilon_m^T)_{ult}[\frac{d}{s}(\frac{E_m}{E_f} - 1) + 1] \quad (2.56)$$

Where

$(\varepsilon_m^T)_{ult}$ ultimate tensile strain of the matrix
d diameter of the fibers

s center to center spacing between the fibers

The fiber microbuckling failure mode of shear/extensional: the local buckling model for calculation of longitudinal compressive strengths have been developed [21,22]. Because the results are depended on advanced topics, only the final expressions are presented:

$$(\sigma_1^c)_{ult} = \min [S_1^c, S_2^c] \tag{2.57}$$

Where

$$S_1^c = 2[V_f + (1 - V_f)\frac{E_m}{E_f}]\sqrt{\frac{V_f E_m E_f}{3(1-V_f)}} \tag{2.58a}$$

$$S_2^c = \frac{G_m}{1-V_f} \tag{2.58b}$$

The lamina maximum shear stress under a longitudinal compressive load σ_1^c is $(\sigma_1^c)/2$ at 45° to the loading axis. So;

$$(\sigma_1^c)_{ult} = 2[(\tau_f)_{ult}V_f + (\tau_m)_{ult}V_m] \tag{2.59}$$

3 Transverse Tensile Strength

Estimation of the transverse tensile strength of a unidirectional lamina assume the model is;

- Bond of fiber-matrix has a perfect.
- Fibers have uniform spacing
- Hooke's law is applied to the fiber and matrix
- There are no residual stresses

It assumes that the lamina transverse failure is depend on the matrix failure, the ultimate transverse failure strain is presented by;

$$(\varepsilon_2^T)_{ult} = [\frac{d}{s}\frac{E_m}{E_f} + (1 - \frac{d}{s})](\varepsilon_m^T)_{ult} \tag{2.60}$$

Where $(\varepsilon_m^T)_{ult}$ ultimate tensile failure strain of the matrix.

The ultimate transverse tensile strength is then presented by

$$(\sigma_2^T)_{ult} = E_2(\varepsilon_2^T)_{ult} \tag{2.61}$$

4 Transverse Compressive Strength

Can be applied the equation (2.61) for computation of the transverse compressive strengths of a lamina. The actual compressive strength is again lower due to imperfect fiber/matrix interfacial bond and longitudinal fiber splitting. Using compressive parameters in Equation (2.61),

$$(\sigma_2^C)_{ult} = E_2(\varepsilon_2^C)_{ult} \tag{2.62}$$

Where

$$(\varepsilon_2^C)_{ult} = [\frac{d}{s}\frac{E_m}{E_f} + (1 - \frac{d}{s})](\varepsilon_m^C)_{ult} \tag{2.63}$$

$(\varepsilon_m^C)_{ult}$ =ultimate compressive failure strain of matrix.

5 In-Plane Shear Strength

The estimation of the ultimate shear strength for a unidirectional lamina using a mechanics of materials approach. Assume the shear stress applied to the magnitude τ_{12} .
The ultimate shear strength is then given by;

$$(\tau_{12})_{ult} = G_{12}(\gamma_{12})_{ult}$$
$$= G_{12}[\frac{d}{s}\frac{G_m}{G_f} + (1 - \frac{d}{s})](\gamma_{12})_{mult} \quad (2.64)$$

2.4 Transient Structure Analysis

The solution method utilized of transient analysis relies on the DOFs involved. Structural, acoustic, and other second order systems (the systems are second order in time) are resolved utilizing one method and the thermal, magnetic, electrical and other first order systems are resolved utilizing another. Each method is described subsequently. The analysis which is containing both first and second order DOFs such as structural and magnetic, each DOF is resolved utilizing the suitable method. For matrix coupling between first and second order influences as for piezoelectric analysis, a combined procedure is utilized.

The determination of the dynamic response of a structure under the action for all types of various loads with time, that's the transient dynamic analysis. For the most structural dynamics problems of a mechanical system, the spatial discretization for the principle of virtual work using the finite element method gives the finite element semi-discrete equation of motion as follows [79]:

$$[M]\{\ddot{u}(t)\} + [C]\{\dot{u}(t)\} + \{F^i(t)\} = \{F^a(t)\} \quad (2.65)$$

Where: $[M]$ Structural mass matrix.

$[C]$ Structural damping matrix

$\{\ddot{u}(t)\}$ Nodal acceleration vector

$\{\dot{u}(t)\}$ Nodal velocity vector

$\{u(t)\}$ Nodal displacement vector

$\{F^i(t)\}$ Internal load vector

$\{F^a(t)\}$ Applied load vector

There are three methods using to solve equation (2.65) as it is mentioned in the reference [79]:

- Central difference time integration method – Used for explicit transient analyses only
- Newmark time integration method – Used for implicit transient analyses
- HHT time integration method – Used also for implicit transient analyses. This method is an extension of the Newmark time integration method.

The structural dynamics problems involved with the mechanical behavior administered by the differential equation can be categorized two classes; which are, linear and nonlinear problems.

2.4.1 Time Integration Scheme for Linear Systems

In the linear structural dynamics systems, the internal load is linearly proportional to the nodal displacement, and the structural stiffness matrix remains constant. Therefore, equation (2.65) can be rewritten as following [79]:

$$[M]\{\ddot{u}(t)\} + [C]\{\dot{u}(t)\} + [K]\{u(t)\} = \{F^a(t)\} \quad (2.66)$$

Where: $[K]$ Structural stiffness matrix

$\{u(t)\}$ Nodal displacement vector

Through direct time integration methods for numerical resolving of the finite element semi-discrete equation of motion in equation (2.66), many methods as the Newmark method in reference [80] and the Generalized-α method in reference [81] are integrated in the program. As the Generalized-α method recaptures the Wood-Bosak-Zienkiewicz method (also called WBZ-α method) in reference [82], the Hilber-Hughes-Taylor method (also called HHT-α method) in reference [83], and the Newmark family of time integration algorithms, the program permits you to gather advantage of one of these methods by designating vary input parameters, as explained both of the methods which are the Newmark method and Generalized HHT-α method in reference [79]. The transient analysis uses for determination a time-dependent displacement and structure response such as stresses, strains, and forces responding to transient loads.

CHAPTER THREE

GEOMETRY AND MATERIAL DESIGN OF COMPOSITE HAWT BLADE

3.1 Blade Geometry Design

3.1.1 Blade Airfoils Selection

There are many various airfoils shapes have been vastly used in wind turbine applications. Due to the fast grow in the wind power turbine sector, while the airfoils have been improved over the years. For the case of small scale wind turbine, the airfoils do not be as critical as for larger wind turbines. However, there are only a number of airfoil shapes that are proper for designing small scale wind turbines. The airfoils shapes of small scale wind turbines should be utilized at a low angle of attack, which the drag coefficient is much lower compared to lift coefficient. As example for airfoils are the S 8 series airfoils, these airfoils were designed by the National Renewable Energy Laboratory (NREL) in the USA, and use popular in stall-regulated wind turbine blades [84; 85].

Most of the airfoil families have being successfully utilized on commercial wind turbine blades. the wind turbines contained these kinds of airfoils provides a significant growing of energy production on account of less sensitivity to roughness influence, best lift-to-drag ratios, and, in the case of stall-regulated rotors, through the use of more swept area for a given generator size [86].

The NREL has examined and proved the results of all airfoils which are used in all wind turbines applications and provided only ones most efficient in use.
The table (3.1) shows the diameter of the suitable blade rotor and types of each airfoil family along with the corresponding airfoils contained each family from blade root to tip. The sizes of wind turbine generators utilize those airfoil families starting from 2 KW up to 1 MW depending on the length of the blade.

Table (3.1) NREL Airfoil Families [86]

Rotor Diameter	Airfoil Category	Type of the Turbine operation	Root	Primary	Tip
1-3 m	Thick	Variable speed	S835	S833	S834
3-10 m	Thick	Variable speed Variable pitch	S823		S822
10-20 m	Thin Thin Thick	Stall regulated Stall regulated Stall regulated	S807 S808 S821	S805A S805A S819	S806A S806A S820
20-30 m	Thick Thick Thick	Stall regulated Stall regulated Stall regulated	S811 S814 S815	S809 S812 S812	S810 S813 S813
20-40 m	- - -	Variable speed Variable pitch	S814 S815 -	S825 S825 -	S826 S826 S829
30-50 m	Thick	Stall regulated	S818	S816	S817
40-50 m	Thick Thick Thick	Variable speed Variable pitch Stall regulated	S818 S818 S818	S830 S830 S827	S831 S832 S828

Our rotor blade designs in 6 m length category, hence we select the three different airfoils and distributed along the blade. The airfoils distribute in the blade root, primary and tip regions. The set of three airfoils is defining a single blade with a variable cross section, such that the 'root' airfoil (S821) is the cross-section shape at the location of largest chord length, the 'primary' airfoil (S819) is the shape at 75% of the blade radius, and the 'tip' airfoil (S820) which occurs at 95% of the radius. The airfoils data are gathered from the NREL documents and are validated to be accurate with XFLR, and the figures (3.1), (3.2), and (3.3) show the Airfoil Profile of NREL S821, S819, and S820 respectively. Accurate with XFLR, and the figures (3.1), (3.2), and (3.3) show the Airfoil Profile of NREL S821, S819, and S820 respectively [87].

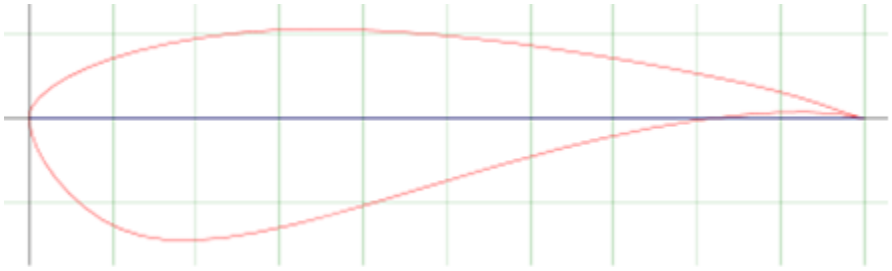

Figure (3.1) Airfoil Profile of NREL S821

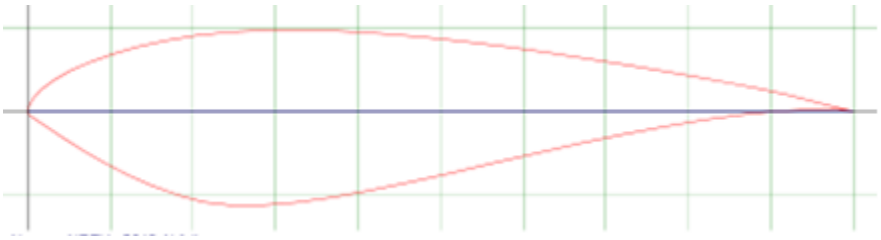

Figure (3.2) Airfoil Profile of NREL S819

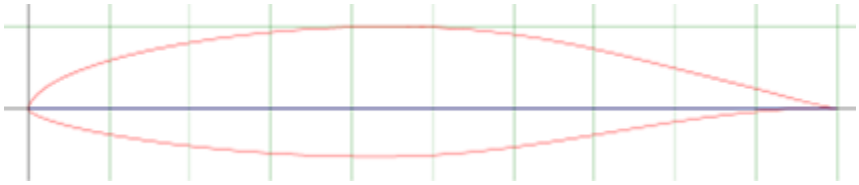

Figure (3.3) Airfoil Profile of NREL S820

3.1.2 Blade Geometry

The proposal of airfoils at the root of the blade is mainly structural, contributing to the aerodynamics performance of the blade but at a lower level. Thus the root of the blade is bigger and stronger than the other two airfoils used at the primary and tip regions. The airfoils closer to the tip of the blade generate higher lift due to speed variation in the relative wind [88].

The determination of the blade shape depends on the airfoils selection in the whole blade, which were designed for small scale wind turbine blade by CATIA V5R20 software. The Blade is 6.0 m long, it was divided into 13 sections and the ten sections starting from blade root is equaled, and it was twisted

from root section to tip, as shown in the figure (3.4). The shape distribution of the blade starts by circle in the hub, This circle transfers into own profile, then it transits to S821 in the root region, and it converts to airfoil S819 primary region of the blade, and then converting to airfoil S820 at the blade tip region in sequence as shown in table (3.2).

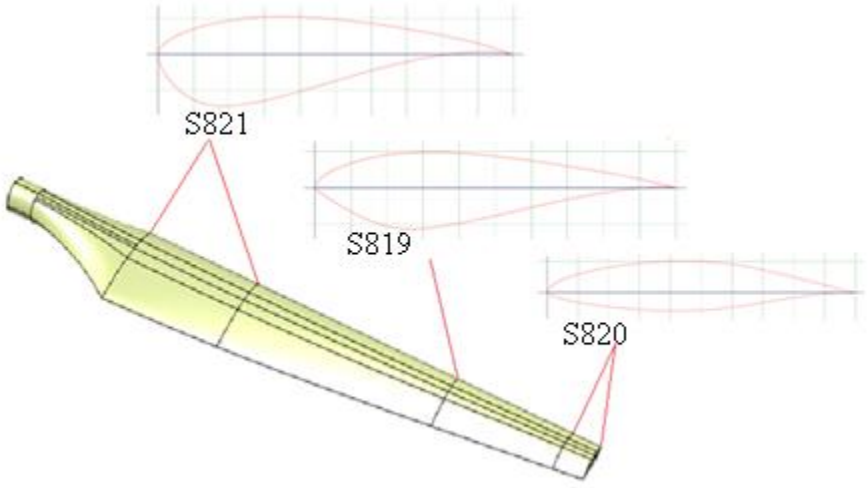

Figure (3.4): The Blade geometry in Catia

Table (3.2): the Blade sections of geometry

Station	Rotor Radius (mm)	Chord Length (mm)	Twist angle (deg.)	Airfoil Type
1	0	280	0	Circle
2	250	280	0	Circle
3	1275	800	16.82	S821
4	2400	684.7	8.76	S821
5	4500	469.3	2.46	S819
6	5700	346.3	0.47	S820
7	6000	315.5	0	S820

After the design of the blade geometry was completed, then the blade geometry is imported into computational fluid dynamics (CFD) analysis systems, That's important for the prediction of the blade aerodynamic performance at variation of wind conditions in order to obtain the distribution of pressure loads on the blade surface to use it in Static and transient Structural Analysis Systems.

3.2 Blade Composite Material Design

3.2.1 Material Modelling

The most important target of the thesis is a selection of the composite material to be bearing aerodynamic loads during the operation regime and at the same time minimize the blade weight to reduce the affective of ground gravity and centrifugal force. For that, it was used a technique of decreasing the blade weight by dividing the blade model into many sections and applied different thickness for each section according to the pressure force acting to that section.

The selection of blade composite material was studied of the five different unidirectional composite materials and epoxy resin at the same fiber volume fraction V_f =50%. The properties of fibers and matrix have used for obtaining composite materials properties in this dissertation as shown in the table (3.3). Then the properties of composite laminas (stiffness and strength parameters) were estimated to enter these data in optimization simulations. The estimation results of the fifth different composite materials are shown in the table (3.4).

Table (3.3) Initial Material Properties

Material Properties	E-glass Fiber[89]	T300 Carbon Fiber [89]	Kevlar49 Fiber [89]	Glass Fiber [78]	S2-glass Fiber[89]	Epoxy 5505 [89]
Young'sModulus(GPa)	72.4	231	124	85	87.9	7.24
Shear Modulus (GPa)	30.34	15	3	35.42	35.65	2.68
Poisson's Ratio	0.20	0.20	0.37	0.20	0.20	0.35
Density (kg/m^3)	2550	1760	1440	2500	2460	1265

Table (3.4) Blade Composite Material Properties

Stiffness and Strength Parameters	E-glass 5505 Epoxy	T300 Carbon 5505 Epoxy	Kevlar49 5505 Epoxy	Glass Epoxy	S2-glass 5505 Epoxy
Density[kg/m^3]	1907.5	1512.5	1352.5	1850	1862.5
E_1 [GPa]	39.824	119.12	65.62	46.12	47.625
E_2 [GPa]	20.06	14.04	7.47	13.343	21.07
G_{12} [GPa]	6.635	4.548	2.831	4.983	6.83
Poisson's Ratio	0.267	0.275	0.355	0.275	0.266
$(\sigma_1^C)_{ult}$ [MPa]	113.2	1090.5	104.20	69	1225
$(\sigma_1^T)_{ult}$ [MPa]	1183	1765	729.758	841.012	2295
$(\sigma_2^C)_{ult}$ [MPa]	108.78	189.29	99.632	45.906	171.71
$(\sigma_2^T)_{ult}$ [MPa]	26.58	63.3	27.639	26.957	57.426
$(\tau_{12})_{ult}$ [MPa]	55.35	69.05	80.408	40.606	67.27
Thickness[mm/ply]	0.32	0.32	0.32	0.32	0.32

In order to evaluate the stiffness parameters of composite materials, the finite element analysis was used. The following steps were used to design the unidirectional composite material in the material designer as follows; the fiber material and resin are added in the material file, the geometry model of the composite material was selected as a square cell. The model meshed with a maximum mesh size of 2 micrometers. In the next step, the composite material type was chosen as orthotropic and then analyzed the composite material parameters. The table (3.5) shows the analysis parameters of composite materials and can be compared these results with the results were calculated by equations which shows in the table (3.4).

Table (3.5) Blade Composite Material Properties (FEA)

Stiffness and Strength Parameters	E-glass 5505 Epoxy	T300 Carbon 5505 Epoxy	Kevlar49 5505 Epoxy	Glass 5505 Epoxy	S2-glass 5505 Epoxy
Density[kg/m^3]	1932.5	1512.5	1352.5	1882.5	1862.5
E_1 [GPa]	39.824	118.67	65.619	46.175	47.625
E_2 [GPa]	20.062	11.29	7.469	20.906	21.074
G_{12} [GPa]	6.635	5.581	2.719	6.821	6.829
Poisson's Ratio	0.267	0.275	0.355	0.266	0.266

3.2.2 Lay-up composite materials

Reference to literature survey focused on the layups composite material used for a wind turbine blades, the blades ply of fiber angle 0° and 45° are commonly used in wind turbine applications.

The layup of the composite material was used for the simulation of the fifth composite materials of the wind turbine blades through the blade sections, table (3.6) describes the layups of composite material used for each section of the wind turbine blades. There are two different ply fiber angle used 0° and 45° and their distribution in whole thickness for each section as it is shown in the table (3.6) with the thickness 0.32 mm and 0.16 mm respectively. The thickness of the composite material laminate of each section of the blade is presented later. The properties of five composite materials and the layups of blade composite material will be defined in the one-way and two-way coupling system (fluid-structural interaction) to compute the results of the static and transient analysis for different materials used. The simulations will perform in the same operation condition at cut-out wind speed operation and compared these results for select one of the composite material which will be suitable for the wind turbine operation.

Table (3.6) Composite Layups of Blade Elements

Blade Section	Radius (%)	Z Location (mm)	Layup Schedule	Thickness (mm)
Hub	4.0 to 8.0	250 – 500	$[+45/-45/0_5/+45/-45/0_5/+45/-45]_s$	8.32
Root	8.0 to 24.4	500 – 1525	$[+45/-45/0_5/+45/-45/0_4/+45/-45]_s$	7.68
Leading Edge	24.4 to 76	1525 – 4750	$[+45/-45/0_4/+45/-45]_s$	3.84
	76.0 to 100	4750 – 6250	$[+45/-45/0_3/+45/-45]_s$	3.20
Spar Caps	24.4 to 42.4	1525 – 2650	$[+45/-45/0_5/+45/-45/0_3/+45/-45]_s$	7.04
	42.4 to 76.0	2650 – 4750	$[+45/-45/0_4/+45/-45/0_3/+45/-45]_s$	6.40
	76.0 to 95.2	4750 – 5950	$[+45/-45/0_3/+45/-45/0_2/+45/-45]_s$	5.12
	95.2 to 100	5950 – 6250	$[+45/-45/0_3/+45/-45]_s$	3.20
Trailing Edge	24.4 to 95.2	1525 – 5950	$[+45/-45/0_4/+45/-45]_s$	3.84
	95.2 to 100	5950 – 6250	$[+45/-45/0_3/+45/-45]_s$	3.20
Shear Web	8.0 to 100	500 – 6250	$[+45/-45/0_3/+45/-45]_s$	3.20
End Cap	-		$[+45/-45/0_3/+45/-45]_s$	3.20

Reference to the data of the composite layups blade elements in the table (3.6), the Finite Element Analysis (FEA) is performed to estimate the tensile stiffness of blade laminates for examining the orientations of layup used to ensure that, the layup sequence used has the maximum tensile stiffness. For the prediction of laminate tensile stiffness, the thickness of the laminate was used in FEA the maximum thickness which is located in the blade hub as an example of the layup sequence in the table (3.6) of Aramid (Kevlar 49) epoxy 5505 with the volume fraction 50%. The Stack layup sequence starts by the layup of blade hub in the table (3.6) and then it was added 15 degrees increment as follows:

1. $[45/-45/0_5/45/-45/0_5/45/-45]s$
2. $[60/-30/15_5/60/-30/15_5/60/-30]s$
3. $[75/-15/30_5/75/-15/30_5/75/-15]s$
4. $[90/0/45_5/90/0/45_5/90/0]s$
5. $[-75/15/-30_5/-75/15/-30_5/-75/15]s$
6. $[-60/30/-15_5/-60/30/-15_5/-60/30]s$
7. $[-45/45/0_5/-45/45/0_5/-45/45]s$

The simulation of the tensile stiffness was performed and according to the results of force reaction of each sequence, layups can be computing the tensile stiffness of each. The results of tensile stiffness are plotted in the figure (3.5) and it shows that the maximum layup tensile stiffness is for layups sequence 1 and 7.

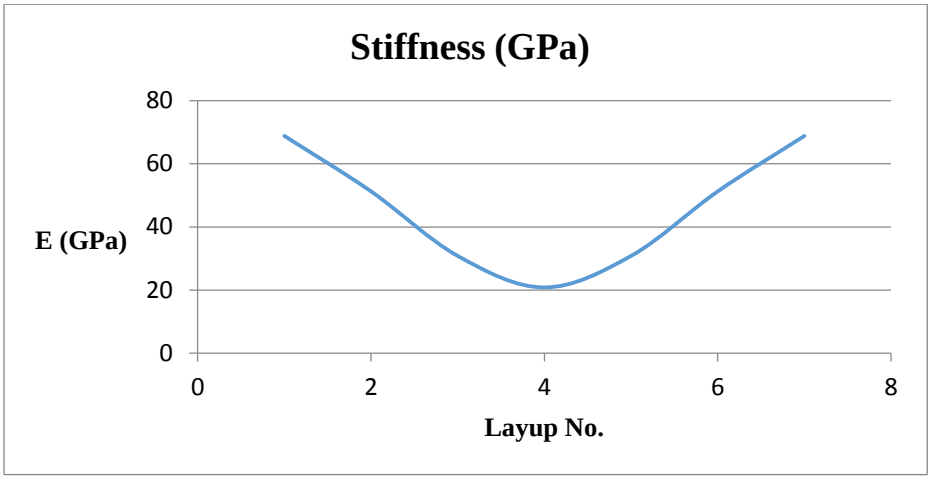

Figure (3.5) Tensile Stiffness for Different Layups Sequence

3.2.3 FEA Modeling For Static and Transient Structural Analysis

The fluid-structural interaction code was used to perform the simulation of the static and transient structural analysis for the five different composite materials properties are shown in the table (3.4) at the cut-out wind speed 25 m/s which is maximum aerodynamic load acting on the wind turbine blades among the operational wind speeds. The physical setup of the fluent in static and transient is the same which was used for the fluid-structural interaction of wind speeds operating later for the composite material was selected. The comparison of the blade composite materials was based on the four main results factors of structural analysis as follows:

1. Maximum Normal (Direct) stress
2. Maximum shear stress
3. Total deformation
4. Blade weight

Through the analysis of the results of the composite materials used, the comparison of the maximum direct stress was implemented for each composite material to their ultimate stress, also for maximum shear stress, the blade tip deformation, and the blade weight. The composite material was chosen the Aramid (Kevlar 49)/Epoxy 5505 based on the analysis factors mentioned above. The results analysis of static and transient structural are discussed later for five different composite materials used in the fluid-structural interaction simulation.

3.3 Finite Element Analysis of Laminates Tensile Stiffness

3.3.1 Material Modeling

As it will be a discussion later, the composite material selection was aramid (Kevlar 49)/ Epoxy 5505 reinforced composite material with the volume of fraction 50%. Tensile stiffness of laminates applied in two different blade sections was estimated that were the maximum and minimum of blade section thickness which are the Hub and Spar cap 4 sections, and there the thickness of each one is 8.32 mm and 3.20 mm respectively.

Composite material layups sequences mentioned in the table (3.6) were used in Finite Element Analysis for both section the hub and spar cap 4 because they are the maximum and minimum thicknesses, respectively. The blade composite material is Armada (Kevlar 49)/Epoxy 5505 which was used on the finite element method for test the tensile stiffness of laminates. The Kevlar 49 reinforced composite was modeled according to the specimen of the ASTM standard D638-14 [90].

The specimen model is applied to an ASTM standard D638-14 which was used in the finite element analysis to estimate the tensile stiffness of laminates for two sections. These two sections of the blade have a different thickness and based on the standard specification of ASTM standard D638-14, the dimension of the specimen is defined according to its thickness, so the dimension of each specimen is described in the figures (3.6) and (3.7).

3.3.2 Specimen Geometry

The two specimens model was designed by surface design mode in the CATIA V5R20 software and according to the standard dimension of the specimens in the reference [90]. The geometry of the specimen was imported to the finite element method as shown in the figures (3.6) and (3.7) to perform the tensile stiffness of both thicknesses.

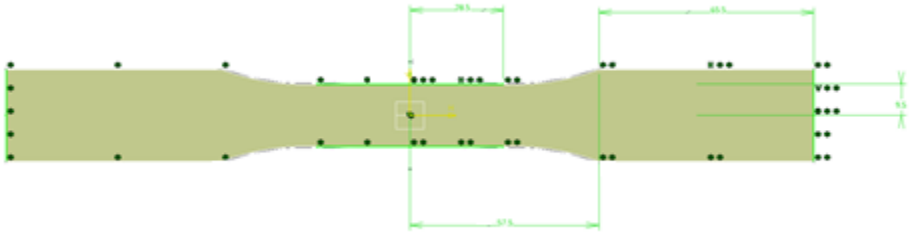

Figure (3.6) Specimen I Standard Dimension of D638-14 for 7 mm or Under

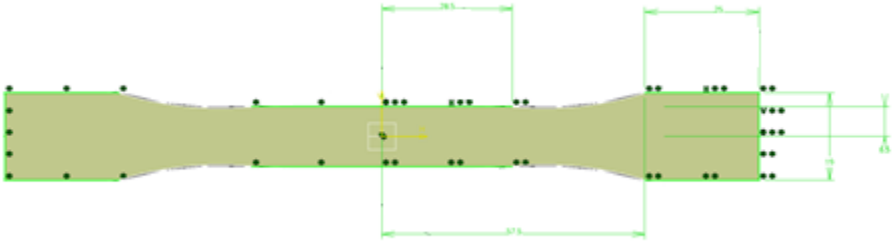

Figure (3.7) Specimen II Standard Dimension of D638-14 Over 7 mm to 14mm

3.3.3 Finite Element Analysis

Once the geometry is imported into the finite element method, the composite material properties are defined used which is the Armada (Kevlar 49)/Epoxy 5505 and applied the mesh into the specimen by using mesh size 4 mm as described in the figure (3.8). Moreover, the composite layup is defined and the lamina thickness, etc. The figures (3.9) and (3.10) describe the polar stack-up properties for two different specimens, the letters (a) and (t) appearing in both of the figures are the layer angle and thickness respectively. Figures (3.11) and (3.12) demonstrate the ANSYS Composite Pre-post (ACP) composite model with the fiber direction of 0° ply.

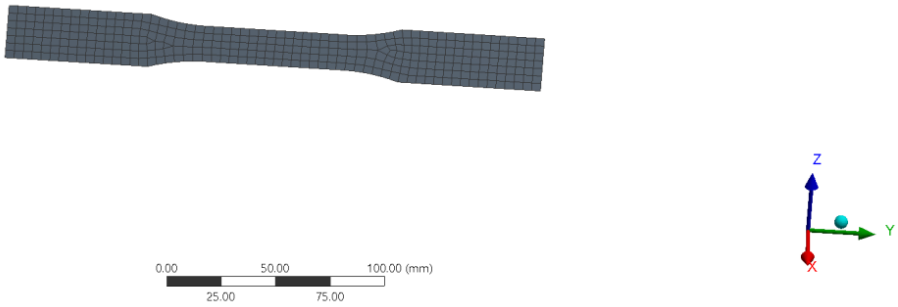

Figure (3.8) Specimen Mesh

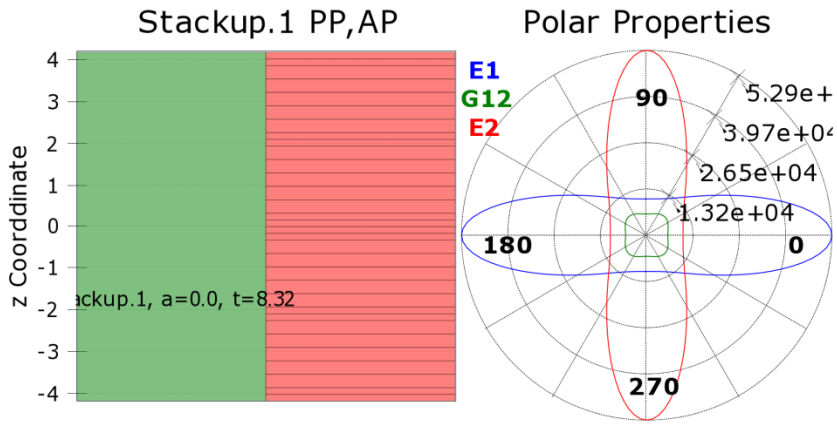

Figure (3.9) Polar Stack-up Properties Specimen I

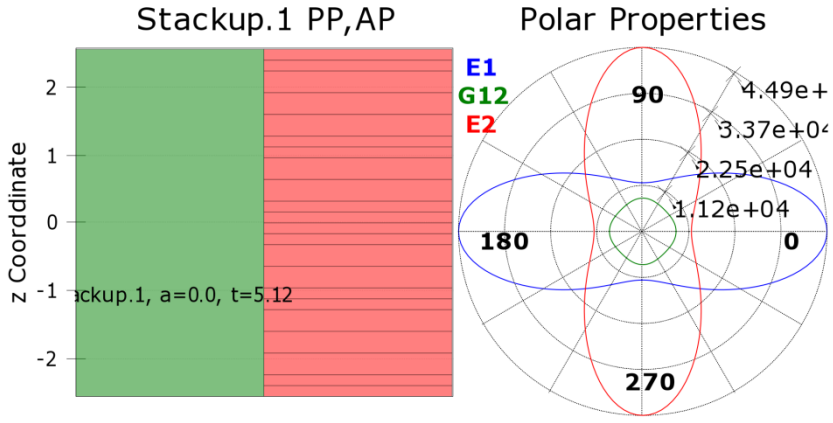

Figure (3.10) Polar Stack-up Properties Specimen II

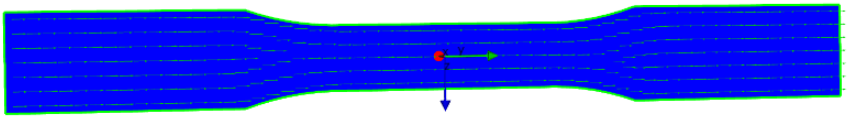

Figure (3.11) The ACP composite model with fiber direction (Y axis) Specimen I.

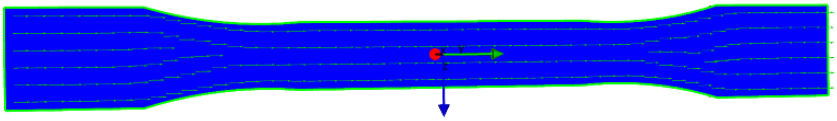

Figure (3.12) The ACP composite model with fiber direction (Y axis) Specimen II.

After it is finished the definition steps of ACP for laminate composite, the finite element analysis is used to estimate the laminate tensile stiffness, the finite element analysis setting was applied of the specimen. The simulation was implemented for both specimens according to the maximum and minimum thickness were applied on the blade sections.

3.3.4 Results and Discussion

In order to estimate the laminate tensile stiffness, a finite element analysis was used. In this analysis, the deformation and force reaction in the direction of tensile were achieved, and according to that, the simulation results were presented in the table (3.7). The FEA results show the deformation and force reaction in both specimens were symmetric configuration. The deformation results of two specimens are shown in the figures (3.13) and (3.14) for specimen I and specimen II, respectively.

Table (3.7) Simulation Results

	Specimen I		Specimen II	
	Min	Max	Min	Max
Deformation (mm)	0	0.25	0	0.165
Force Reaction (N)	11060		3705.6	

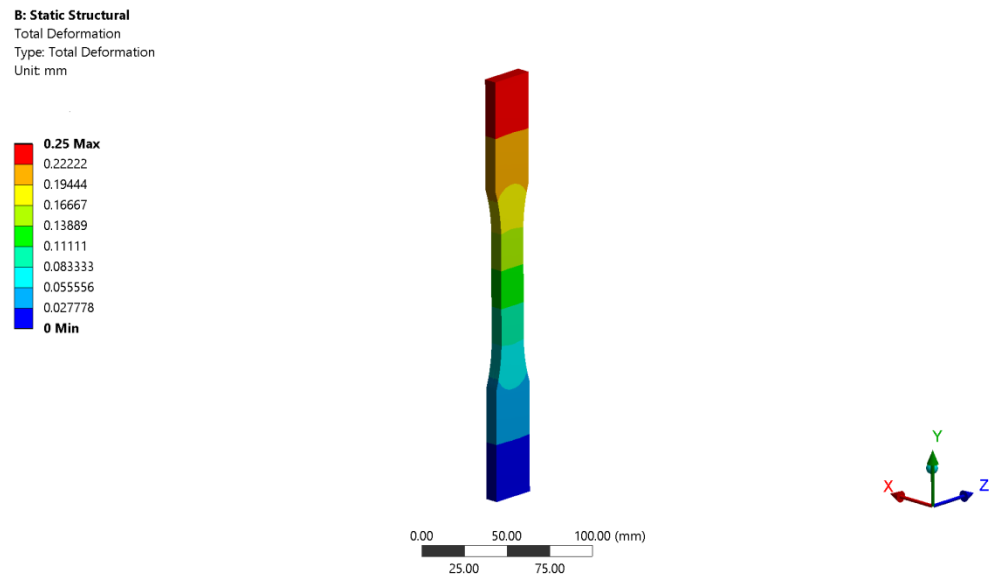

Figure (3.13) the Deformation of Specimen I

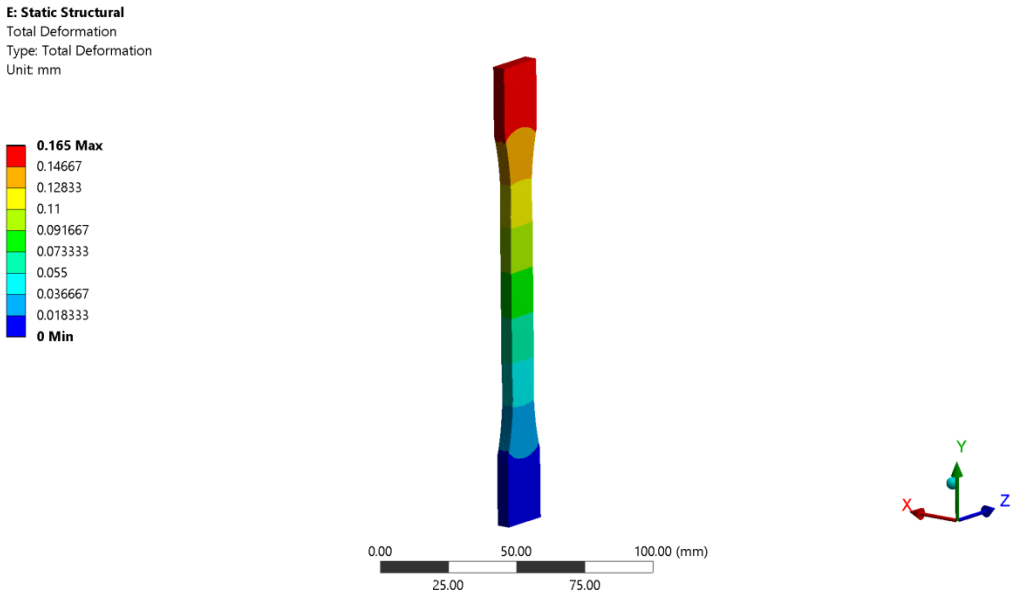

Figure (3.14) the Deformation of Specimen II

The results of force reaction achieved for both specimens from finite element analysis, and according to that results can calculate the nominal stress and tensile stiffness of the composite material which is their results shown in the table (3.8). The calculations procedure of both the nominal stress and tensile stiffness are described in Appendix ( ).

Table (3.8) Tensile Stiffness of Two Specimens

	Nominal Stress (MPa)	Tensile Stiffness (GPa)
Specimen I	69.965	68.846
Specimen II	55.673	55.673

3.4 Influence of Material Flaw

3.4.1 Introduction

The development and application of porous structural materials is motivated by the continuous demand in different fields of possible applications. For instance, in a field of structural engineering there is a demand for lightweight constructions with enhanced mechanical properties. In the other hand, in the field of medicine, porous biocomposites are used as bone replacement in implant surgery. Therefore, different porous materials have been used in a wide range of applications in various engineering structures such as ceramics and bioceramics, porous shape memory alloys, foam-like structures and thermal spray deposits. But presence of porosity usually degrades mechanical properties of structural material [91]. Fact that porosity reduces the mechanical properties is important when material is used as structural member carrying some load. In this case porosity is considered as a flaw which generally causes a decrease in the mechanical properties of structural material such as: strength, stiffness, etc. As defined in metallographic studies, pores can be mainly classified as: closed round pores, long and broad pores, long and fissured pores, and small, fissured pores [92].

When presence of porosity is evident, mechanical properties of structural materials are strongly influenced by microstructure of pores size and shape. This impact were in focus of number of the prior studies which confirmed the fact that less porosity in the material microstructure leads to higher material stiffness and strength, while an irregular shape of pores strongly influences the material fracture toughness and strength [93-97]. It should be emphasized that sometimes presence of porosity is quite necessary and desirable. In implant surgery porous materials have been shown to effectively provide stable long-term anchorage for biological fixation of the implant due to bone tissue ingrowth through the pores [98]. Nielsen [99] developed a number of empirically based relations between stiffness (modulus of elasticity) and strength (modulus of rupture) of materials has been established in order to control quality without damaging or destroying the material or the building component considered. Some theoretical methods have been developed to correlate porosity size and shape and material stiffness and strength. A detailed summary of these methods could be found in and Wang and Tseng [100].

Through past decades numerical modeling became a powerful tool for studying influence of microstructure on mechanical properties for different types of materials. Three dimensional Unit Cell Approach is widely used for simulating real microstructure of different types of materials. In the Unit Cell Approach, real microstructure having random distribution of pores shape and size is idealized by periodically distributed pores of the same shape and size which are represented by a periodic repeating cell which is usually simple cube. The Unit Cell Approach requires relatively little computational efforts in comparison to simulations of real structures. For instance, in some prior studies the Unit Cell Approach was used to investigate the effect of the mutual arrangement of phases in different composite materials [101,102] and to study effect of structural porosity on the mechanical and elastic properties of sintered materials [103,104].

In this study, address is on low level porosity in form of closed round pores and their influence on strength of structural materials by using proposed UCNM. A face-centered-cubic (FCC) finite element (FE) unit cell model which was previously designed to evaluate the compressive stiffness and strength of biocomposite material for a range of porosity volume fractions [101] is used here for simulating spherical geometry of pores. An extension of FCC model is developed to simulate non-spherical geometry of pores.

3.4.2 Modeling Procedure

Typical example of microstructure of porous material is SEM micrograph of HAP sample sintered at 1250ºC for 2h – Figure (3.15) (a) [104]. Sintering usually leads to a denser microstructure, with closed pores and parts of well sintered grains. To fully simulate such a microstructure, a three-dimensional (3D) model of a random distribution of pores shape and size is required. The present study aims at carrying out an influence of closed pores shape and size on strength of structural materials. In this study, distribution of pores is idealized by face-centered-cubic arrange of pores where there is one spherical pore at each corner and one spherical pore centered in each face of the cube cell as shown on Figure (3.15) (b). With assumption of isotropic material properties, for analysis in this study, one eighth of original unit cell is used – Figure (3.15) (c). The irregular shape of porosity appearing in real microstructure, is idealized as ellipsoid geometry shape (Figure (3.15) (d)) with chosen orientation, aligned with main coordinate axe *z*. Aspect ratio of pores - AR, defined as diameter to diameter ratio – $AR=D_1/D_2$, were chosen to be 1 (sphere), 2, and 3 respectively, while volume fraction of porosity (V_p) is

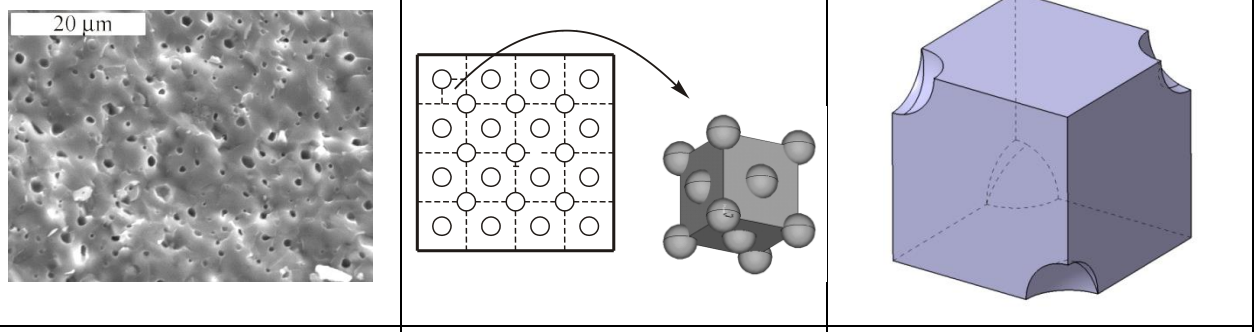

(a) (b) (c)

Figure (3.15) Idealization of the random pore distribution, shape and size by arranging the pores of same size and same shape (sphere) on a FCC packing array.

chosen to be 3, 5 and 7 percent respectively. Unit cell is loaded by compression in vertical direction (NL load case) or horizontal direction (PL load case). Symmetry of geometry and load potentially allows unit cell to be reduced to the one eighth of original unit cell as shown on Figure (3.16).

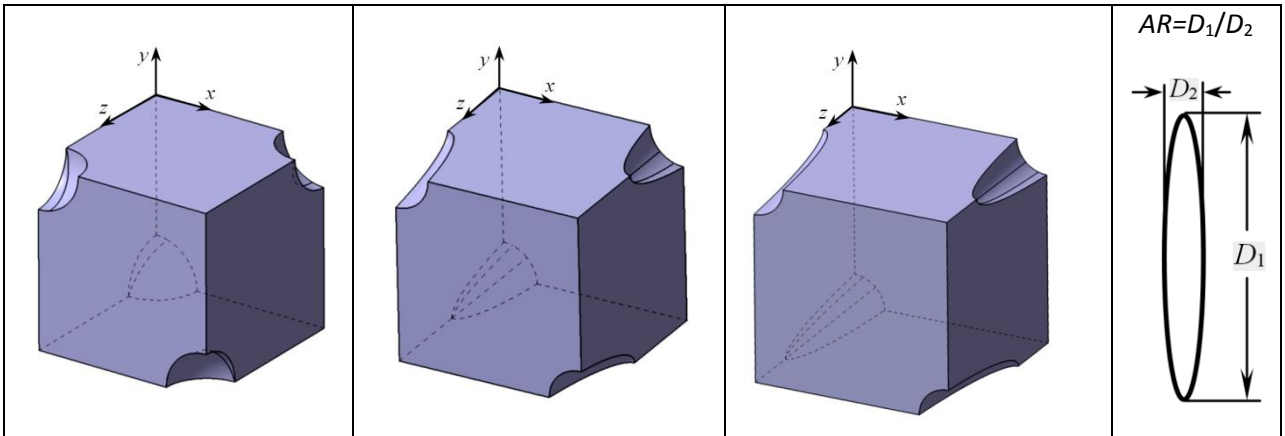

(a) (b) (c) (d)

Figure (3.16) UCNM with 3% of porosity volume fraction (V_p): (a) AR=1, (b) AR=2, (c) AR=3 and (d) dimensions of ellipsoid (D_1, D_2 - principal axe diameters).

The assumptions for all models are: (a) the elastic properties of material are linear, (b) the material is isotropic, (c) in every model, all sphere and ellipsoid like pores are of the same size, (d) the material will not fail at the prescribed loads and (e) pores do not intersect each other.

Due to the symmetry of the unit cell and the applied loads, as well as adopted isotropic material properties, analysis were reduced to one eighth of the unit cell for all models as shown on Figure (3.16) (a,b,c). Dimensions of reduced unit cells presented at Figure (3.16) are: 10×10×10μm.

All 3D finite element (FE) models were produced using ANSYS 16.4, a general purpose FE software package for structural analysis. The elements used in analysis are 10-node tetrahedral structural solid elements (an option of 20-node solid brick elements). Each node has three degrees of freedom corresponding to the three degrees of translation. Boundary conditions constrain the unit cell to remain in its original shape. After loading, the sides remain parallel and orthogonal, but changes in length. Load was introduced in form of displacement in vertical or in horizontal direction. In the vertical load case (NL) nodes positioned at upper surface of the cube (y=0μm) were displaced by Δ_y=-0,01 μm in vertical direction while nodes positioned at lower surface of the cube (y=-10μm) were constrained by displacement in y direction. In horizontal load case (PL) nodes positioned at side surface of the cube (z=10μm) were displaced by Δ_z=-0,01 μm in horizontal direction while nodes positioned at z=0μm were constrained by displacement in z direction. The local coordinate system aligns with the global one.

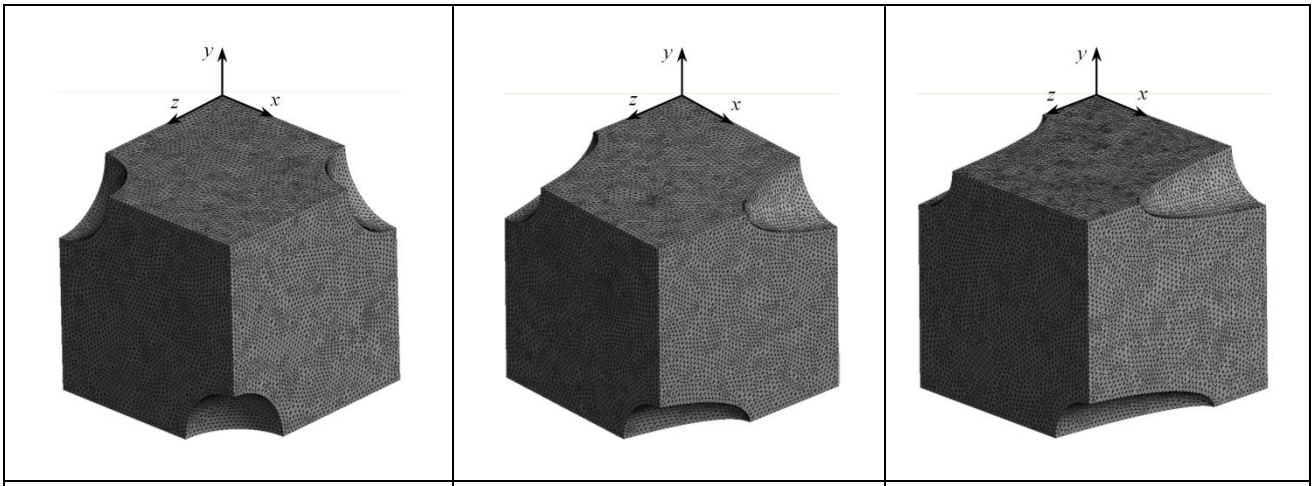

(a) (b) (c)

Figure (3.17) Finite element grid of unit cell with 5% of porosity volume fraction (V_p): (a) AR=1, (b) AR=2, (c) AR=3.

A representative FE grid for evaluation of compressive strength with porosity volume fraction V_p =5%, shown in Figure (3.17) (a), contains 116513 elements and 169724 nodes. The material data used for FE analyses, adopted based on literature data [101], with following values: E= 16.04 GPa, ν=0.124, where E is Young's modulus and ν is Poisson's ratio. After loading, maximum equivalent stress is divided by nominal stress (stress in non-porous material) to obtain stress concentration factor SCF:

$$\mathrm{SCF} = \frac{\sigma_{max}}{\sigma_{nominal}} \qquad \text{..... (1)}$$

Higher values of SCF can dramatically lower strength of structural material. Therefore there is a need to investigate how porosity volume fraction and porosity shape influences on SCF of structural material.

3.4.3 Results and Discussion

Results presented in this section are obtained numerically with assumptions for ideally elastic material adopted in previous section.

Summary of obtained results (maximal and nominal stress and SCF) for different AR (1, 2, and 3) and different V_p (3%, 5%, and 7%) for PL load case are presented at Table (3.9) PL load case refers to load applied parallel to direction of pores.

Table (3.9) Summary of obtained results for SCF for different AR for PL load case.

AR = 1			
Porosity volume fraction V_p(%)	3	5	7
Maximal stress (MPa)	391,43	390,18	375,01
Nominal stress (MPa)	190,04	181,11	173,35
SCF	2,059	2,166	2,161
AR = 2			
Porosity volume fraction V_p(%)	3	5	7
Maximal stress (MPa)	308,17	363,59	403,39
Nominal stress (MPa)	195,16	188,35	181,48
SCF	1,579	1,93	2,223
AR = 3			
Porosity volume fraction V_p(%)	3	5	7
Maximal stress (MPa)	244,34	273,8	289,19
Nominal stress (MPa)	195,64	190,07	184,76
SCF	1,249	1,44	1,565

Comparison of obtained values of SCF from equation (1) for different AR for load parallel to direction of pores – PL load case is presented in Figure (3.18).

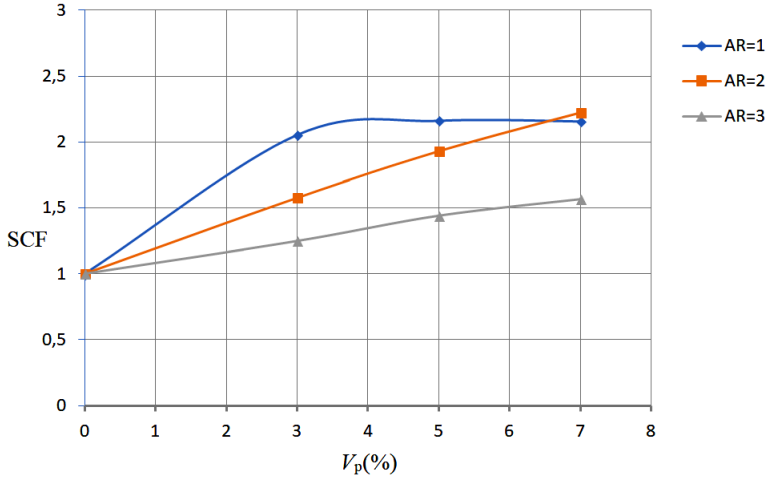

Figure (3.18) Comparison of obtained values of SCF for PL load case for different fixed aspect ratios and for different porosity volume fractions - V_p.

Summary of obtained results (maximal and nominal stress and SCF) for different AR (1, 2, and 3) and different V_p (3%, 5% and 7%) for NL load case are presented at Table (3.10) NL load case refers to load applied normal to direction of pores.

Table (3.10) Summary of obtained results for SCF for different AR for NL load case.

AR = 1			
Porosity volume fraction V_p(%)	3	5	7
Maximal stress (MPa)	391,43	390,18	375,01
Nominal stress (MPa)	190,04	181,11	173,35
SCF	2,059	2,166	2,161
AR = 2			
Porosity volume fraction V_p(%)	3	5	7
Maximal stress (MPa)	342,17	403,65	449,68
Nominal stress (MPa)	195,16	188,35	181,48
SCF	1,753	2,143	2,478
AR = 3			
Porosity volume fraction V_p(%)	3	5	7
Maximal stress (MPa)	270,17	303,91	332,75
Nominal stress (MPa)	195,64	190,07	184,76
SCF	1,381	1,599	1,801

Comparison of obtained values of SCF for different AR for load normal to direction of pores – NL load case is presented in Figure (3.19).

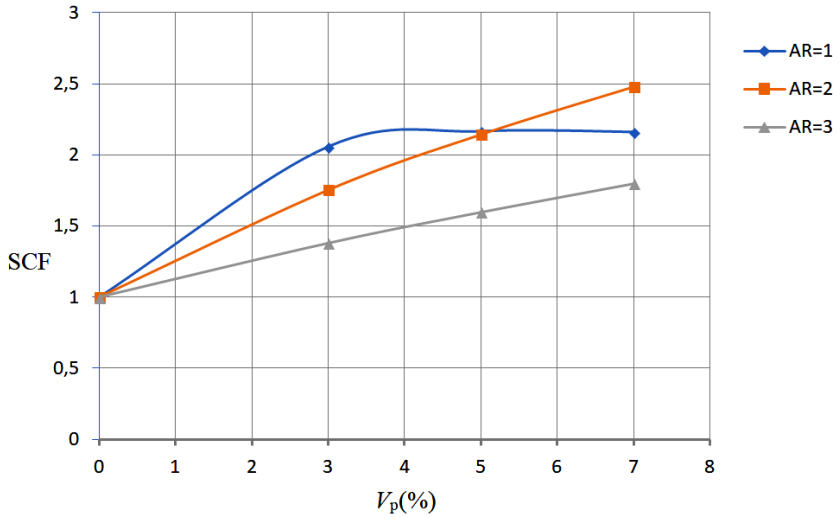

Figure (3.19) Comparison of obtained values of SCF for NL load case for different fixed aspect ratios and for different porosity volume fractions - V_p.

Additionally, obtained results for PL load case for AR=2 and AR=3 are compared to the experimental values available at literature [22], as presented at Figure (3.20). For comparison purposes normalized experimental strength $S_{nor.}^{exp.}$ is calculated from:

$$S_{nor.}^{exp.} = \frac{S_{por.}}{S_{nom.}} \quad \text{..... (2)}$$

Where $S_{nom.}$ is measured strength of non-porous material of sample, and $S_{por.}$ is measured strength of porous material sample.

Numerically obtained results for SCF were used for calculating estimated normalized strength as:

$$S_{nor.}^{est.} = \frac{1}{\text{SCF}} \quad \text{..... (3)}$$

As obvious from obtained results, for non-porous structural material SCF=1 and therefore $S_{nor.}^{est.} = 1$. For porous structural material, porosity influences the strength by the fact that increasing V_p is increasing SCF which in other hand is lowering the strength.

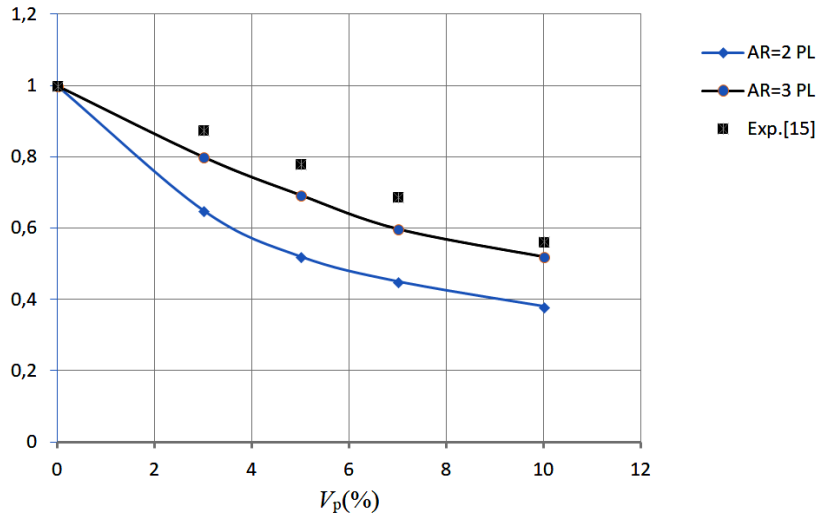

Figure (3.20) Comparison of obtained results for estimated normalized strength - $S_{nor.}^{est.}$ with normalized experimental strength $S_{nor.}^{exp.}$ (data from [105]).

As obvious from Figure (3.20) with the increase in porosity content strength observably decreases. For example, for PL load case and AR=3, presence of 5% of porosity leads to estimated decrease of strength for approximately 30%. For porosity of 7% estimated decrease of strength is approximately 40%. For this comparison additional numerical models having 10% of porosity with AR=2 and AR=3 (for PL load case) were made. Experimentally obtained values [105] are similar with values obtained numerically for PL load case and AR=3 within 10% difference. For all other aspect ratios and load cases estimated decreases of strength were much lower than the values obtained experimentally. It should be emphasized that SCF is important but not the only one parameter contributing to strength decrease in structural materials. Type of load, post-yield behavior, hardening low etc. are contributing to strength as well. Therefore these numerical models generally underestimate real values of strength in structural materials. Estimated values obtained by these models are always on the side of safety.

Figure (3.21) presents influence of pores shape (AR) to SCF for PL load case for different fixed porosity volume fractions - V_p. Figure (3.22) presents influence of pores shape (AR) to SCF for NL load case for different fixed porosity volume fractions - V_p. As it is evident from Figures (3.21) and (3.22), shape of porosity has an impact on strength. With increasing aspect ratio (AR) of pore for fixed porosity of 3% and 5% value of SCF is lowering. Same trend is observed for both load cases NL and PL. With increasing aspect ratio (AR) of pore for fixed porosity of 7% value of SCF has a light higher value for AR=2 while for AR=3 value of SCF is lower than the value obtained for AR=1. It can be concluded that this influence is moderate when comparing to influence of volume fraction which is clearly dominant.

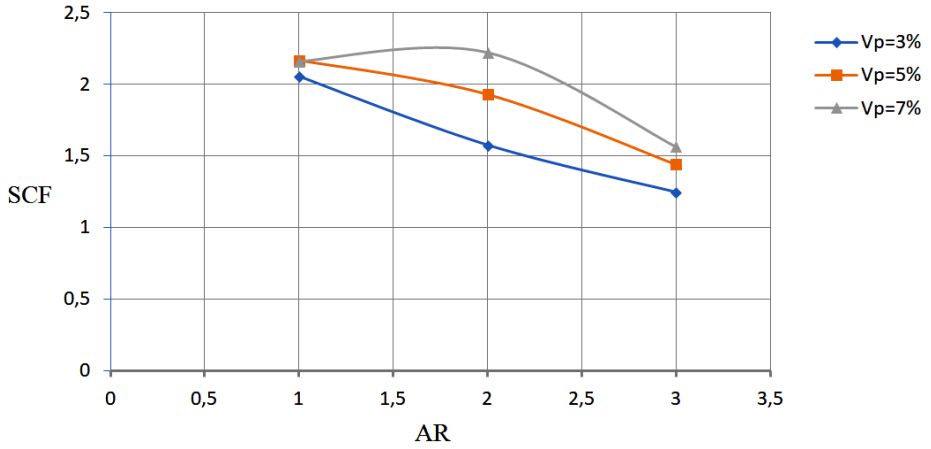

Figure (3.21) Influence of pores shape (AR) to SCF for PL load case for different fixed porosity volume fractions - V_p.

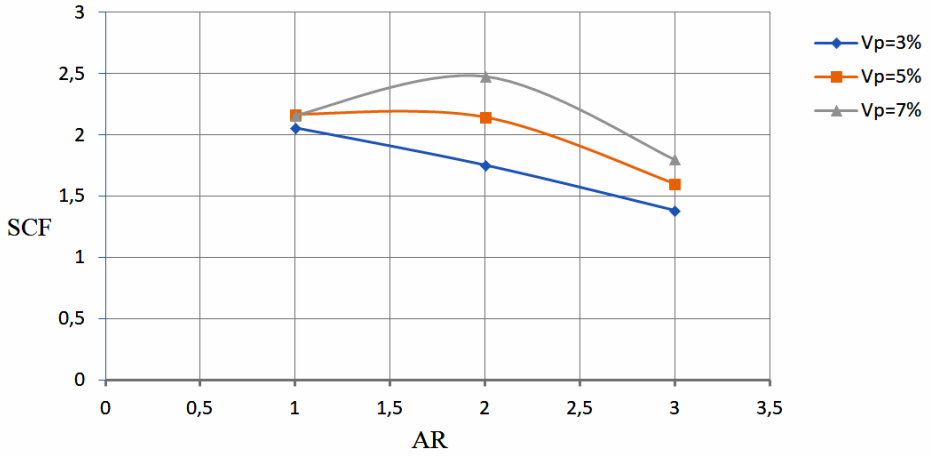

Figure (3.22) Influence of pores shape (AR) to SCF for NL load case for different fixed porosity volume fractions - V_p.

CHAPTER FOUR

COUPLED FLUID-STRUCTURE ANALYSIS

OF DESIGNED COMPOSITE BLADE

4.1 Fluid Flow (Fluent) Analysis "Pressure Load"

4.1.1 Computational Domain

The 3-D model of wind turbine contains three blades used which is symmetric, thus we selected one blade for numerical simulation has a length 6 m as shown in the figure (4.1). Rotational blade speed is defined at 76.4 RPM. The flow around the blade is turbulent flow. The blades are made of Aramid (Kevlar49) fiber reinforced layered composite.

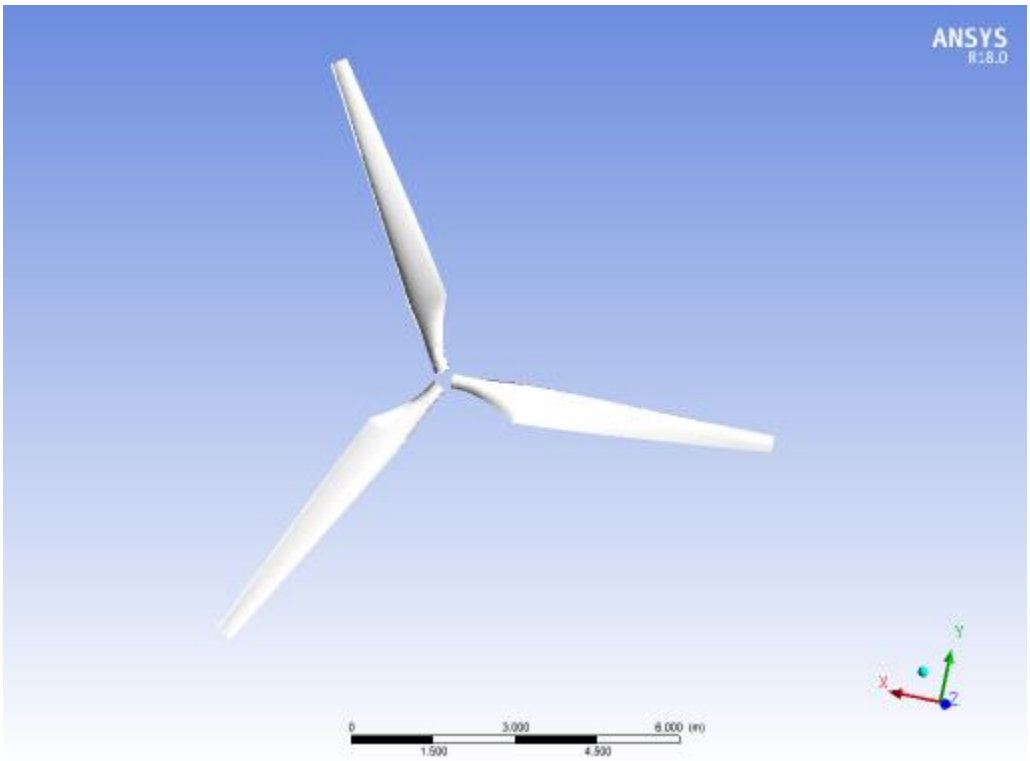

Figure (4.1) the Three Blades Wind Turbine Model

In this study for computation aerodynamic load on wind turbine blade is analyzed taking into respect an isolated blade with periodic boundaries, in order to make simulation a full three-blade rotor as much as a smaller domain, saving simulation time. For that, the 3-D domain is modeled as a semi-cylindrical section (conical shape) with a central angle of 120°. The domain inlet is planed 15 m ahead of the blade and the domain outlet 30 m behind the blade, and expands radially from the turbine axis of rotation to shroud at the 20 meters radius in the inlet, and 40 meters at the outlet, as shown in the figure (4.2). The mode Boolean operation is applied for removal solid blade from the fluid domain; hence it creates a void in place of the blade. This void in the fluid domain is appropriate to implement CFD simulation.

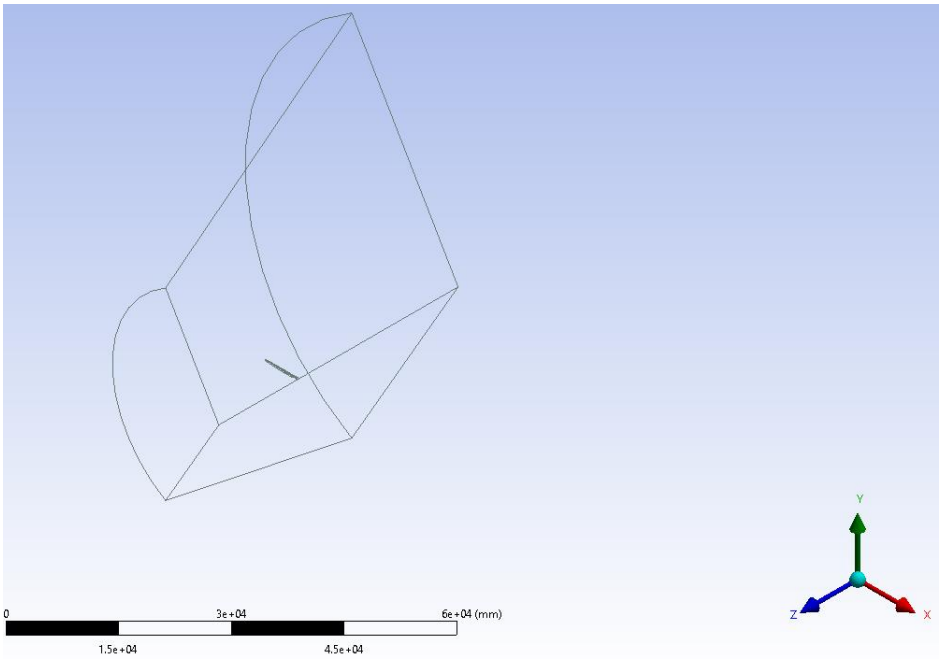

Figure (4.2) Fluent Domain of CFD

4.1.2 Numerical Mesh for CFD Computation

A number of local mesh controls have been applied to the numerical mesh for CFD computation to define the mesh feature in specific areas. The first model applied was the match control for matching the nodes for different surfaces. The second mode applied was inflation to specify cell size on the blade surface and captured the boundary layers on the object, these cells are hexahedral instead of tetrahedral as it's shown in the figure (4.3). The nodes number and elements of the mesh are 321685 and 222064, respectively. It is used inflation ratio setting 0.272 with a growth rate of 1.2. Figure (4.4) shows the fluid domain mesh implementation. Through the observation, the mesh transition is a smooth, and a very accurate and small near to contact surfaces. The mesh control applications have been performed for obtaining the appropriate solutions.

The inlet velocity of boundary conditions can be set to the wind velocity free stream. The outlet pressure of the boundary condition assigns at atmospheric pressure. The domain outer surface can assign by the same of main inlet velocity. the fluent domain selected to be a conical shape based on the results experimental which have described that wake expansion behind the blade is formed conically [106,107]. The blade is chosen as the stationary non-slip wall, and the computational domain is taken into consideration to be a rotation frame by specified the rotational speed. The periodic boundary condition is applied for the computational domain reduced the number of grids to enable finer grids as shown in the figure (4.2) one-third of the turbine.

The air viscosity is chosen to be 1.7894E-05 (kg/m.s) and the inlet turbulent intensity is 5%. In this study, the turbulence model is selected to be the k-ω shear stress transport (SST) model in the fluid solver. the most important features of the two-equation model developed by Menter [108] has the ability to transform from a k-ϵ turbulence model [109] appropriate of the simulation far-field flows to a k-ω turbulence model [110] appropriate to modeling the boundary layer. Most studies related to the wind turbine blades applications have utilized this model and obtained favorable results.

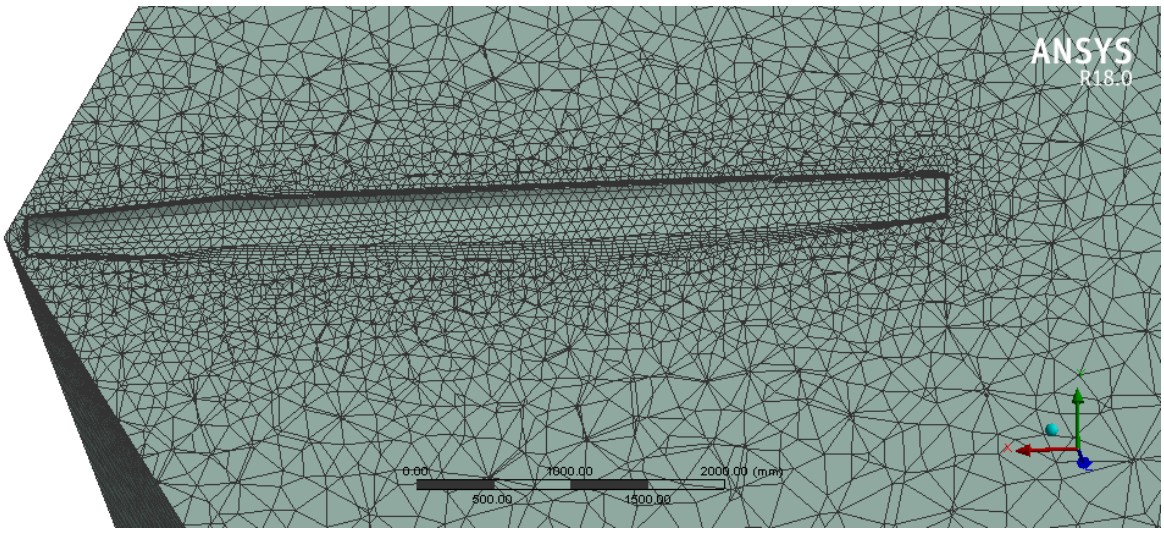

Figure (4.3) Inflation Layers on Blade Surface

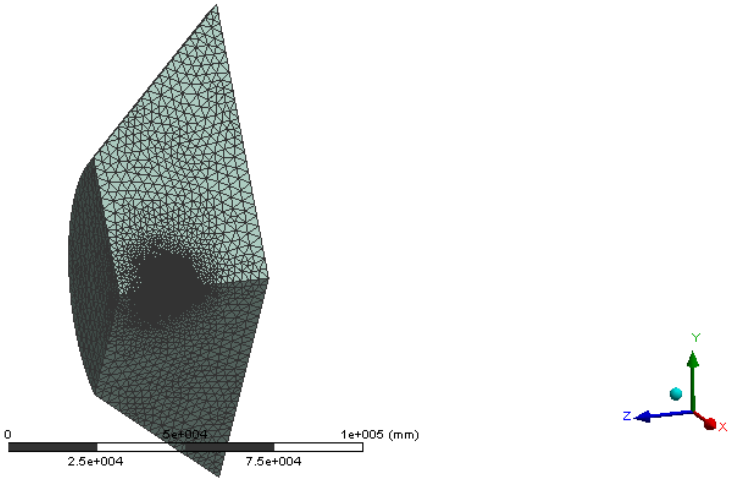

Figure (4.4): The Fluent Mesh

4.2 Fluid Flow (Fluent) Analysis "Transient Analysis"

4.2.1 Domain of CFD

the 3-D domains of CFD analysis are selected to be a 120-degree wedge model with one blade, the reason is minimized the computational time and simplified the CFD analysis, for that the assumption of the boundary conditions is symmetry on the both of domain sides, and each side was afforded periodic boundary conditions as shown in the figure (4.5). It means that the velocities step out from the left side boundary can be entering the boundary on the other side in an infinite loop [111]. The flow was supposed to be ideal, steady and homogenous. The selected turbulence model was k-w, SST (shear-stress transfer) for catching the turbulence phenomena. The inlet wind speed boundary condition was considered a fixed uniform entrance velocity. The boundary condition outlet was applied to a static pressure with a free stream wall. The surfaces of the blade were set as non-slip walls with rotation. As soon as the wind flows in the domain, the blade should rotate around the hub of the wind turbine, there were defined two subdomains. One is internal and the other one external domain, the internal domain

consists of the blade and rotates with it. The internal domain has the same central angle, the blade hub is positioned in the center point, and expands radially from the turbine hub to internal shroud at 6.6 meter radius, and axially from blade centered point 1.2 meter upstream and downstream, as shown in the figure (4.5). The internal domain is surrounded by a bigger external domain, stationary. It expands radially from the turbine hub to external shroud at 48 meter radius, and axially from blade centered point 24 meter upstream and downstream, as shown in the figure (4.5).

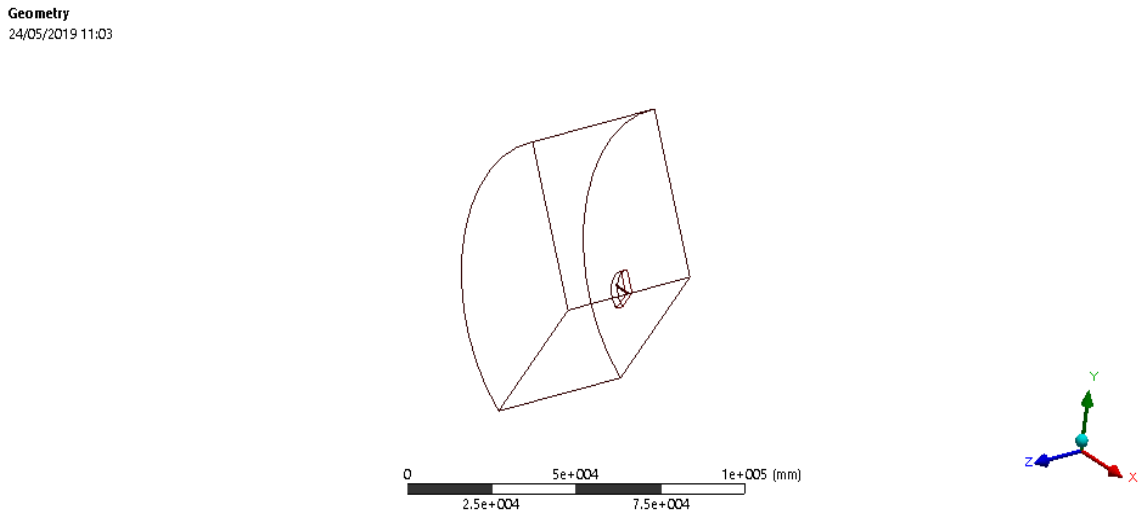

Figure (4.5) Internal and External Domain Geometry

The wind stream flows in negative Z-direction in the boundary system. Therefore, wind flow speed is considered a constant flow speed perpendicular to the inlet plane (black arrows in figure 4.6). The planes parallel to the inlet (outlet) and the external shroud were considered openings (blue arrows) to allow both the inflow and outflow. Both of two side walls were known as periodical boundaries. The hub was considered to be a free-slip wall in the external domain and as a no-slip wall in the internal domain.

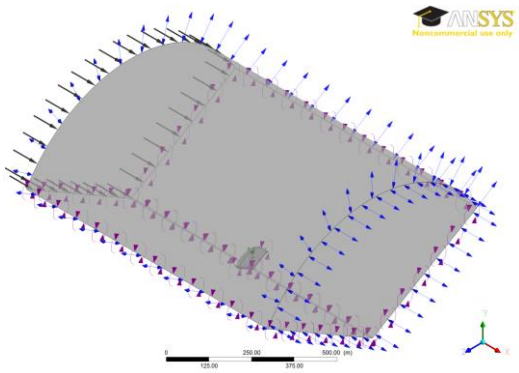

Figure (4.6) Domain Boundary Conditions

4.2.2 Mesh of CFD

Mesh density has different for both of two domains, the internal domain makes a much fine mesh to catch the significant gradients in the velocity and pressure for the wind stream flows near the blade. The external domain mesh is set to be a much coarser mesh to retain the total nodes a reasonable number for reducing the computational time simulation.

The transient structural component system was utilized the finite element analysis. The model of blade geometry which utilized in the computational fluid analysis (CFD) was participated with finite element (FEA). The CFD transient mesh was generated to be tetrahedral mesh elements of both domains (stationary and rotating domain) with total elements 1546304 and 2242235 nodes as shown in the figure (4.7). the rotating domain mesh was applied the body sizing 0.12 m for the blade, and also used a ten inflation layers around the blade with transition ratio 0.272 and growth rate 1.2. In this study, the wind turbine blade was modeled as a shell made from Kevlar 49 reinforced epoxy 5505 composite material.

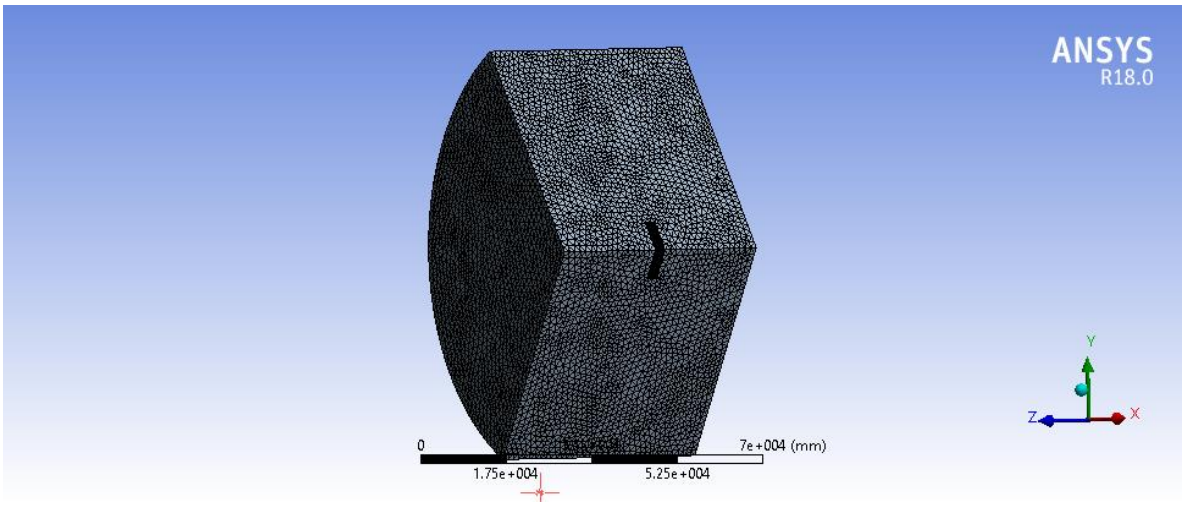

Figure (4.7) the Transient Fluent Mesh (Stationary and Rotating Domains)

4.3 Material Modeling

The composite material was chosen Aramid (Kevlar49) with epoxy 5505 at volume fraction V_f = 50% as it is mentioned on section of composite material selection in chapter 5, and used layups of the blade sections demonstrated in the table (3.4) in the composite material design section of chapter three. The Kevlar 49 epoxy 5505 composite material properties are utilized in the fluid-structural interaction ANSYS simulation for prediction the blade maximum normal (direct) stress, maximum shear stress, and maximum tip blade deformation during the wind speeds operating, and shown in the Table (4.1).

According to the blade geometry shown in the figure (3.4) can be observed that the blade structure consists of many sections, and applied the different stack-up (lay-ups) of each section of the blade as presented in the table (3.4), through the figure (4.8) describes polar properties composite material used for many of blade sections as an example to show the composite material properties in different angles

Table (4.1) blade Kevlar/Epoxy5505 composite material properties

Stiffness and Strength Parameters	Kevlar49 5505 Epoxy
Density (kg/m^3)	1352.5
E_1 [GPa]	65.619
E_2 [GPa]	7.472
G_{12} [GPa]	2.72
Poisson's Ratio	0.355
$(\sigma_1^C)_{ult}$ [MPa]	104.2
$(\sigma_1^T)_{ult}$ [MPa]	729.758
$(\sigma_2^C)_{ult}$ [MPa]	99.632
$(\sigma_2^T)_{ult}$ [MPa]	27.639
$(\tau_{12})_{ult}$ [MPa]	82.723
Thickness[mm/ply]	0.28

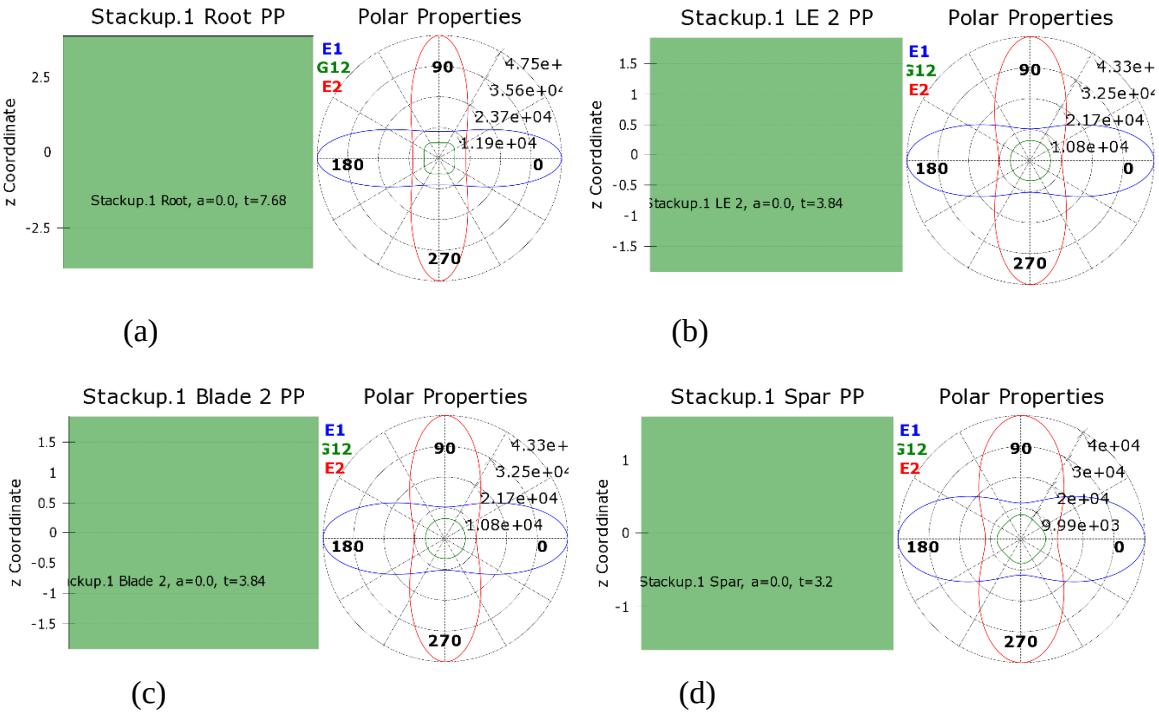

Figure (4.8) Polar Stack-up Properties of (a) Root Section. (b) Leading Edge 2 (c) Trailing Edge 2. (d) Shear Web (Spar)

4.4 FEA Modeling For Static Analysis

The blade geometry is imported into static structural workbench as it is shown in the figure (3.4). the necessary constraints on the blade was applied for a simulation, such as the turbine blade material is chosen from the list of composite materials and selected the one which was entered as composite material property adding as given in the table (3.4). The next procedure, mesh structure of the blade is done by using structured mesh with shell elements. The blade is meshed using the quadrilateral mesh method is utilized to generate elements with low aspect ratios to prevent produced incorrect results, mesh sizing 0.035 m and consisted of 35697 elements and 35575 nodes as shown in the figure (4.9). Then, the wind loads are applied by imported the pressure loads along the blade surface from CFD workbench fluent of pressure load. The hub section of wind turbine blade is applied rotational velocity according to Right Hand Base clockwise 8 rad/s around Z axis component and remote point constraint all six degree of zero. After finalizing of static and dynamic structure definition, the blade analyses by utilizing ANSYS software based on the values of Equivalent Stress, Shear Stress, Total Deformation, Force Reaction and Moment Reaction when blade is undergone to the pressure forces.

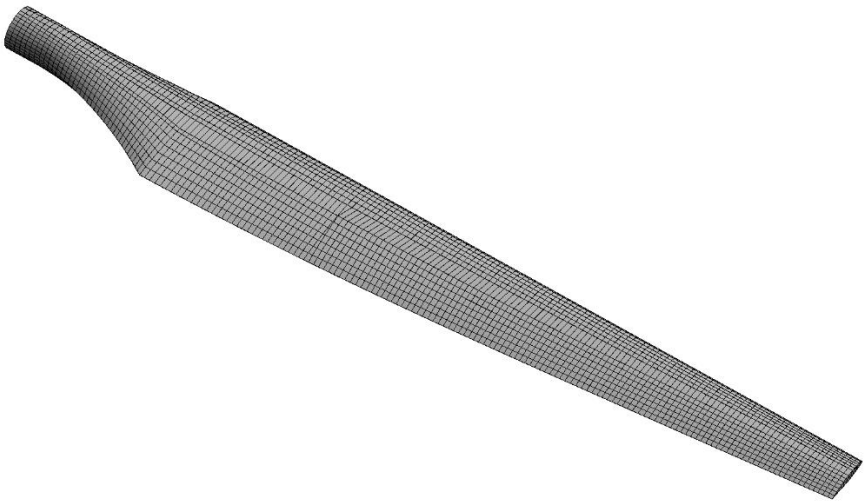

Figure (4.9) Blade Structure Mesh

The ACP model composite of the blade is presented in the figure (4.10). in this figure, a described the reference of fiber direction for the Kevlar 49 epoxy 5505 composite material along the span direction which is shown as green arrow and composite layups direction is shown as pink arrow.

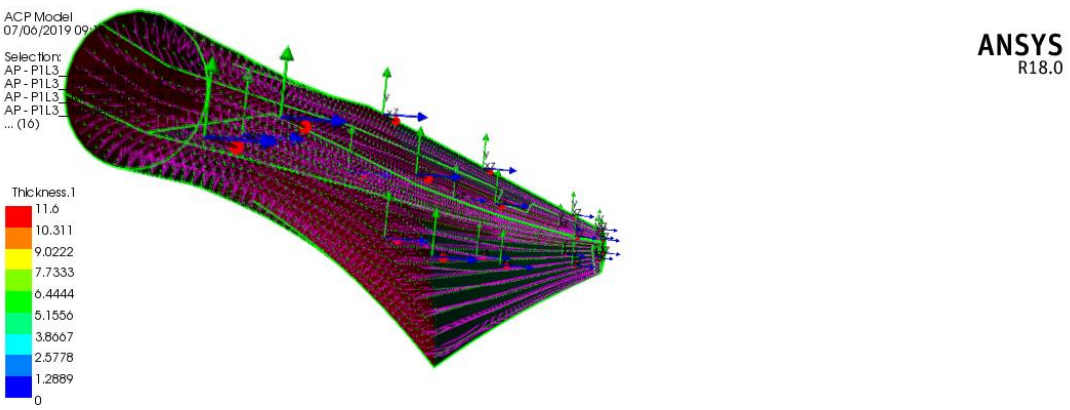

Figure (4.10) ACP Composite Model with Layups and Fiber Direction

4.5 FEA Modeling of Transient Analysis

The transient structural component system was utilized the finite element analysis. Therefore, the blade geometry using in the computational fluid analysis (CFD) participates with the finite element analysis (FEA). Transient conditions were applied for the simulation such as the rotational velocity is applied in the hub section of the blade according to Right Hand Base clockwise 76.4 rpm (8 rad/s) in Z-component constraints all six degrees of zero. The fluid-solid interface region was defined as blade surface. The blade FEA model was applied mesh with shell elements (shell 191) and the mesh discrete into 35697 elements and 35575 nodes as shown in the figure (4.9). The FEA mesh was varied in the CFD mesh and was more proper for the FEA. The loosely coupled modular approach has this advantage to utilizing various meshes for CFD and FEA. The wind turbine blade was modeled as a shell made from Aramid (Kevlar49) reinforced epoxy 5505 composite material. After finalizing of static and dynamic structure definition, the blade analyses by utilizing FEA based on the values of Normal (Direct) Stress, Shear Stress, Total Deformation, Force Reaction and Moment Reaction when blade is undergone to the pressure forces.

4.6 The System Coupling

The system coupling of fluid-structure interaction (FSI) was implemented by two of methods, on one hand the simulation was performed by one-way fluid-structure interaction for all operation of wind speeds. On the other hand, the simulation was executed too for two-way of fluid-structure interaction at cut-out wind speed because of the maximum deformation, equivalent stress and shear stress occurred with this wind speed. Additionally, the two-way FSI simulation needs a computer with high specifications such as wide hard disc space during the computations and a big enough space for results storage.

4.6.1 One-way System Coupling

The system coupling component was utilized to execute coupling between the CFD and FE analysis. The system coupling setup was defined to be the same for the fluent (CFD) transient and FEA modules. Additionally, two files of data transfers were formed for the two-way Fluid-Structural Interaction (FSI) analysis with a fluid-solid interface included of the whole blade surfaces as the region of contribution from the FEA. In the data transfer procedure, the fluid force (pressure force) was transferred from the

CFD model at the blade region to the fluid-solid interface region of FEA. The sequence of data transfer was accountable for transferring the incremental displacement at the fluid-solid interface region in the FEA to the rotor blade region as mesh displacement in the CFD. In the fluent (Pressure load) simulation of the CFD model is solved to provide the initial pressure force on the rotor blade which transferred to the specified fluid-solid interface in the structural model as the initial load on the rotor blade. Then the system coupling is started by the transferred the displacement data which occurred by the initial pressure load in FEA through the specified fluid-solid interface region in the structural model is transferred to the CFD of a transient. The system coupling implements mesh deformation with the selection mesh deformation settings. The process is repeated for the number of defined coupling iterations until the accomplishment of all the coupling steps. Figure (4.11) shows the flowchart of system coupling.

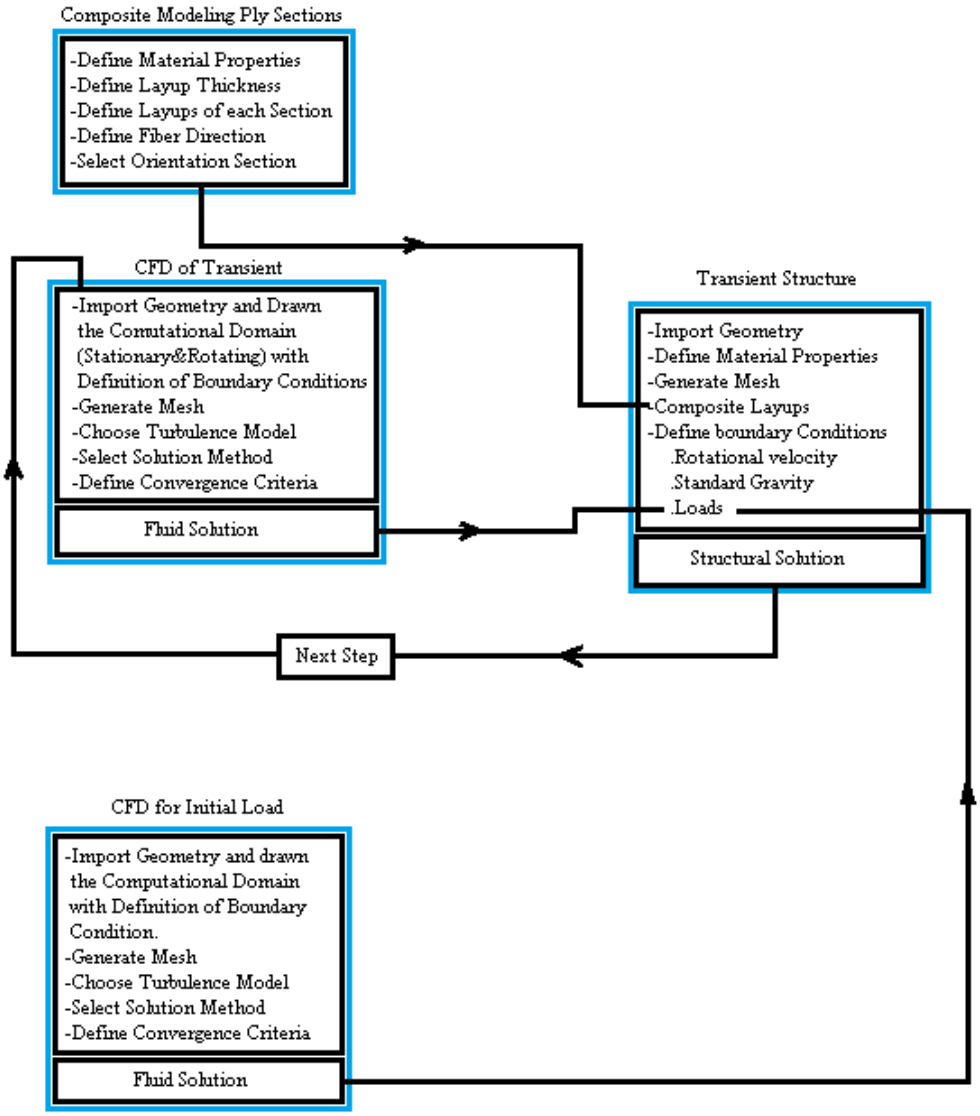

Figure (4.11) One-way System Coupling Flowchart

4.6.2 Two-Way System Coupling

The maximum deformation, normal stress, and shear stress have occurred in cut-out wind speed according to results of one-way Fluid-Structure Interaction, that drives us to execute an extra simulation for Two-way system coupling simulation was performed for obtaining the more accurate results, and compared with the one-way results. The simulation configurations of two-way system coupling consist of the two main steps:

Step one, the time step size, finishing time and the minimum/maximum of coupling iterations number at each step. In general, aside from coupling iterations at each step, the required information automatically transferred to system coupling as soon as the solvers have been coupled.

Step two, data transfer is the most important part of the system coupling, because of incorporation and managing the data transfer sequence between the two numerical solvers which are the Fluent to Mechanical (aerodynamic forces) and Mechanical to Fluent (displacements of nodal)

The mesh parameters help the CFD solver to converge with reducing the iterations and less error, that's can be obtained by keeping the quality of orthogonal ratio higher and skewness lower for whole CFD domain [112]. The mesh applied for CFD of two-way fluid-structure interaction with element size 1318.3 mm, and introduced the distribution of orthogonally and skewness cells described in the figures (4.12) and (4.13) respectively. There are no mesh cells under an orthogonal quality of 0.11261 or over a skewness of 0.88739 for a good optimization of aerodynamic performance in the FSI model. The quality average of orthogonal and skewness were 0.76446 and 0.23431 respectively.

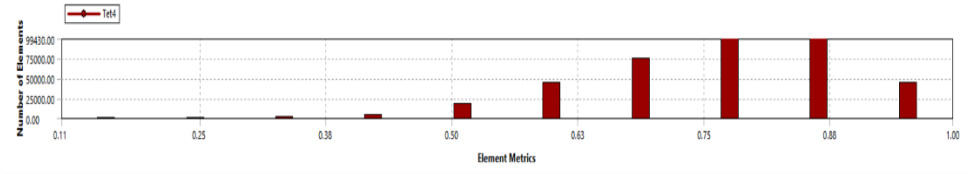

Figure (4.12) Orthogonally Quality Mesh Cell

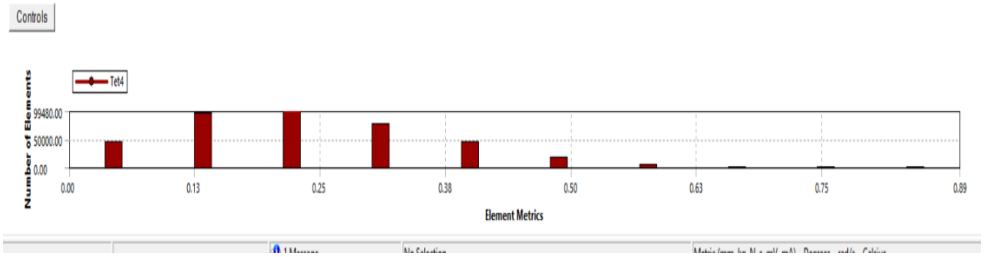

Figure (4.13) Skewness Quality Mesh Cell

Moreover, the techniques used in mesh settings discussed to improve the CFD meshing utilizing the target which is the smallest number of nodes and elements of the mesh without the influence of the end result resolution.

The two-way system coupling runs by transferring displacement data created by the initial pressure load of fluent in the FEA to the CFD of the transient. The process is repeated for the number of defined coupling iterations until the completed all of the coupling steps. The figure (4.14) describes the two-way system coupling flowchart.

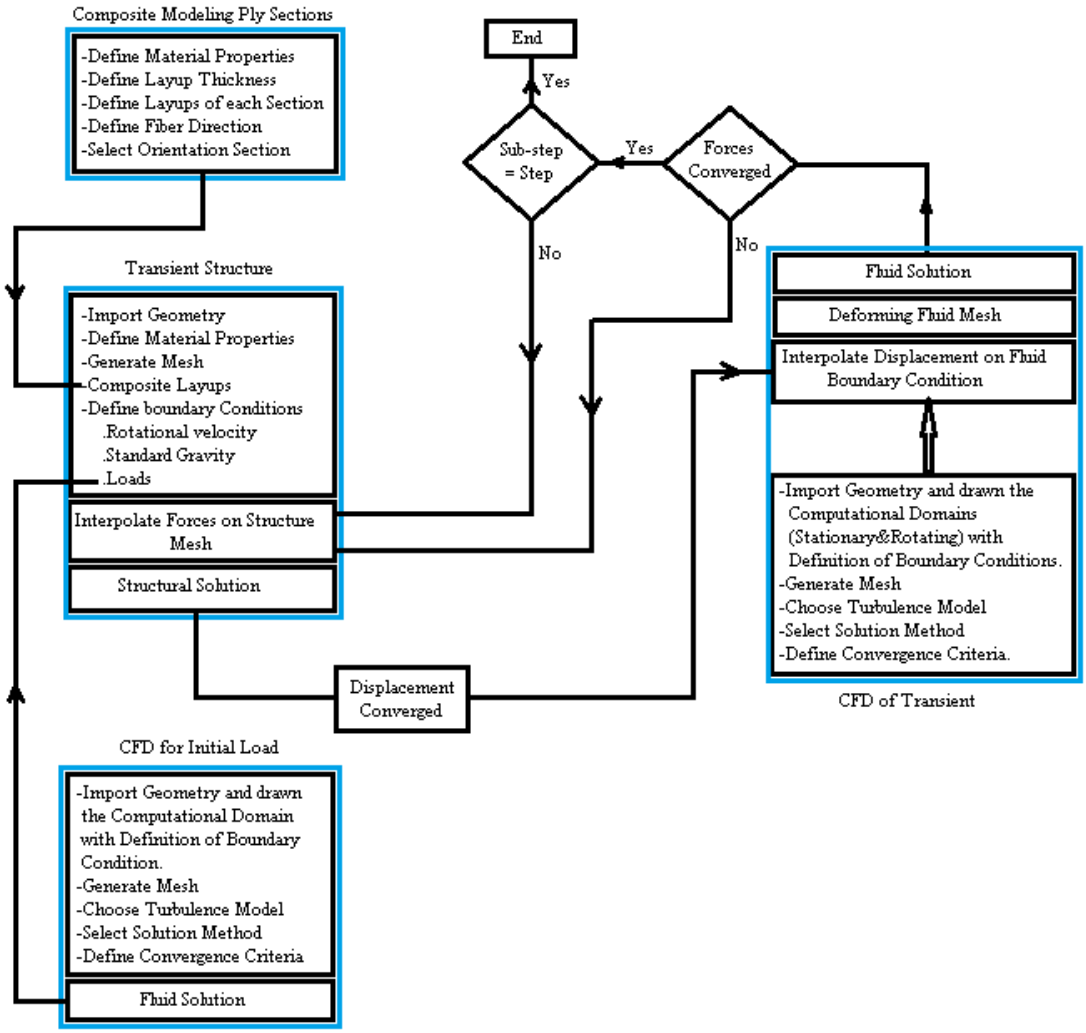

Figure (4.14) Two-way System Coupling Flowchart

CHAPTER FIVE

ANALYSIS OF NUMERICALLY OBTAINED RESULTS AND DISCUSSION

5.1 Fluent Analysis Results

A Computational Fluid Dynamic (CFD) 3-D for both the pressure (aerodynamic) loads simulation and fluent transient simulation are completed at attack angle 5° of the blade model described in the figure (3.4), a fluent domains of one blade in 120º is designed as shown in the figures (4.2) and (4.4). The domain utilizes periodic boundary condition for keeping the simulation equivalent to three blades in a circular domain. The simulation is performed using a model of a steady state SST k-ω turbulence solution. The simulations were performed for different wind speeds starting from cut-in speed up to the cut-out speed. The fluid analysis of the blade is discussed for only the design wind speed as an example for simulations done.

5.1.1 Fluent Analysis Results of Pressure (aerodynamic) Loads

Figure (5.1) illustrates the pressure contour plots for both of the pressure and suction side of the blade, found that the pressure generated on the blade surface was graduated through the blade root to the tip and the maximum pressure is shown on leading edge section of the blade.

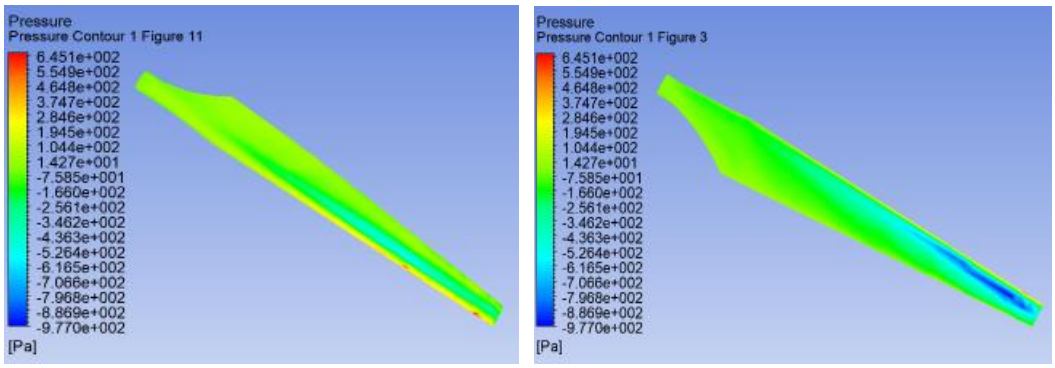

(a) Pressure Side (b) Suction Side

Figure (5.1) Pressure Contours Plots on the Blade

At design wind speed 8 m/s, the pressure distribution at three cross-sections selected which are defined as the blade radius percentage are in good agreement of flow characteristic and the flow is perfectly attached and there is no flow separation. At the cross-section 0.40 R, the pressure distribution is regular with low-pressure distribution while at 0.75 R and 0.95 R of blade radius, the pressure difference can be noted and achievement of the torque generated. The pressure contour of 0.95 R of the blade radius demonstrates low pressure on the suction side of the blade approximately at the middle of the chord length, the velocity vector can be observed the high speed in that area in streamline plot. Figures (5.2) and (5.3) illustrate the streamlines velocity and pressure contours over the airfoils. Figure (5.4) shows the velocity streamlines for the design wind speed 8 m/s.

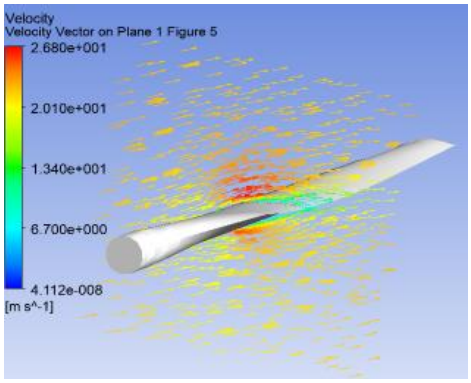

(a) 0.40 R

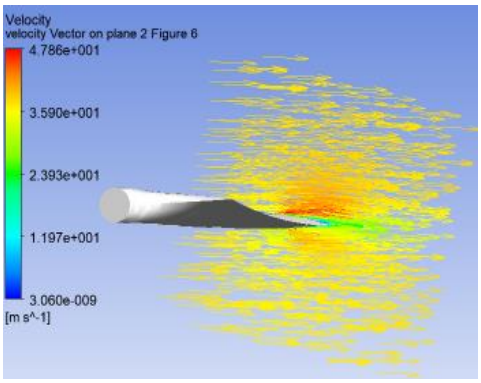

(b) 0.75 R

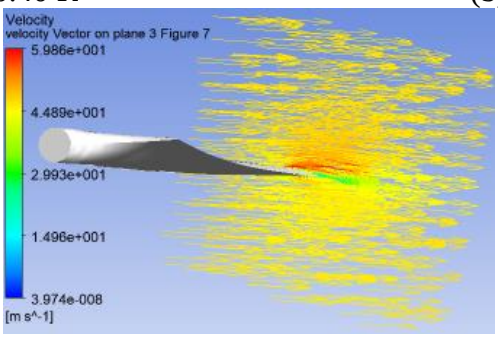

(c) 0.95 R

Figure (5.2) Velocity Vector Distribution for (a) 0.4 R (b) 0.75 R (c) 0.95 R

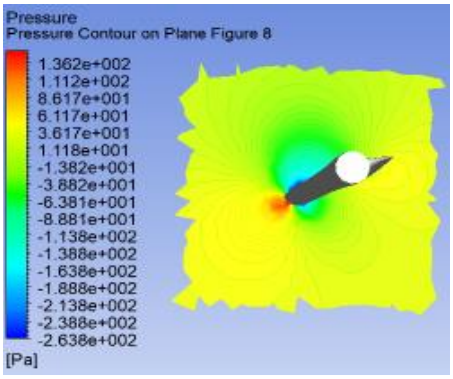

(a) 0.40 R

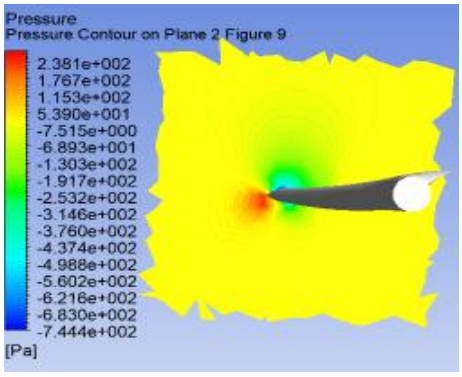

(b) 0.75 R

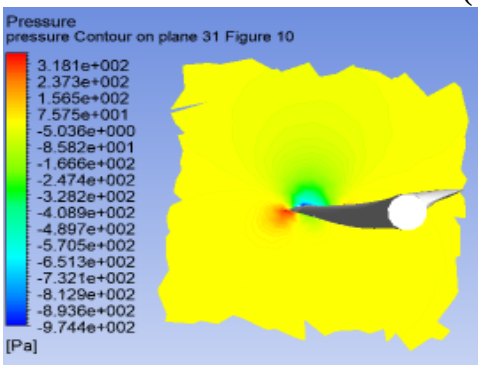

(c) 0.95 R

Figure (5.3) Pressure contours Distribution for (a) 0.4 R (b) 0.75 R (c) 0.95 R

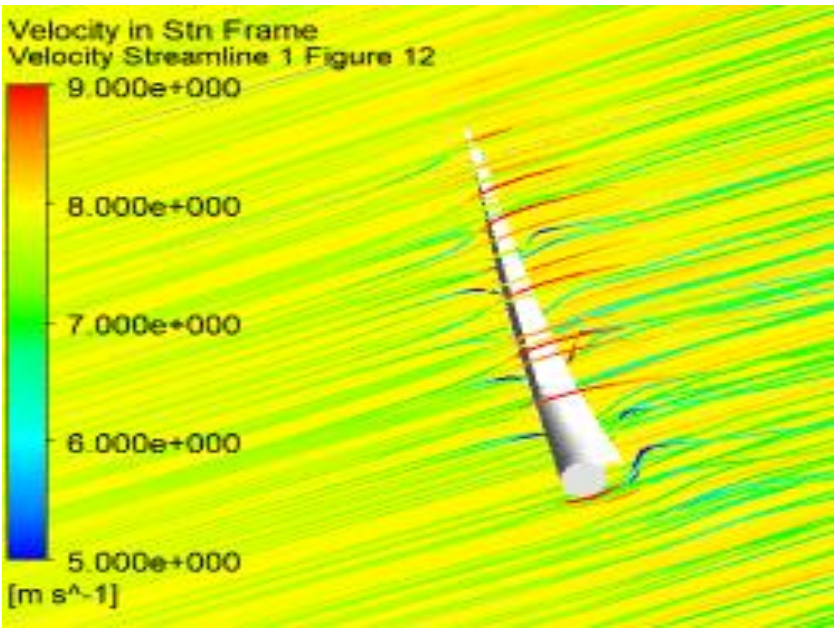

Figure (5.4) Wind Streamlines over the Blade at Design Wind Speed

5.1.2 Transient Fluent Analysis Results

The pressure contour was plotted on the blade for both of the pressure and suction sides through the numerical results of transient fluent at the design speed. The figure (5.5) shows the pressure contour on both sides of the blade. Found the pressure generated on the blade suction side was little changed through the whole of the suction side. While the pressure of pressure side was graduate in the pressure from the blade root to the tip and the maximum pressure is shown on the trailing edge section of the blade on the second half of the blade.

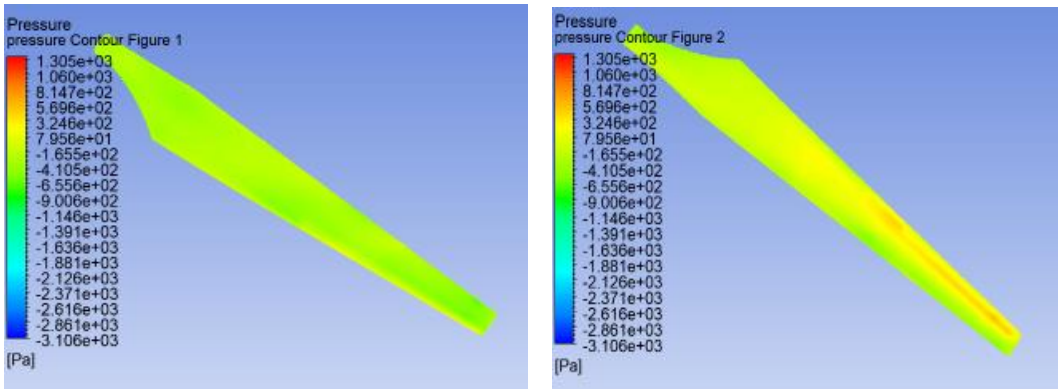

(a) Suction Side (b) Pressure Side

Figure (5.5) Transient Pressure Contours Plots on the blade

The pressure distribution on the blade surface at three cross-sections selected which are positioning the three different airfoils used to design of the blade. The pressure configuration on the blade was satisfied because it has different level pressure on both sides of the blade to generate the torque at the three cross-sections. Moreover, the pressure generated on both sides of the blade through the aerodynamic flow has enough force to rotate the blade for generating torque. The figure (5.6) describes the pressure distribution on the three cross-sections 0.4R, 0.75R and 0.95R of the blade, the results of

rotation domain and turn on the mesh deformed. Figure (5.7) shows the velocity streamlines on the blade at the design wind speed 8 m/s in the rotation domain.

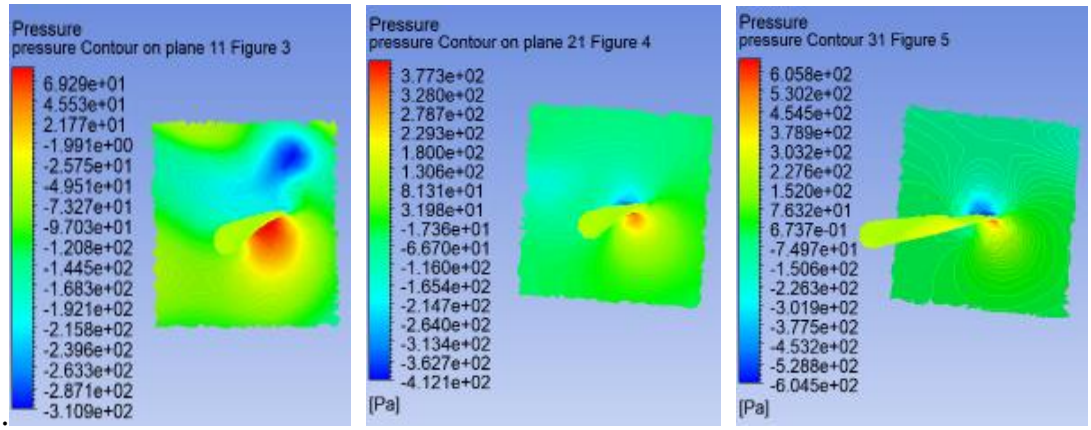

(a) 0.4R (b) 0.75R (c) 0.95R

Figure (5.6) Transient Pressure Distribution on the Three Cross Sections

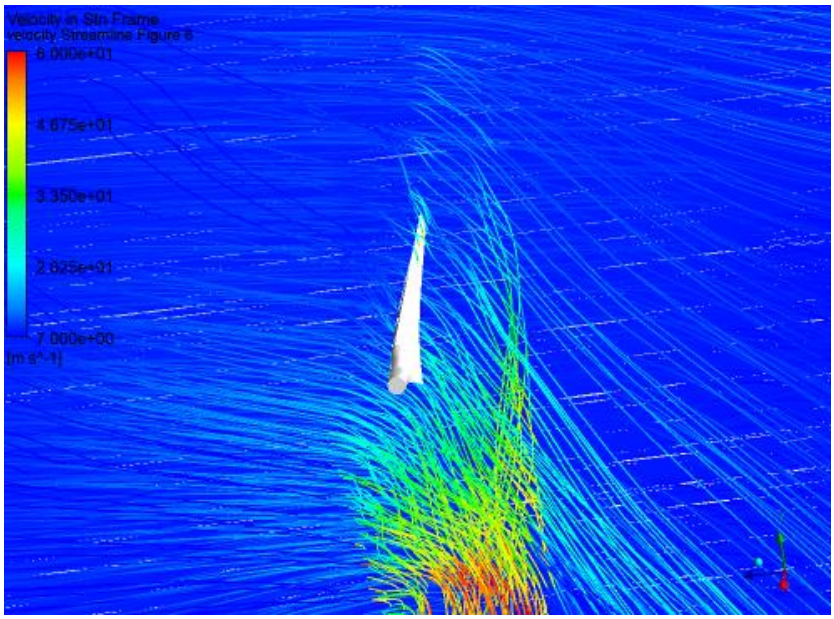

Figure (5.7) Velocity Streamlines of Transient at the Design Wind Speed.

5.2 Composite Material Selection

The Active Pitch Control mechanism is supposed to be for the horizontal axis wind turbine where the rotor blades move around their along axis (to pitch) by a computer-controlled mechanism. For extreme wind speed, wind turbine blades are pitched to a place that the airflow moves around the blades surface smoothly to reduce aerodynamic load and turned off the blades to prevent blade rotation above cut-out speed. Due to mention above, the maximum aerodynamic load on the blades occur in cut-out speed, so the composite material selection was executed through this consideration. according to the FEA results of the static structural simulation, the normal stress through the wind speeds operating is a maximum value happens at the cut-out speed for the five different composite materials using for the simulations, while the normal stresses of the composite materials were a very low compared to composite materials

yield strength, table (5.1) describes the tip deformations, maximum normal stresses, and maximum shear stresses for cut-out wind speed 25m/s. These composite materials E-glass/Epoxy5505, Glass/Epoxy and S2-glass/Epoxy5505 have the maximum tip deformation in the static structural analysis at 49.572 mm, 49.403 and 42.500 mm respectively compared with the other composite materials.

Table (5.1) Results analysis of static structure

	E-glass Epoxy 5505	T300 Carbon Epoxy 5505	Kevlar 49 Epoxy 5505	Glass Epoxy	S2-glass Epoxy 5505
Total Deformation (mm)	49.572	19.59	38.889	49.403	42.500
Normal Stress (MPa)	14.254 -15.11	17.202 -20.561	16.116 -19,452	14.77 -16.706	13.783 -15.073
Shear Stress (MPa)	7.9959 -3.6616	17.19 -10.068	15.348 -8.4285	12.800 -5.892	8.822 -3.982

In reality, the consideration of aero-elasticity is important for all applications involve a structural response to a fluid action. For that, the simulation results of a wind turbine structural response are required applying the fluid-structural interaction simulation to get accurate results.

The one-way fluid-structure interaction is used to compare between the five composite materials which ones is more suitable for this wind turbine case. The fluid-structure interaction has performed for the different composite materials at the cut-out speed which is the maximum aerodynamic load influence on the blades. The transient structure analysis results for the five composite materials are described in the table (5.2) for the parameters of normal (direct) stress, shear stress, and deformation, these results are plotted in the figures (5.8), (5.9), and (5.10) for the normal stress and shear stress, deformation, and blade weight, respectively.

Table (5.2) Results analysis of Transient structural

	E-glass Epoxy 5505	T300 Carbon Epoxy 5505	Kevlar 49 Epoxy 5505	Glass Epoxy	S2-glass Epoxy 5505
Total Deformation (mm)	155.22	62.299	128.71	155.90	137.40
Max. Normal Stress (MPa)	40.135 -47.454	46.129 -63.343	44.580 -65.185	40.927 -55.317	39.316 -47.751
Shear Stress (MPa)	23.449 -10.453	48.924 -30.793	46.681 -26.470	37.996 -18.135	26.040 -11.944
Blade Weight (kg)	71.967	57.608	51.009	71.024	70.270

The selection of composite material is based on the results of FSI simulation for each composite material and compared these results with each other's. The simulation results for the five composite materials are presented the maximum normal stress of kevlar49/Epoxy 5505 is a higher value than other of composite materials as it is shown in the figure (5.8), and the second higher value is T300 carbon/Epoxy 5505. While, these value are compared to the ultimate strength of each composite material. The kevlar49/Epoxy 5505 is a more reasonable maximum normal stress compared with its the

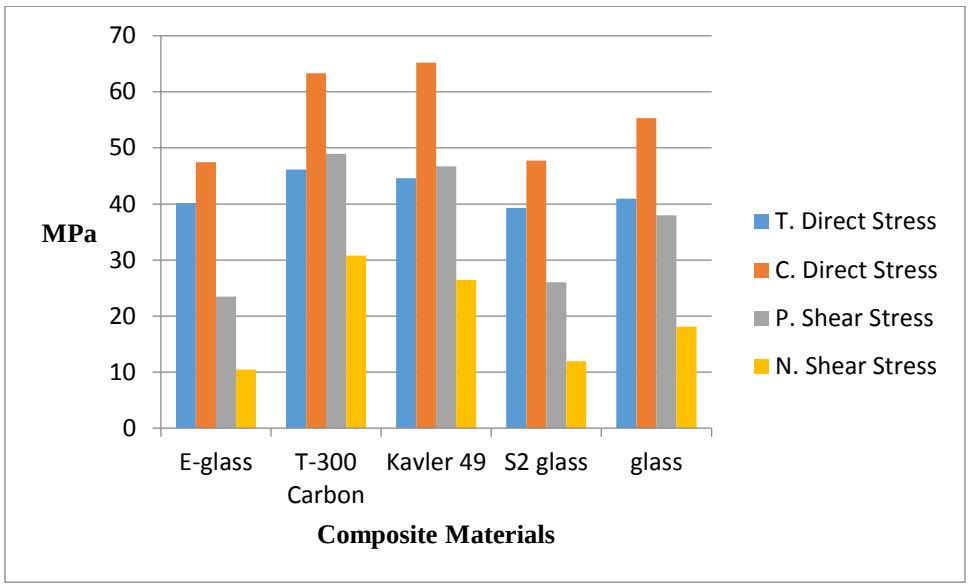

Figure (5.8) Maximum the Direct and Shear Stress for Five Composite Materials

ultimate strength which is 729.758 MPa, unlike the T300 carbon/Epoxy 5505 is far from it's the ultimate strength. Moreover, the blade fabricates by the kevlar49/Epoxy 5505 has a lowest weight among the five composite materials as described in the figure (5.9). The blade deformation of composite material T300 carbon/Epoxy has a lowest value among the five composite materials, and the kevlar49/Epoxy has the second minimum value of the deformation as demonstrated in figure (5.10). The deformation of the five composite materials is a less than the maximum allowable value 10% of blade length. Based on the information mentioned above, the kevlar49/Epoxy 5505 is the proper composite material among the five composite materials in this study case.

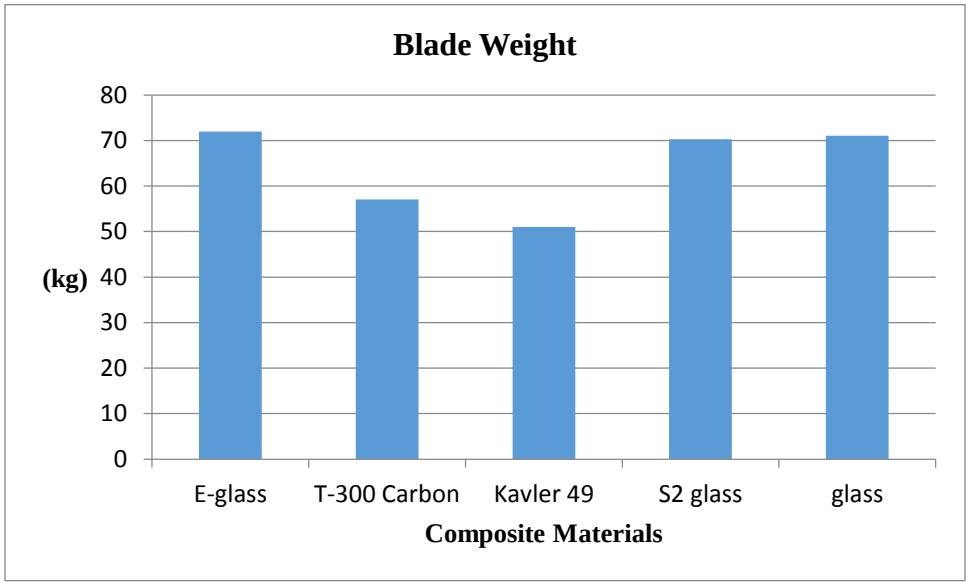

Figure (5.9) Blade Weight for Different Composite Materials

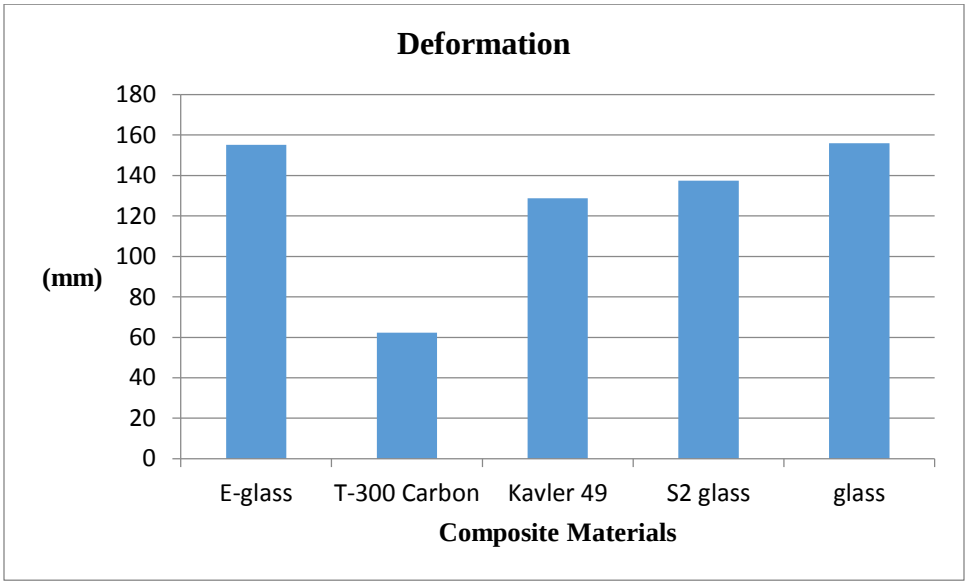

Figure (5.10) Blade Deformation for Different Composite Materials

5.3 Static Structural analysis Results

In order to execute the static structural analysis, a finite element code of ANSYS software was used for a number of different wind speeds among the cut-in speed to cut-out speed including the design speed which is 8 m/s. In this analysis, linear static stress analysis, Shear stress analysis, force reaction analysis, moment reaction analysis, and blade deflection analysis were achieved. The aerodynamic fluent loads were applied along the blade length direction. Loads were computed by the Computational Fluid Dynamic (CFD) for the different wind speeds at rotational speed design to be 76.4 rpm (8 rad/s). According to the analysis results, it was assured that the blade works a safety with the composite material used.

5.3.1 Normal (Direct) Stress Analysis

The static structural simulation was performed through the operation of wind speeds among cut-in speed to cut-out speed including design speed, the normal stress results on the blade were found that is a little higher in cut-in speed compared with the next three of the operational wind speeds. The normal stress results are shown in the table (5.3). For all operations of wind speeds showed that the maximum normal stress occurs on opposite sides of the root connection with the hub, while the maximum normal stress has increased with wind speed increasing and occurred in the same places. However, the maximum normal stress was registered at the cut-out speed 16.116 MPa, 19.452 MPa for Positive and Negative maximum normal stress, respectively. Through the figure (5.11) to figure (5.16) is explained the normal stress results mapped on the blade geometry and located the position of maximum normal stress on the blade for each wind speed operation.

Table (5.3) Maximum Normal Stress Results for Different Operating Speeds

Wind Operation Speed	4 m/s	8 m/s	12 m/s	16 m/s	20 m/s	25 m/s
Max. Normal Stress (MPa)	3.5325 -2.7200	4.5773 -4.8666	6.4304 -7.5699	9.2184 -10.993	12.063 -14.445	16.116 -19.452

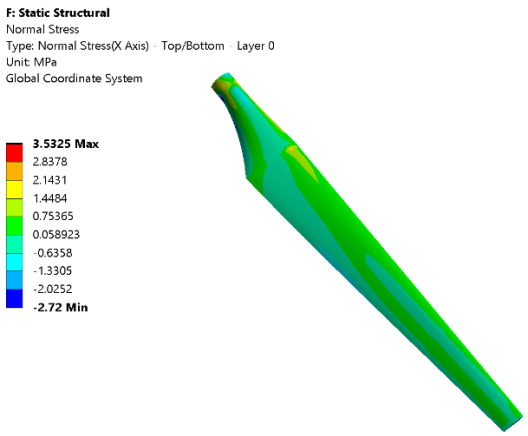

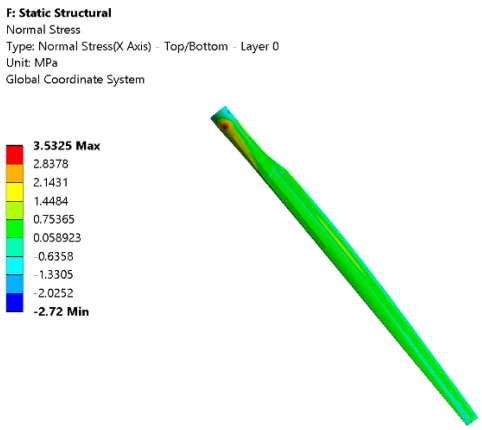

(a) Suction Side (b) Pressure Side

Figure (5.11) Normal Stress Distribution on the Blade for Design Speed 4 m/s

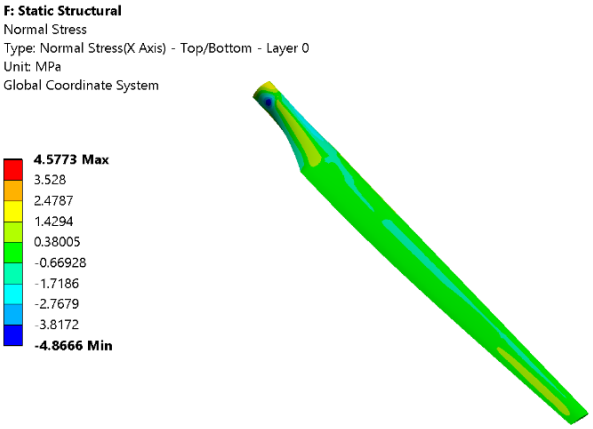

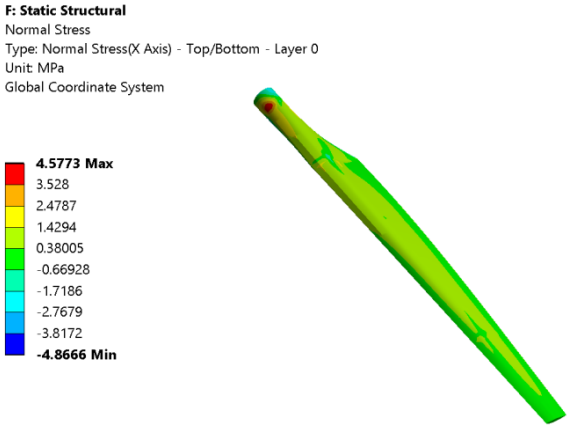

(b) Suction Side (b) Pressure Side

Figure (5.12) Normal Stress Distribution on the Blade for Cut-in Speed 8 m/s

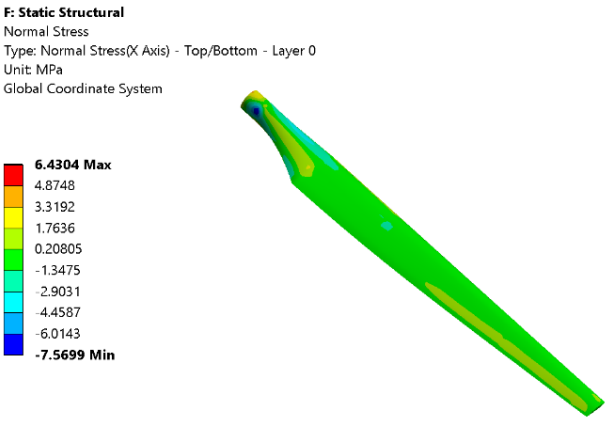

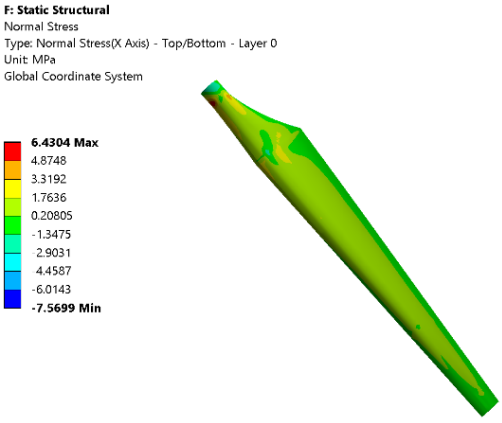

(a) Suction Side (b) Pressure Side

Figure (5.13) Normal Stress Distribution on the Blade for Wind Speed 12 m/s

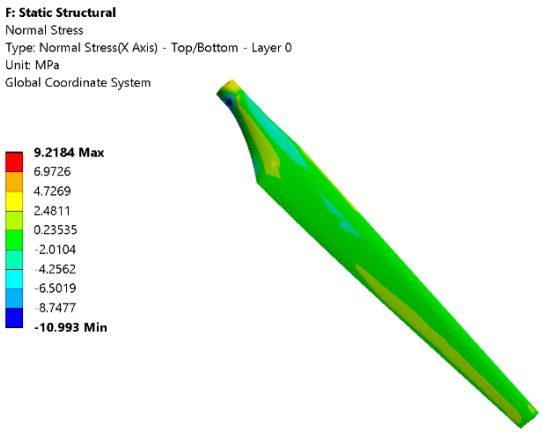

(a) Suction Side

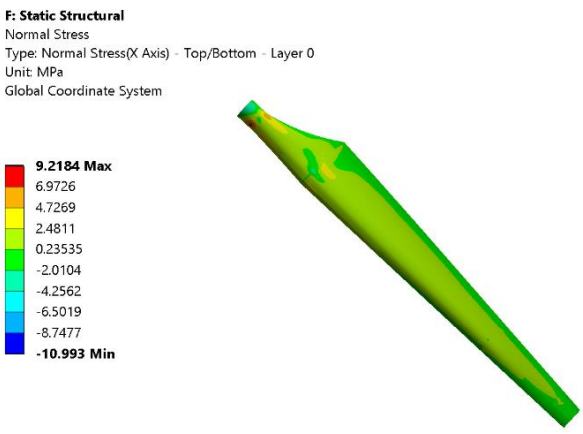

(b) Pressure Side

Figure (5.14) Normal Stress Distribution on the Blade for Wind Speed 16 m/s

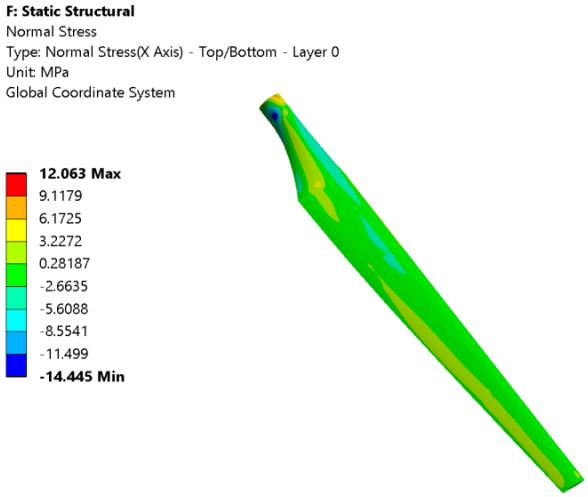

(a) Suction Side

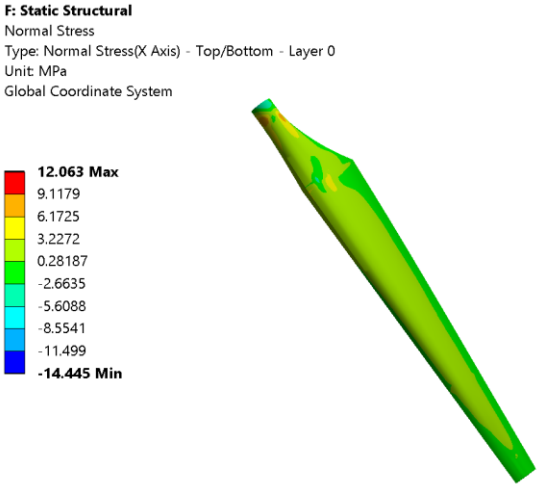

(b) Pressure Side

Figure (5.15) Normal Stress Distribution on the Blade for Wind Speed 20 m/s

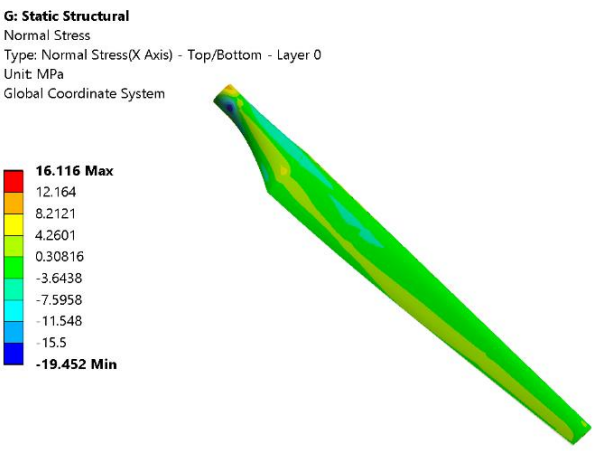

(a) Suction Side

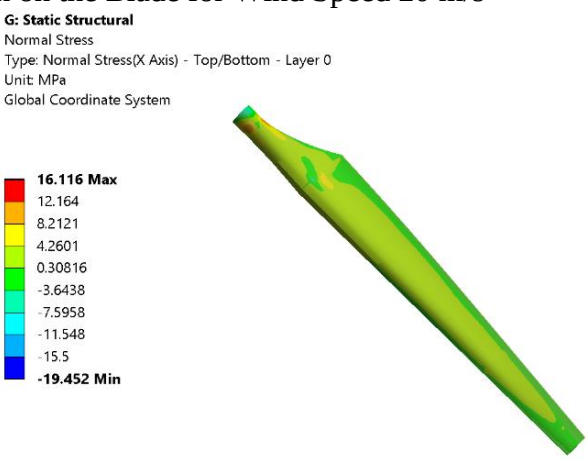

(b) Pressure Side

Figure (5.16) Normal Stress Distribution on the Blade for Cut-out Speed 25 m/s

The normal stress results of different wind speeds applied on the blade were represented to predict the normal stress characteristic of the blade through wind operation speeds. The charts were plotted of these results and shown the trend line slightly grows with wind speed change, the maximum normal stress value starts at 3.5325 (MPa) for the cut-in wind speed 4 m/s and grows to reach the maximum value 16.116 (MPa) at cut-out wind speed 25 m/s. While the negative maximum normal stress starts at 2.72 MPa of the cut-in wind speed to reach the maximum value of 19.452 MPa for cut-out speed. The figure (5.17) demonstrates the maximum normal stress trend line for wind operation speeds.

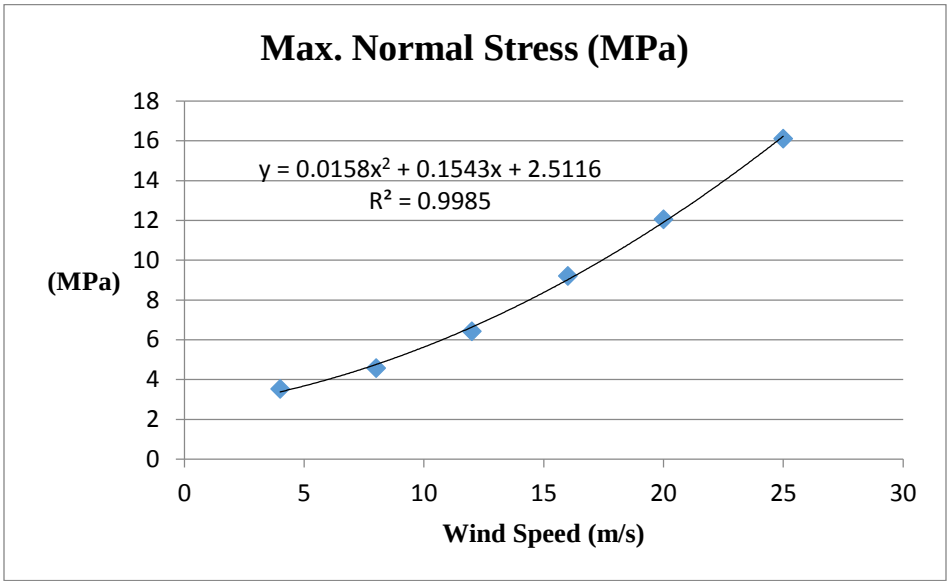

Figure (5.17) Maximum Normal Stress of the Operational Wind Speeds

5.3.2 Shear Stress Analysis

Shear stress analysis was executed for both sides of the pressure and suction side of the blade because the blade affected by positive and negative pressure for the pressure side and suction side respectively. Shear stress was carried out for wind speeds regime and the results are shown in the table (5.4). Simulation results were obtained for the shear stress are shown their distribution on the blade surface and indicated the maximum shear stress on the hub section of the blade where connects blade fixing part with the hub rotor system, shear stress value increases by raise wind speed. Through the figures (5.18) to (5.23) are illustrated the shear stress results mapped on the blade geometry and positioned the maximum/minimum shear stress on the blade for each operation of wind speeds.

Table (5.4) Maximum Shear Stress Results for Different Operating Speeds.

Wind Operation Speed	4 m/s	8 m/s	12 m/s	16 m/s	20 m/s	25 m/s
Max. Positive Shear Stress (MPa)	2.4331	4.3424	6.5489	9.1034	11.654	15.348
Max. Negative Shear Stress(MPa)	-1.8907	-2.2505	-3.284	-4.6633	-6.1888	-8.4285

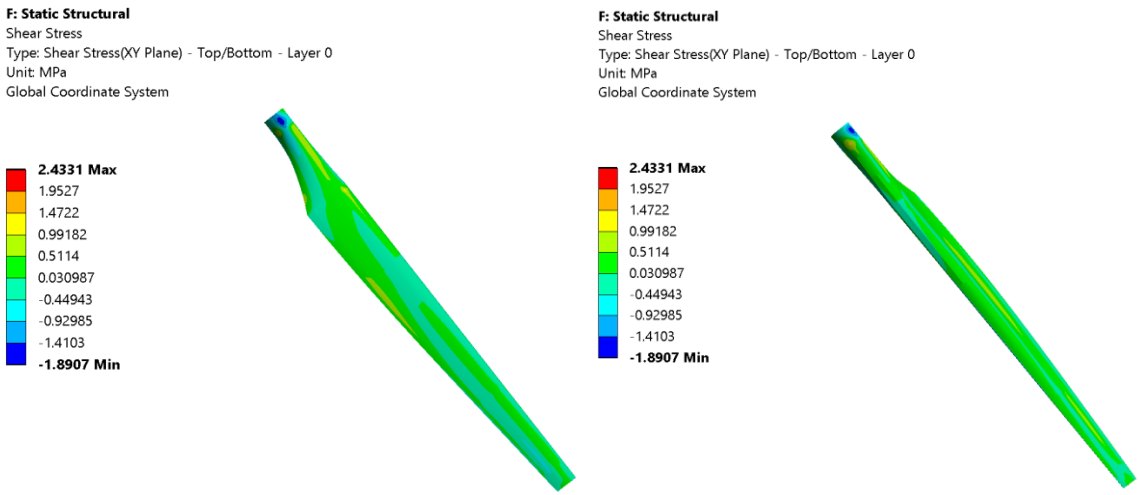

(a) Suction Side (b) Pressure Side

Figure (5.18) Shear Stress Distribution on the Blade for Cut-in Speed 4 m/s

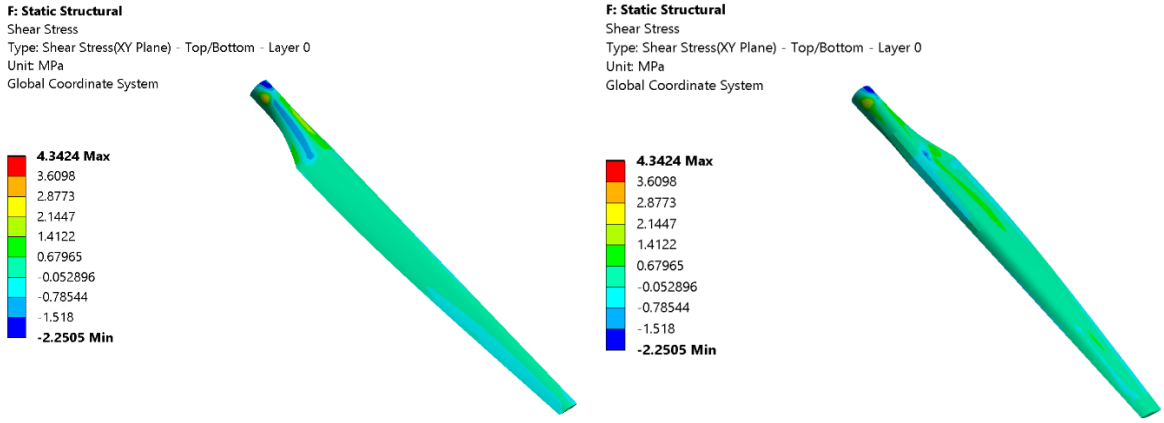

(a) Suction Side (b) Pressure Side

Figure (5.19) Shear Stress Distribution on the Blade for Design Speed 8 m/s

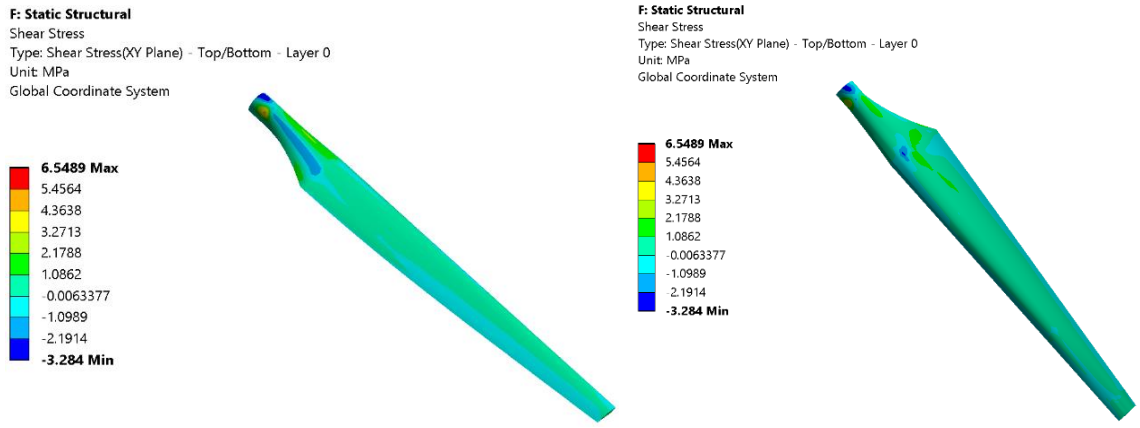

(a) Suction Side (b) Pressure Side

Figure (5.20) Shear Stress Distribution on the Blade for Wind Speed 12 m/s

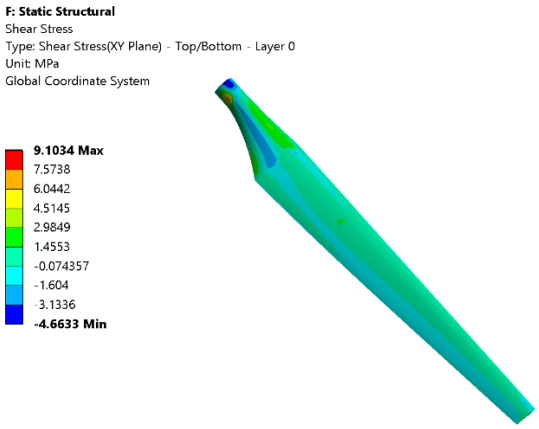

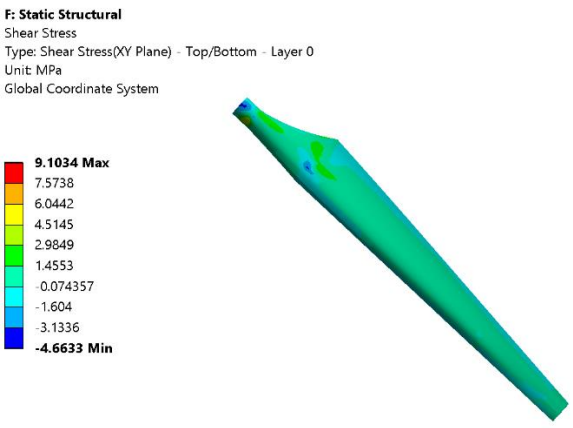

(a) Suction Side (b) Pressure Side

Figure (5.21) Shear Stress Distribution on the Blade for Wind Speed 16 m/s

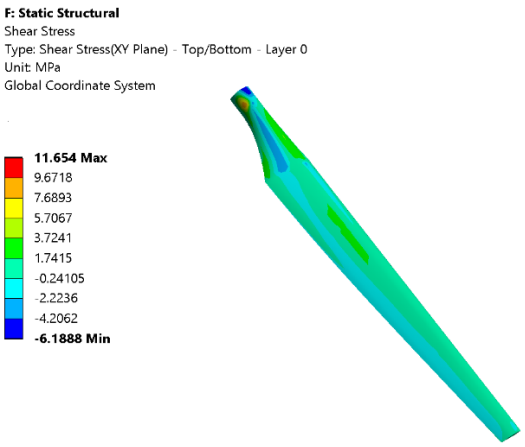

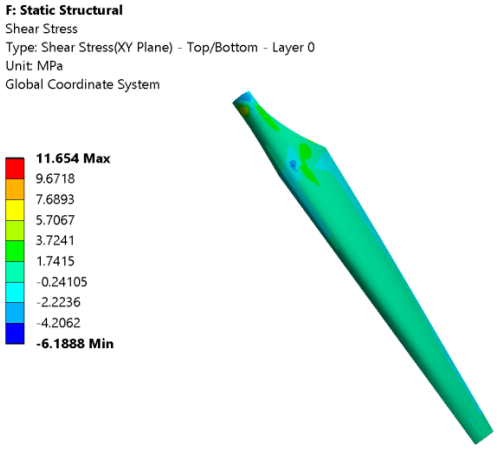

(a) Suction Side (b) Pressure Side

Figure (5.22) Shear Stress Distribution on the Blade for Wind Speed 20 m/s

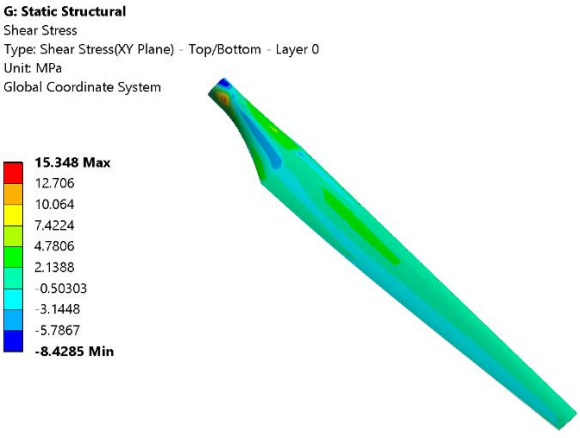

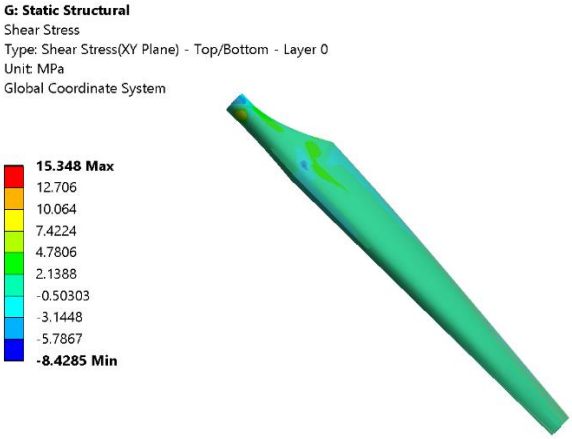

(a) Suction Side (b) Pressure Side

Figure (5.23) Shear Stress Distribution on the Blade for Cut-out Speed 25 m/s.

The shear stress parameter for various operation wind speeds applied on the blade was performed to predict the shear stress characteristic of the blade through the different operational wind speeds. The charts were plotted for those results of maximum positive and negative shear stress. the positive maximum shear stress trend line is sharply grown through the operation of wind speeds to reach the maximum positive value 15.348 (MPa) at cut-out speed 25 m/s, while the negative shear stress trend line is sharply dropped through the operation of wind speeds to reach the value -8.4285 (MPa) at cut-out wind speed. Figure (5.24) and (5.25) show the positive and negative of maximum shear stress trend for the wind operation speeds respectively.

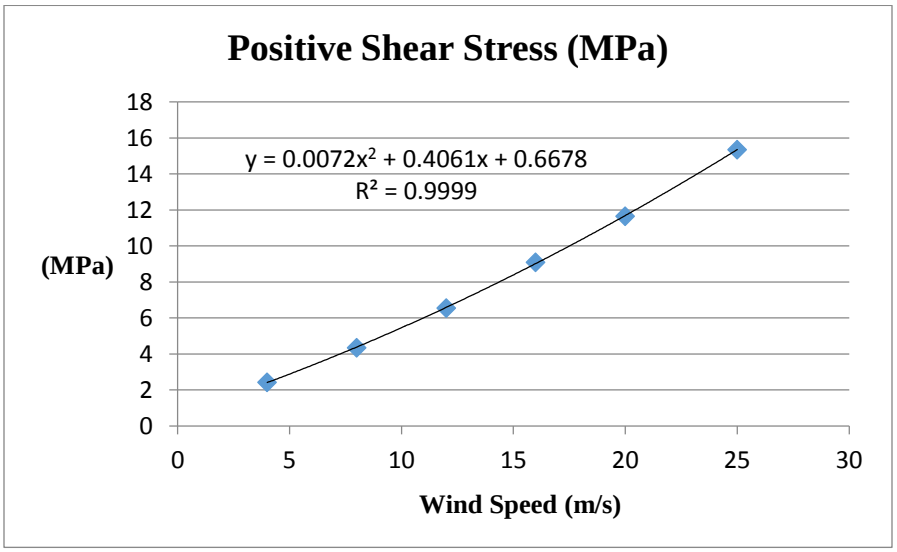

Figure (5.24) Positive Maximum Shear Stress of the Operational Wind Speeds

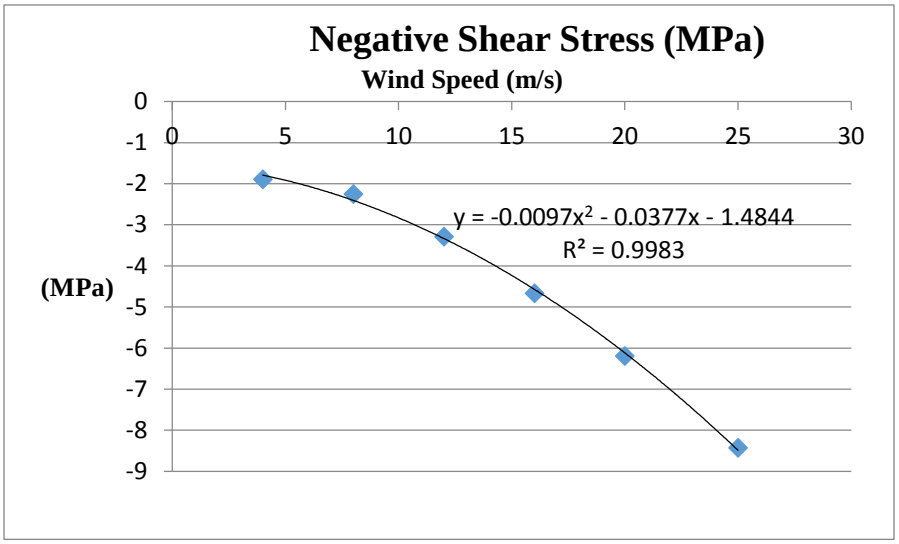

Figure (5.25) Negative Maximum Shear Stress of the Operational Wind Speeds

5.3.3 Force Reaction Analysis

Force reaction analysis of various wind speeds operation was performed to predict how much changes of force reaction magnitude during the wind speeds operation regime of the system. According to the results, the force reaction trend line a slightly increased within the first three wind speeds operation, while the trend for the next speeds has sharply increased to reach the maximum value 8690.0 (N) at cut-out wind speed 25 m/s. the results of force reaction are described in the table (5.5) for the

different wind speed operation. Figure (5.26) shows the direction of the force reaction to reference the system coordinates axis for design wind speed 8 m/s an example for that, and figure (5.27) shows the forces reaction trend line of the various wind speeds operation regime.

Table (5.5) Resultant Force Reaction for Different Operating Wind Speeds.

Wind Operation Speeds	4 m/s	8 m/s	12 m/s	16 m/s	20 m/s	25 m/s
Total Force Reaction (N)	8361.1	8364.2	8392.3	8448.9	8529.9	8690.0

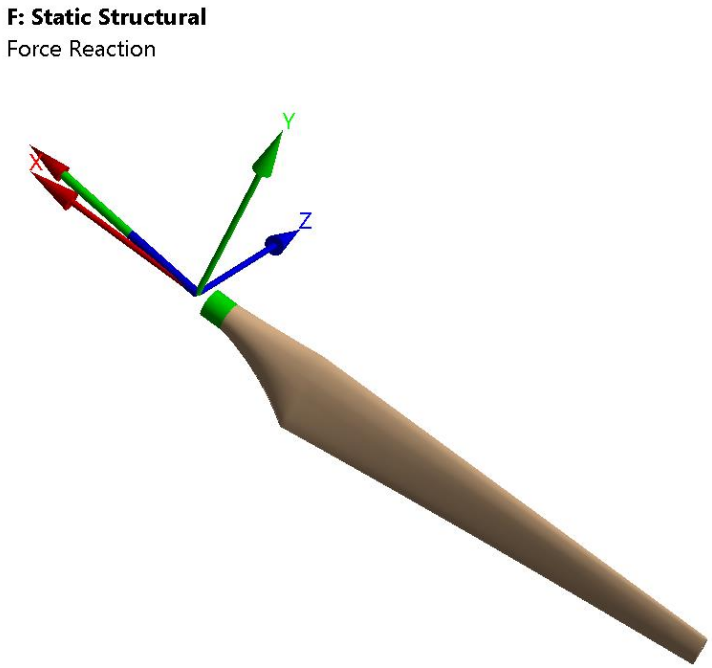

Figure (5.26) Force Reaction of design Wind Speed 8 m/s.

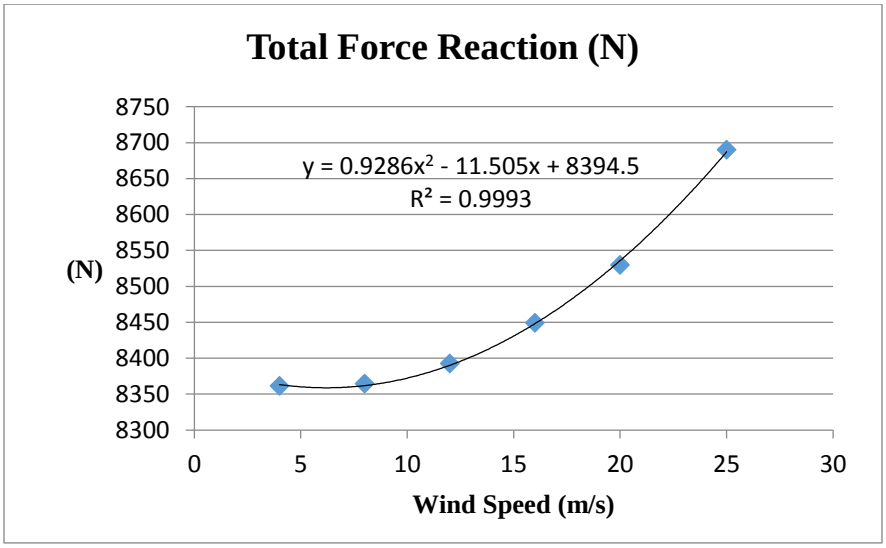

Figure (5.27) Force Reaction Trend for the operational Wind Speeds.

5.3.4 Moment Reaction Analysis

Moment reaction analysis was performed to predict the magnitude of force reaction during the wind speed operation regime of the system. Figure (5.28) shows the direction of moment reaction to reference the system coordinates axis for design wind speed. the results of the moment reaction were described in the table (5.6) for the different wind speeds operation, and that results were represented on figure (5.29) where the moment reaction trend line sharply grows through the operational wind speeds to reach the maximum value moment reaction 8778.6 (N-m) at the cut-out wind speed 25 m/s.

Table (5.6) Moment Reaction Results for Different Operating Wind Speeds.

Wind Operation Speed	4 m/s	8 m/s	12 m/s	16 m/s	20 m/s	25 m/s
Moment Reaction (N-m)	1551.1	2410	3605.5	5052.1	6552.5	8778.6

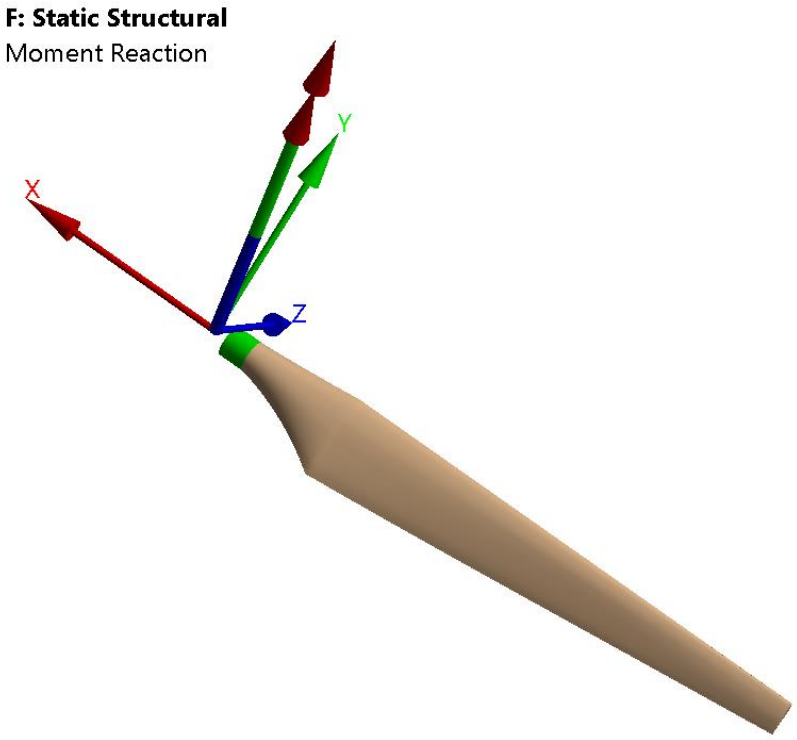

Figure (5.28) Moment Reaction of design Wind Speed 8 m/s.

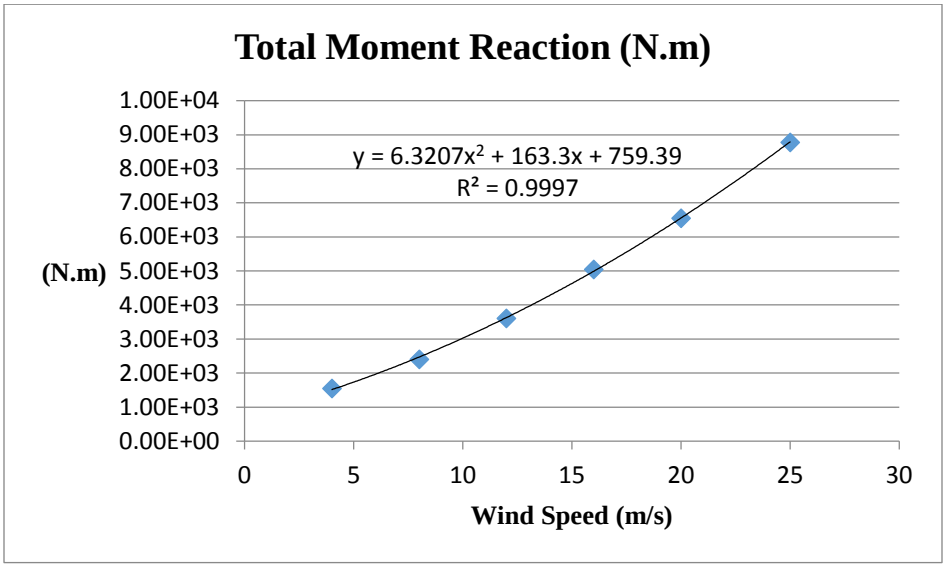

Figure (5.29) Moments Reaction Trend for Operational Wind Speeds

5.3.5 Blade Deformation Analysis

The blade deformation analysis was performed for static structural analysis including the influence of the blade weight, executed for different wind speeds operation and the results have been computed and described in the table (5.7). The simulation results are plotted in the figure (5.30), and the trend line of those results is a sharply raised during the operation of wind speeds, and the maximum of the blade tip deformation is reached to 38.889 mm at cut-out speed. Relationship of blade tip deformation with operational wind speeds describes as linear. Figure (5.31) demonstrates the blade tip deformation for the wind design speed 8 m/s.

Table (5.7) Deflection of Tip Blade for different Operating Wind Speeds.

Wind Operation Speeds	4 m/s	8 m/s	12 m/s	16 m/s	20 m/s	25 m/s
Tip Blade Deformation (mm)	2.723	10.470	16.246	22.551	28.966	38.889

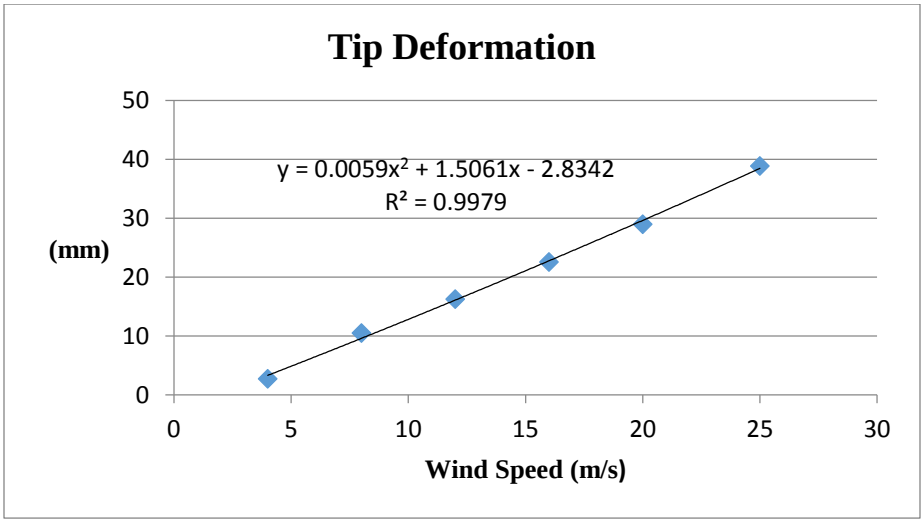

Figure (5.30) Tip blade deformation through the different operating wind speeds.

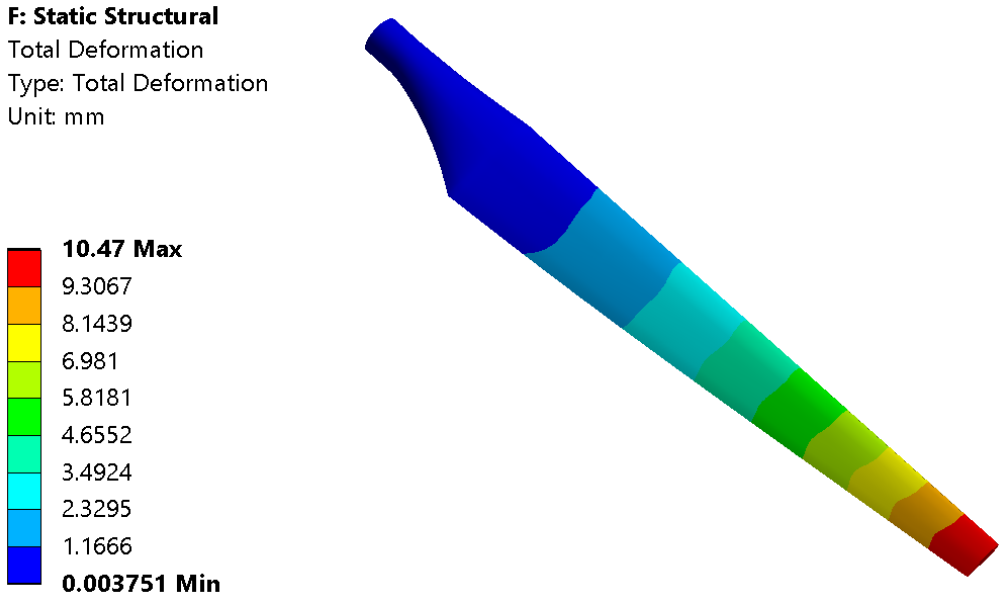

Figure (5.31) Deformation through the Blade Length at the Design Wind Speed

5.4 Transient Structural Analysis Results

A coupled Fluid-Structure Analysis (FSI) model can be efficiently solving for the fluid field and structural field at the same time and providing a high accuracy solution in both of the fluid and structural domains. For a prediction of the real structural characteristic of wind turbine blade during the wind speeds operation, the Fluid-Structure Interaction (FSI) was performed of horizontal axis wind turbine (HAWT) which made through the coupling of the CFD solver with Structural solver in ANSYS Workbench of one-way for various wind speeds operation among the cut-in and cut-out speed including the design wind speed 8 m/s for complete 1 step contains 25 sub-steps. While two-way of system coupling performed for cut-out speed to compare this results with one-way at the specific wind speed. The simulation has been carried out with transient analysis for the complete 1 step contains 1000 sub-step. In this analysis, linear transient normal stress analysis, shear stress analysis, force reaction, moment reaction analysis and the blade deformation analysis were done. The aerodynamic pressure loads were affected on the blade which uses to compute the transient structural analysis for each wind speed applied at blade rotational speed design 76.4 rpm (8 rad/s), and boundary condition was considered to be the blade root is fixed.

5.4.1 Normal (Direct) Stress Analysis

The transient structural simulation was done for six wind speeds starting from cut-in speed 4 m/s with increment 4 m/s for fifth speeds and the cut-out speed was selected to be 25 m/s. The normal stress results on the blade were computed and the results of maximum normal stress over the complete step are shown in the table (5.8) for the six wind speeds among the cut-in speed to cut-out speed. The normal stress has fluctuated over the complete step for each wind speed operation, and the maximum normal stress has happened in sub-step number 2 among wind speeds 12, 16, 20 and 25 m/s. while for wind speeds 4m/s and 8 m/s at sub-step number 8 and 6, respectively. The maximum normal stress were found in the connection of hub with root in the side of positive pressure for all wind speeds, the value of maximum normal stress during the operational wind speeds is 44.580 MPa and -65.185 MPa at sub-step number 2 because the maximum normal stress occurs at cut-out speed. Through the figures

(5.32) to (5.37) describe of the transient maximum normal stress results mapped on the blade geometry over the complete and it´s located on the blade for each operation of wind speeds.

Table (5.8) Maximum Normal Stress Results for Different Wind Speeds

Wind Operation Speed	4 m/s	8 m/s	12 m/s	16 m/s	20 m/s	25 m/s
Max. Normal Stress (MPa)	7.6726 -9.4261	12.748 -16.541	17.699 -23.389	25.304 -34.459	33.330 -46.833	44.580 -65.185

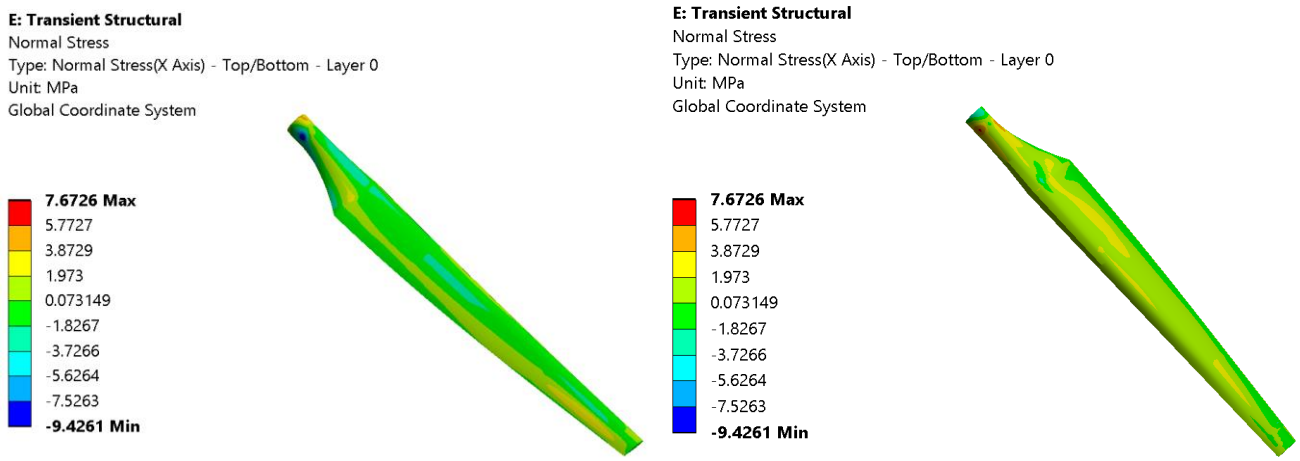

(a) Suction Side (b) Pressure Side

Figure (5.32) Distribution of Maximum Normal Stress at Cut-in Speed 4 m/s

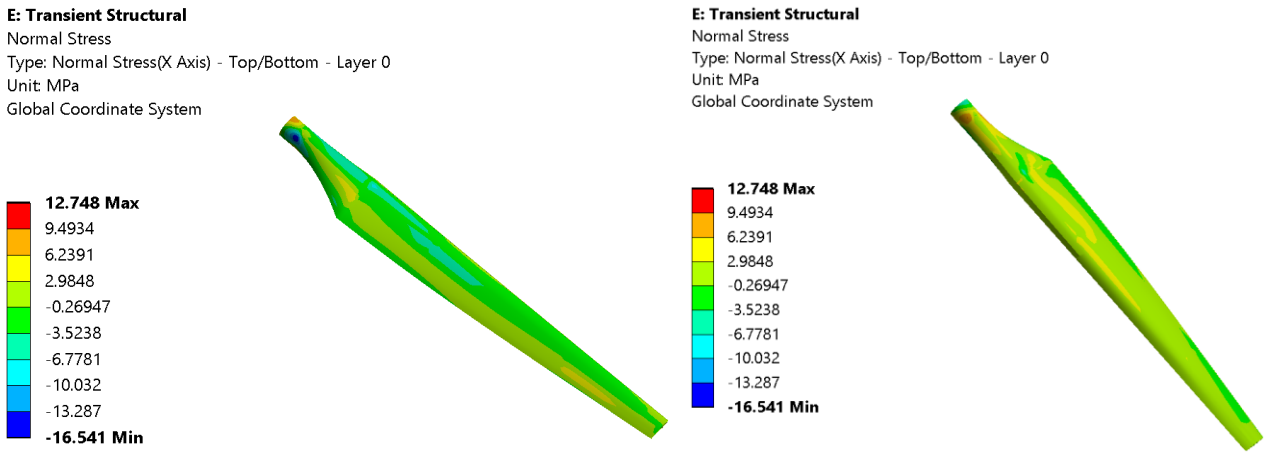

(a) Suction Side (b) Pressure Side

Figure (5.33) Distribution of Maximum Normal Stress at Design Speed 8 m/s

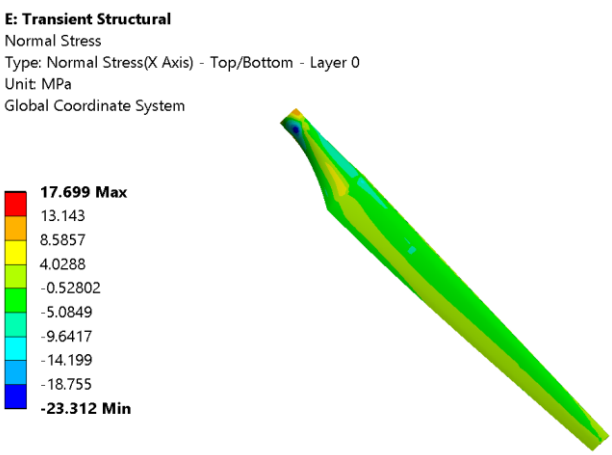

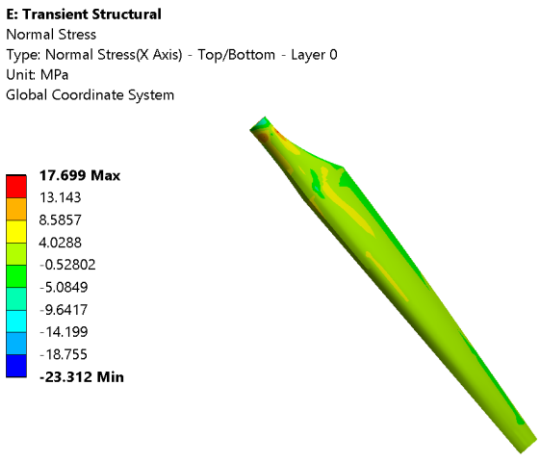

(a) Suction Side (b) Pressure Side

Figure (5.34) Distribution of Maximum Normal Stress at Wind Speed 12 m/s

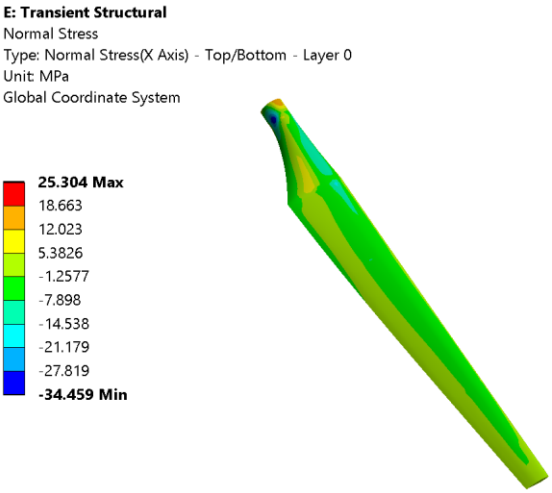

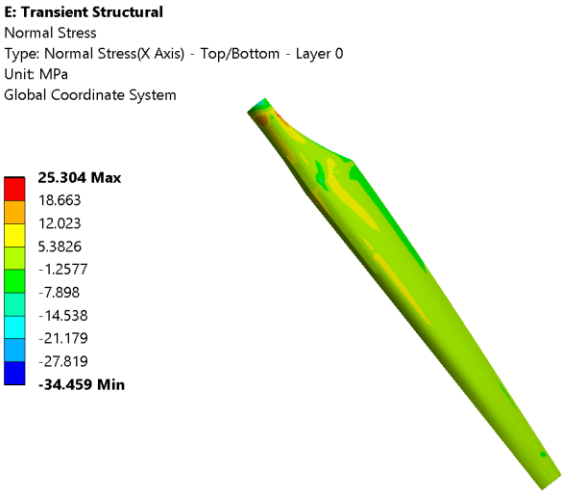

(a) Suction Side (b) Pressure Side

Figure (5.35) Distribution of Maximum Normal Stress at Wind Speed 16 m/s

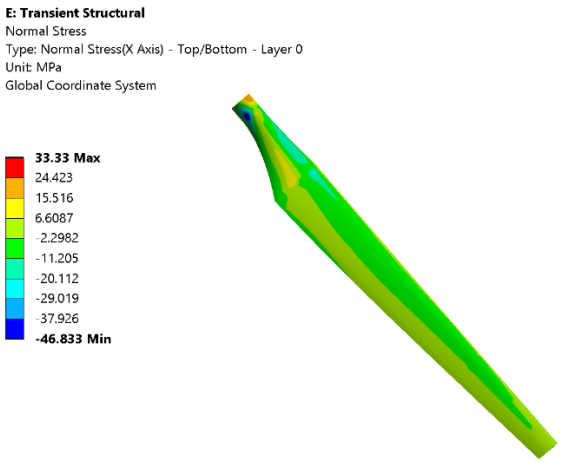

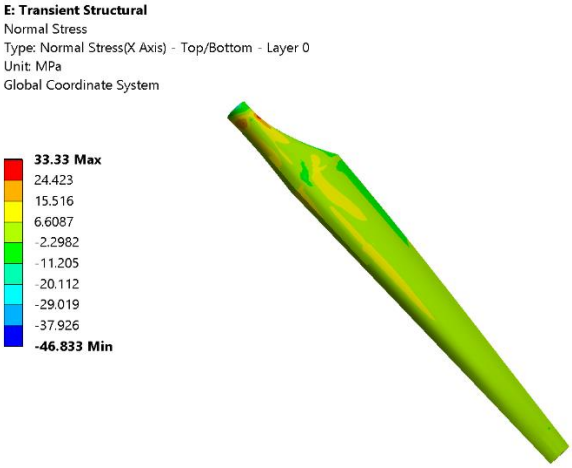

(a) Suction Side (b) Pressure Side

Figure (5.36) Distribution of Maximum Normal Stress at Wind Speed 20 m/s

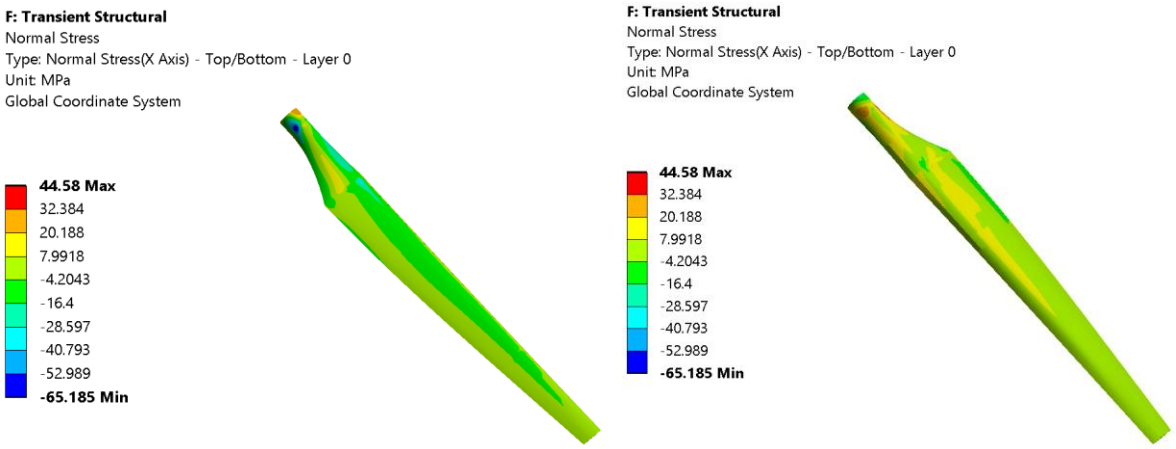

(a) Suction Side (b) Pressure Side

Figure (5.37) Distribution of Maximum Normal Stress at Wind Speed 25 m/s

The normal stress results of different wind speeds applied on the blade were represented to predict the normal stress characteristic of the blade through wind operation speeds. The chart was plotted of these results and shown the trend line sharply grows with the wind speeds change. The maximum normal stress value starts at 7.6726 (MPa) for the cut-in wind speeds to reach the highest value is 44.58 (MPa) at the cut-out speed 25 (m/s). While, the maximum negative normal stress starts at 9.4261 (MPa) of the cut-in wind speed to reach the maximum value of 65.185 (MPa) for cut-out speed. The figure (5.38) demonstrates the maximum equivalent stress through the wind speeds operation.

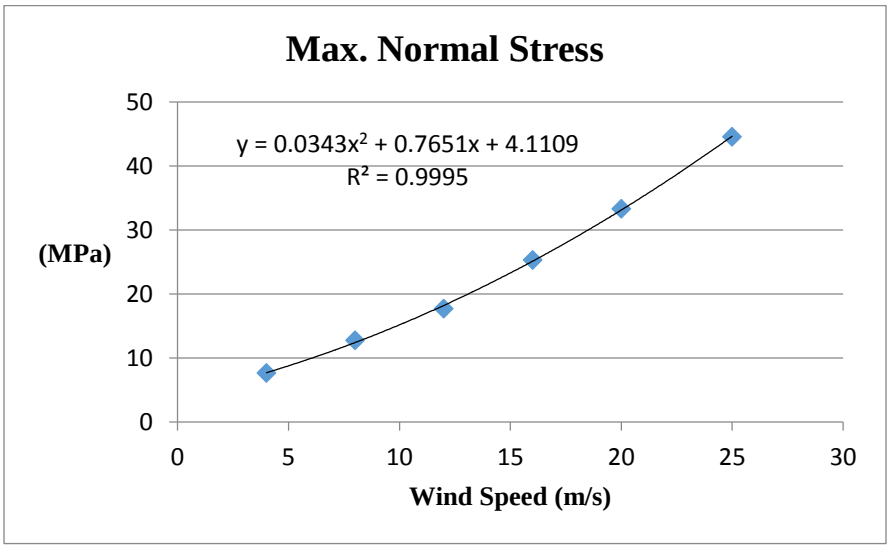

Figure (5.38) Maximum Normal Stress Trend for the Operational Wind Speeds

The fluid-structural interaction results describe the normal stress fluctuation at design wind speed over the complete step in green line and red line for positive and negative normal stress, respectively. The fluctuation results illustrated the normal stress of the value range difference over the complete step, and touched the maximum value at sub-step number 6 then it has been starting to be decreasing in the difference of the normal stress value range. Figure (5.39) shows the normal stress over the complete step at design wind speed.

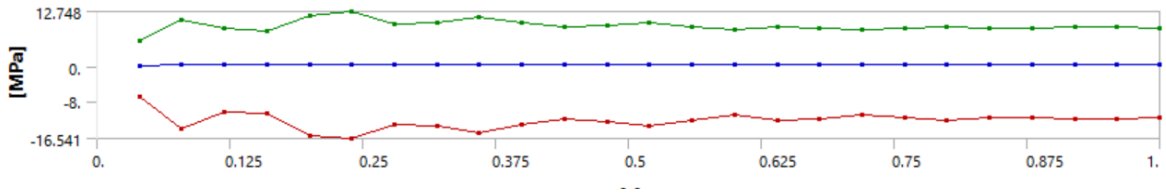

Figure (5.39) Fluctuation of Normal Stress over the Complete Step at Design Wind Speed

5.4.2 Shear Stress Analysis

The transient structural simulation was done for six wind speeds starting from cut-in speed 4 m/s with increment 4 m/s for fifth speeds and the cut-out speed was selected to be 25 m/s. The shear stress results on the blade were computed and the results of maximum shear stress over the complete step are shown in the table (5.9) for the six wind speeds among the cut-in speed to cut-out speed. The shear stress fluctuates over the complete step for each wind speeds operation, according to the shear stress distribution map on the blade, the maximum value for the positive shear stress places on the connection of root section with the hub, while for the negative shear stress places on the hub, and that's normal because the hub surfaces were selected as fixation surfaces with the rotor system. The maximum shear stress has occurred in the same steps of maximum normal stress for each operational wind speed except the design wind speed, the positive maximum shear stress has happened in step number 5 instead of step number 6. The maximum positive shear stress value was 46.681 MPa at the sub-step number 2 at cut-out speed, while the maximum negative shear stress value was 26.47 MPa. Shear stresses distribution mapped on the blade are illustrated through the figures (5.40) to (5.45) for different wind speeds operation including the design wind speed.

Table (5.9) Maximum Shear Stress Results for Different Wind Speeds

Wind Operation Speed	4 m/s	8 m/s	12 m/s	16 m/s	20 m/s	25 m/s
Max. Positive Shear Stress (MPa)	7.1049	11.913	17.699	24.859	33.484	46.681
Max. Negative Shear Stress(MPa)	-3.7992	-7.2697	-10.141	-14.641	-19.507	-26.470

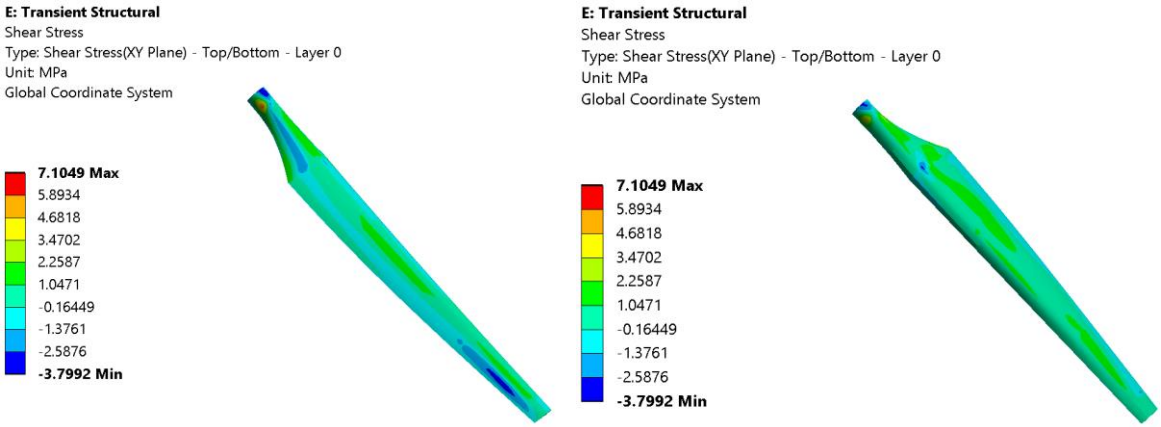

(a) Suction Side (b) Pressure Side

Figure (5.40) Distribution of Maximum Shear Stress on the Blade for Cut-in Speed 4 m/s

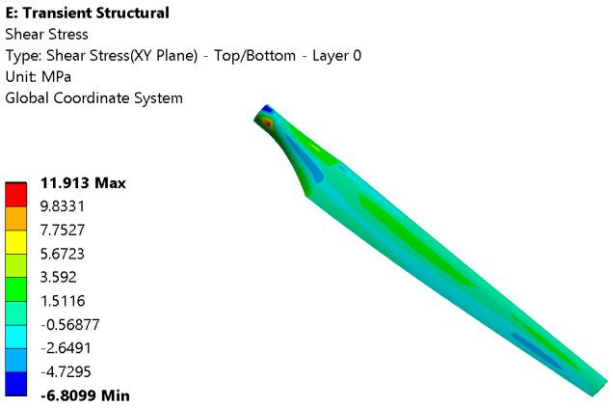

(a) Suction Side

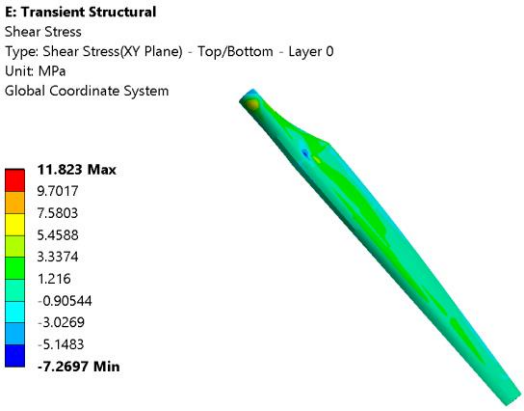

(b) Pressure Side

Figure (5.41) Distribution of Maximum Shear Stress on the Blade for Wind Speed 8 m/s

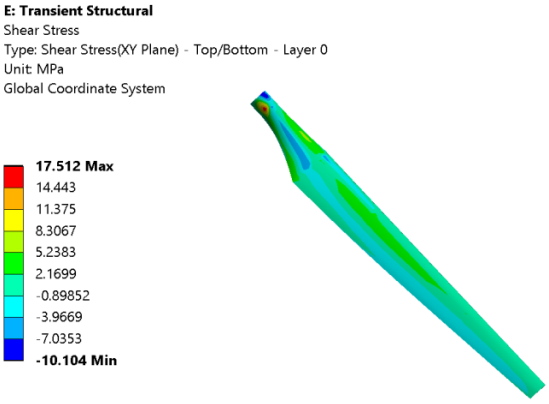

(a) Suction Side

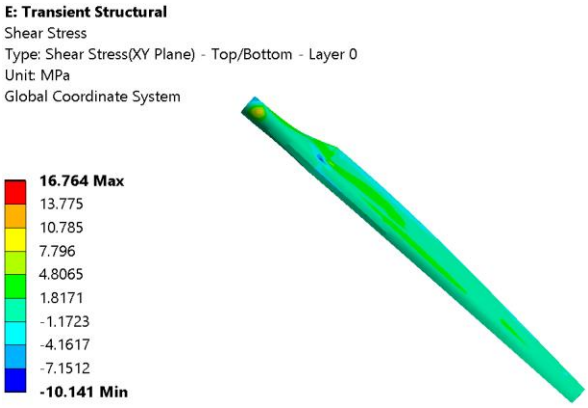

(b) Pressure Side

Figure (5.42) Distribution of Maximum Shear Stress on the Blade for Wind Speed 12 m/s

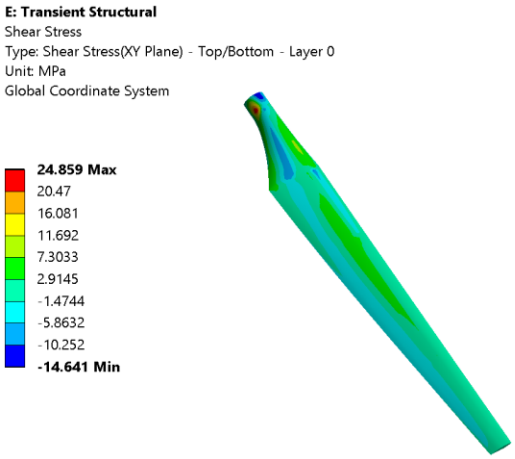

(a) Suction Side

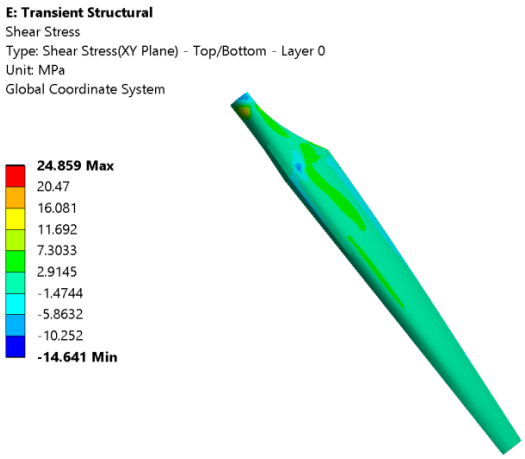

(b) Pressure Side

Figure (5.43) Distribution of Maximum Shear Stress on the Blade for Wind Speed 16 m/s

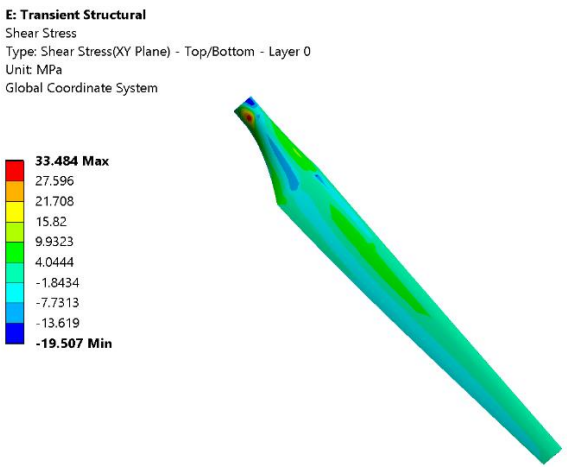

(a) Suction Side

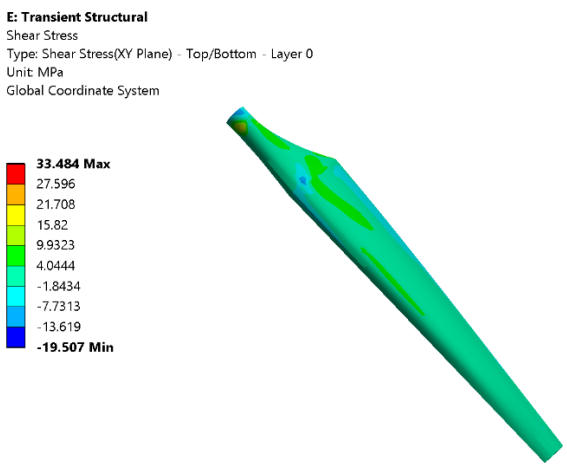

(b) Pressure Side

Figure (5.44) Distribution of Maximum Shear Stress on the Blade for Wind Speed 20 m/s

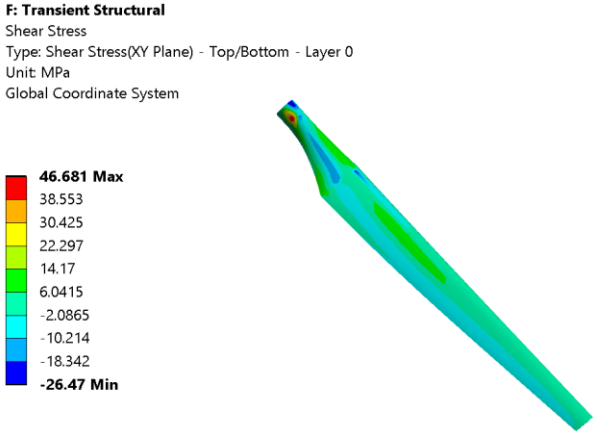

(a) Suction Side

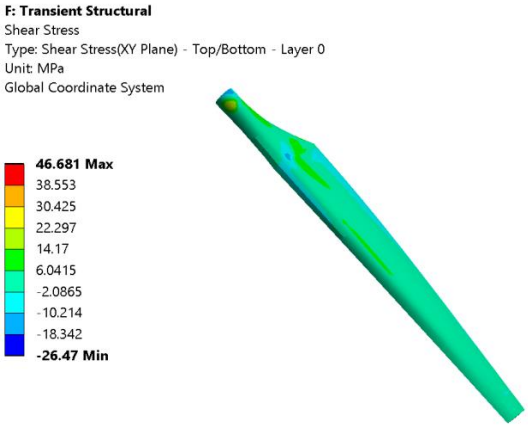

(b) Pressure Side

Figure (5.45) Distribution of Maximum Shear Stress on the Blade for Wind Speed 25 m/s

The maximum positive and negative shear stress results for the different operational wind speeds applied on the blade were used for plotting these results on a chart to predict the shear stress characteristic of the blade through various wind speeds. The results of maximum positive and negative shear stress are shown in the table (5.9). The maximum positive/negative shear stress results of the blade were represented in the figures (5.46) and (5.47), respectively, and obviously shown that the trend line of positive shear stress was raised through the different wind speeds operation to reach the maximum value (46.681 MPa), while the negative shear stress was dropped to reach the value 26.47 MPa at cut-out wind speed.

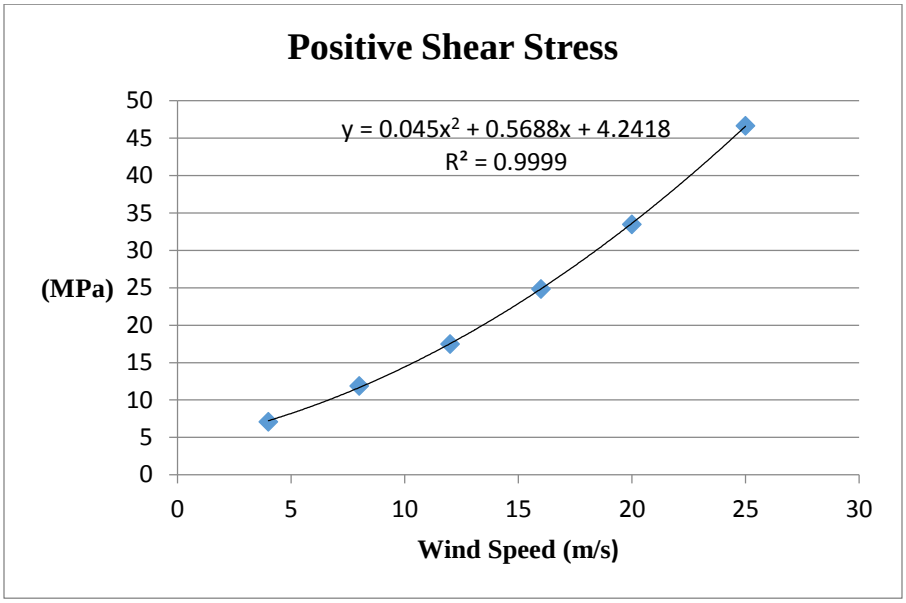

Figure (5.46) the Trend of Positive Maximum Shear Stress for the Operational Wind Speeds.

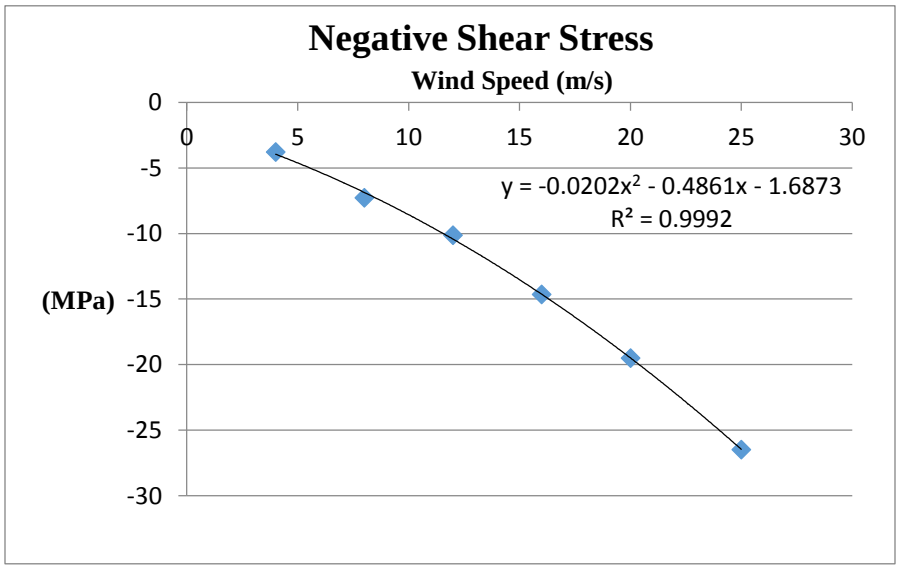

Figure (5.47) the Trend of Negative Maximum Shear Stress for the Operational Wind Speeds.

Reference to the figure (5.48) of the shear stress fluctuation at design wind speed over the complete step that obtained from the simulation of one-way fluid-structural interaction describes the shear stress fluctuation over the complete step and illustrated that the maximum range values occur on first of one-third of the complete step, then these values have started decreasing to be stable.

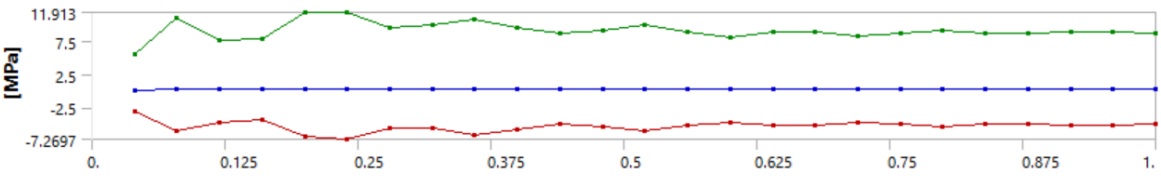

Figure (5.48) Fluctuation of Shear Stress over the Complete Step at Design Wind Speed

5.4.3 Force Reaction Analysis

Force reaction analysis of various wind speeds operation was performed to predict how much changes of force reaction magnitude and direction during the wind speeds operation regime of the system. The simulation results of the force reaction were described in the table (5.10) for the operational wind speeds regime and figure (5.49) shows force reaction direction at the design wind speed 8 m/s as an example for that. The force reaction results were represented in the figure (5.50). According to the figure (5.50), the trend line has smoothly increased through the operational wind speeds regime to touch the maximum value of the force reaction at 27471 N for cut-out speed.

Table (5.10) Resultant Force Reaction for Different Wind Speeds Operation

Wind Operation Speeds	4 m/s	8 m/s	12 m/s	16 m/s	20 m/s	25 m/s
Resultant Force Reaction (N)	8682.4	8862.1	9018.5	9589.6	10237	11533

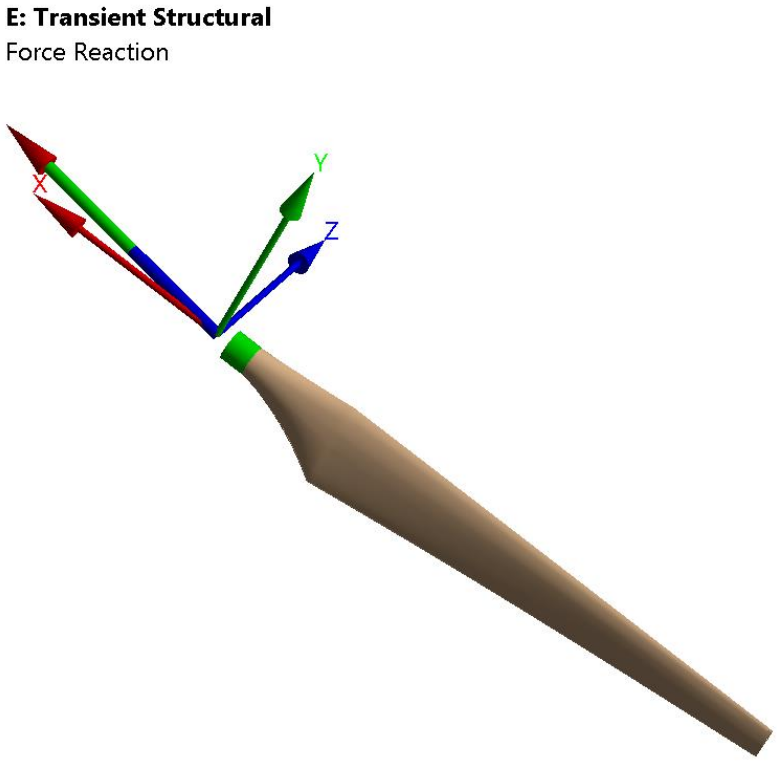

Figure (5.49) Force Reaction of Design Wind Speed 8 m/s

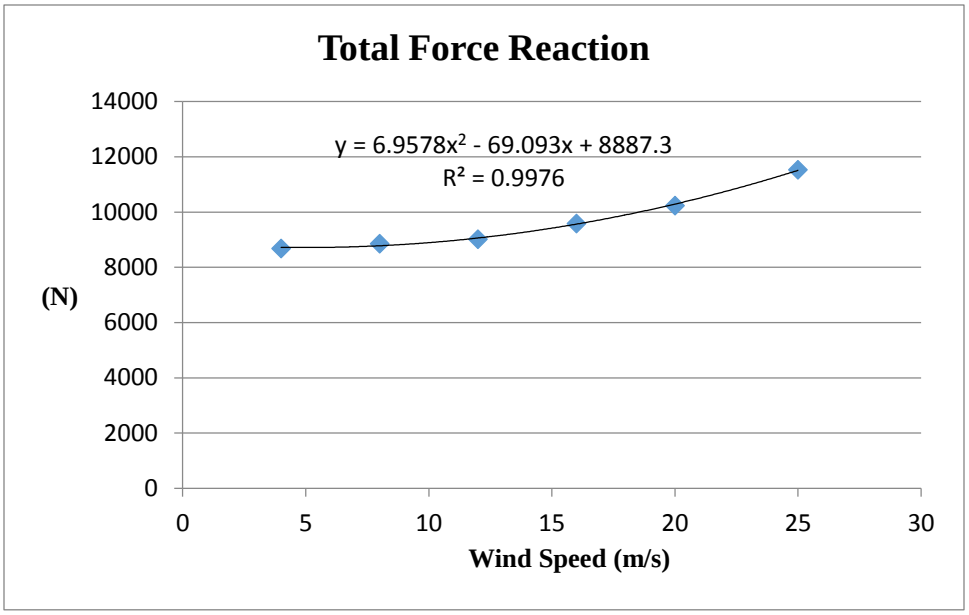

Figure (5.50) Force Reaction Trend for the Operational Wind Speeds

5.4.4 Moment Reaction Analysis

Moment reaction results for various wind speeds operation were obtained to predict how much changes of moment's reaction magnitude and direction during the wind speeds operation regime of the system. The simulation results are shown in the table (5.11) for the operational wind speeds, and the figure (5.51) shows the moment reaction direction at design wind speed 8 m/s as an example of that. The simulation results were represented of the moment reaction in the figure (5.52) for the operational wind speeds and according to the figure (5.52), the trend line has sharply raised through the operational wind speeds to reach the maximum value at 27471 for cut-out wind speed.

Table (5.11) Moment Reaction Results for Different Wind Speeds Operation.

Wind Operation Speed	4 m/s	8 m/s	12 m/s	16 m/s	20 m/s	25 m/s
Moment Reaction (N-m)	4026.0	7439.1	10462	15014	20097	27471

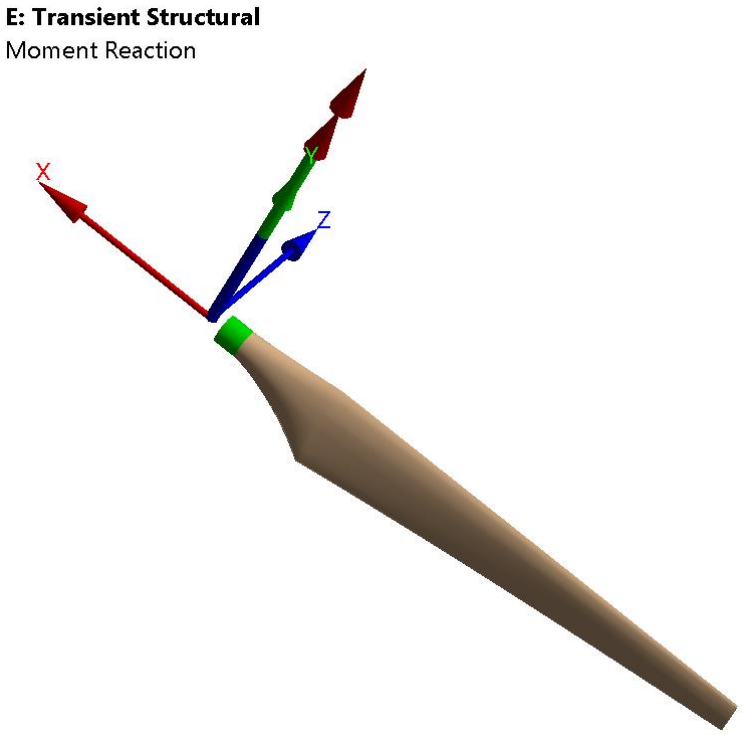

Figure (5.51) Moment Reaction of design Wind Speed 8 m/s.

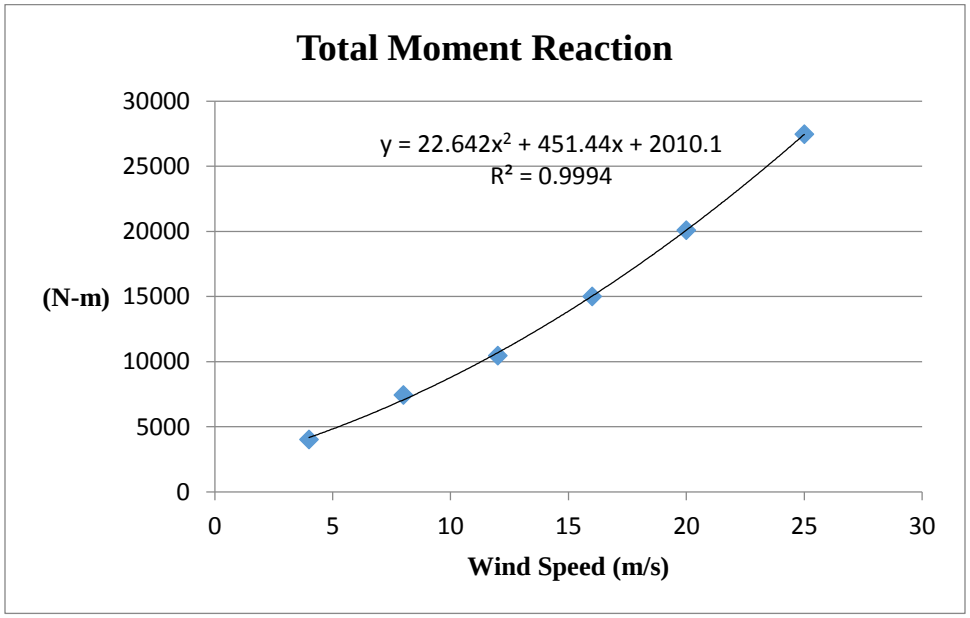

Figure (5.52) Moments Reaction Trend for the Operational Wind Speeds.

5.4.5 Blade Deformation Analysis

The simulation results of the composite material blade deformation were obtained for the operational wind speeds and the results have been described in the table (5.12). Figure (5.53) shows the deformation through the blade sections from the root to the tip blade at the design wind speed. the simulation results were represented for operational wind speeds in the figure (5.54), and the trend line has sharply increased in tip deformation of the blade by rise in wind speed to reach the maximum value 128.71 mm at cut-out wind speed 25 m/s. because it is the maximum value of blade tip deformation

during the wind turbine operation, while this value does not exceed the maximum allowable deformation which is 0.1*R=600 mm at cut-out speed, so the wind turbine works in the safe operation according to the simulation results mentioned above.

Table (5.12) Deflection of Tip Blade for different Wind Speeds Operation.

Wind Operation Speeds	4 m/s	8 m/s	12 m/s	16 m/s	20 m/s	25 m/s
Tip Blade Deflection (mm)	21.854	39.128	52.453	70.825	94.229	128.71

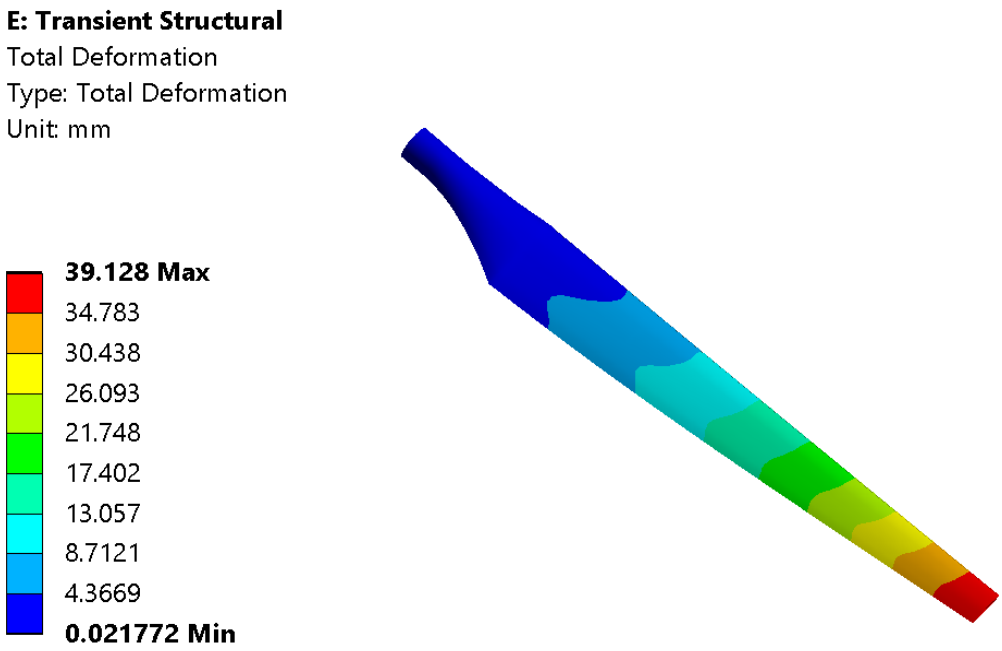

Figure (5.53) Deflection through the Blade Length at the Design Wind Speed

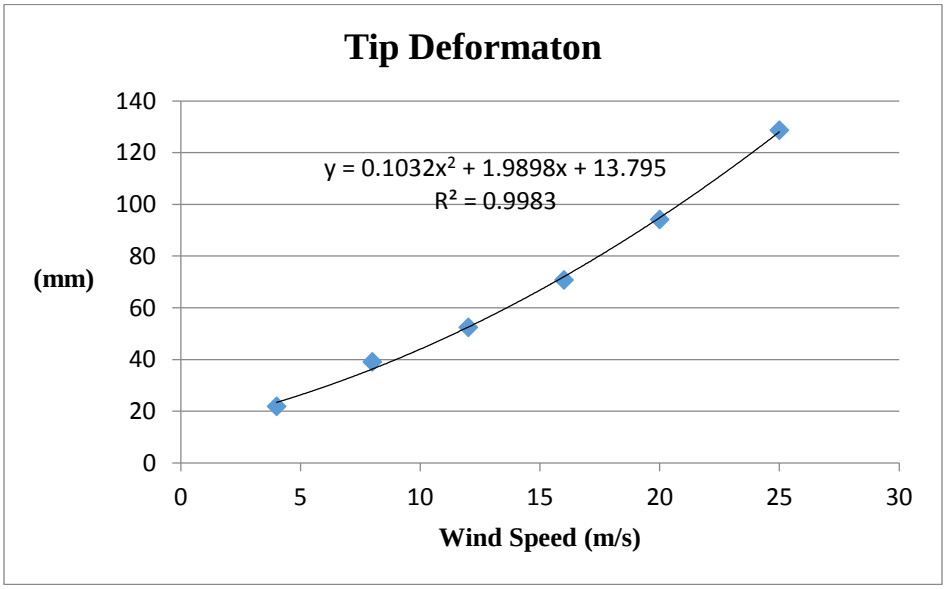

Figure (5.54) Blade Deformation at the Tip for Operational wind speeds

The fluctuation of simulation results of the one-way fluid-structural interaction describes the tip blade deformation fluctuation at design wind speed over the complete step, the figure (5.55) demonstrates the tip blade deformation fluctuation at the design wind speed, through the figure (5.55) it shows maximum values of the blade tip deformation approximately on the first one-third of the complete step to touch the maximum value at 39.128 mm in sub-step number 6 for design wind speed. Then it has reduced to be more stable.

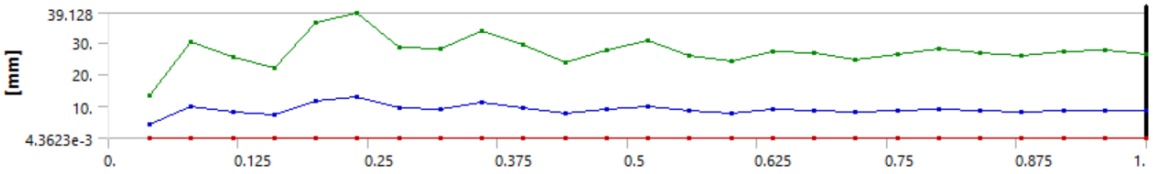

Figure (5.55) Fluctuation of Tip Blade Deformation over the Complete Step at Design Wind Speed

5.5 Two-way Transient Structure Analysis

The simulation of two-way fluid-structure interaction was performed at the cut-out wind speed for the reasons were mentioned previous, the evaluation of the wind turbine blade structure is based on the maximum aerodynamic load occurred during the operational wind speeds. In the case study, the maximum aerodynamic load is introduced on the wind turbine blade in the cut-out wind speed according to simulation results for one-way coupling. Reference to that, the simulation analysis of two-way coupling was performed and the following is a discussion of those results:

The normal stress distribution on the blade surface of the two-way coupling matched with the normal stress distribution the one-way for cut-out wind speed, while the normal stress values of the two-way are a little higher than the one-way. The figure (5.56) shows the normal stress distribution on the blade surface and placed maximum value points of the normal stress at value 54.331 and -79.537 MPa for positive and negative normal stress, respectively.

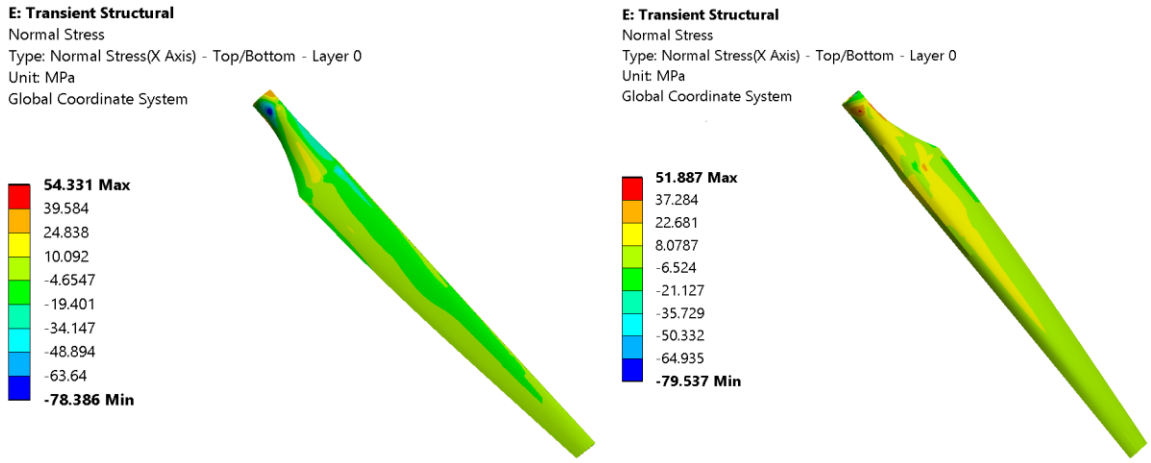

(a) Suction Side (b) Pressure Side

Figure (5.56) the Normal Stress Mapping on the Blade Surface and Placed Maximum Values

The fluctuation of normal stress was described for simulation results through the complete step to touch the maximum positive and negative normal stress value at 54.331 and -79.537 MPa at sub-step numbers 45 and 48, respectively. Figure (5.57) shows the fluctuation of positive and negative normal

stress over the complete step and obviously observed the fluctuation maximum values of normal stress have around occurred in the first of 40% from the complete step, and then the fluctuation has been more stable.

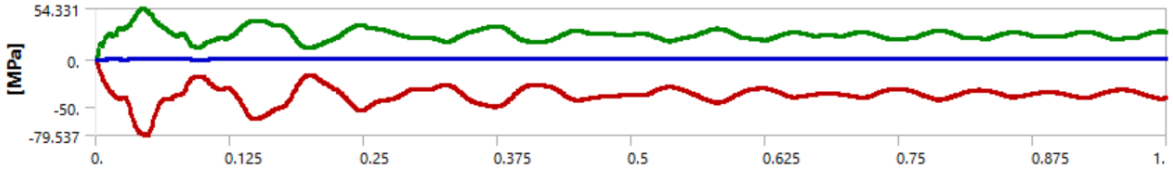

Figure (5.57) the Normal Stress Fluctuation during the Time of Simulation

The shear stress distributions on the whole blade surface illustrated in the figure (5.58) and agreed with the shear stress distribution for one-way coupling simulation, while the shear stress values were a little higher on the two-way coupling simulation results for both the positive and negative shear stresses.

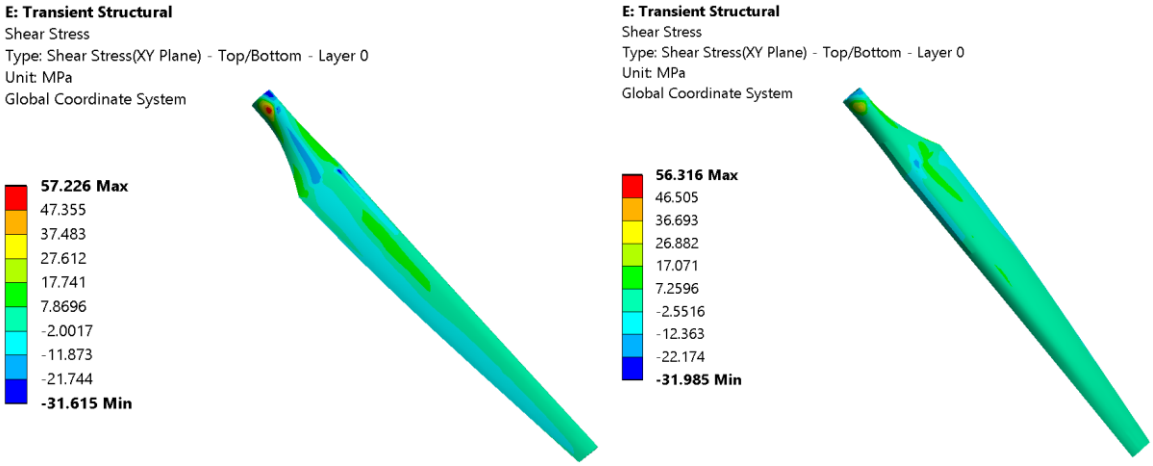

(a) Suction Side (b) Pressure Side

Figure (5.58) Shear Stress Mapping on the Blade Surface and Placed Maximum Values

The figure (5.59) shows the shear stress fluctuation through the complete step, and the maximum values of shear stress have occurred in the first of 40% of the complete step, then the fluctuation has been more stable. The maximum shear stress among these values occurred at 57.226 and 31.985 MPa in the sub-step numbers 48 and 45 for positive and negative shear stress, respectively.

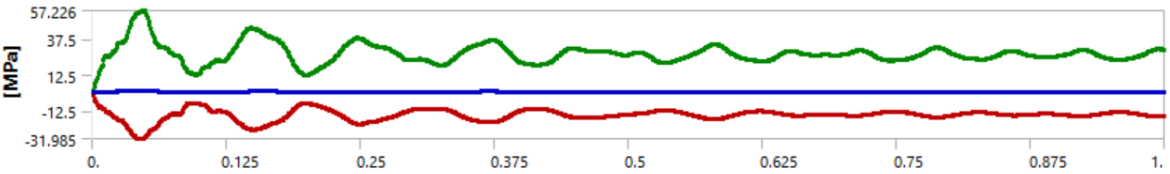

Figure (5.59) Positive and Negative Shear Stress Fluctuated during Sub-steps of simulation

The blade deformation

the deformation distribution on the blade sections for the two-way method describes in the figure (5.60) and agreed with the deformation distribution for the one-way method, while the deformation values have a little higher in the two-way method.

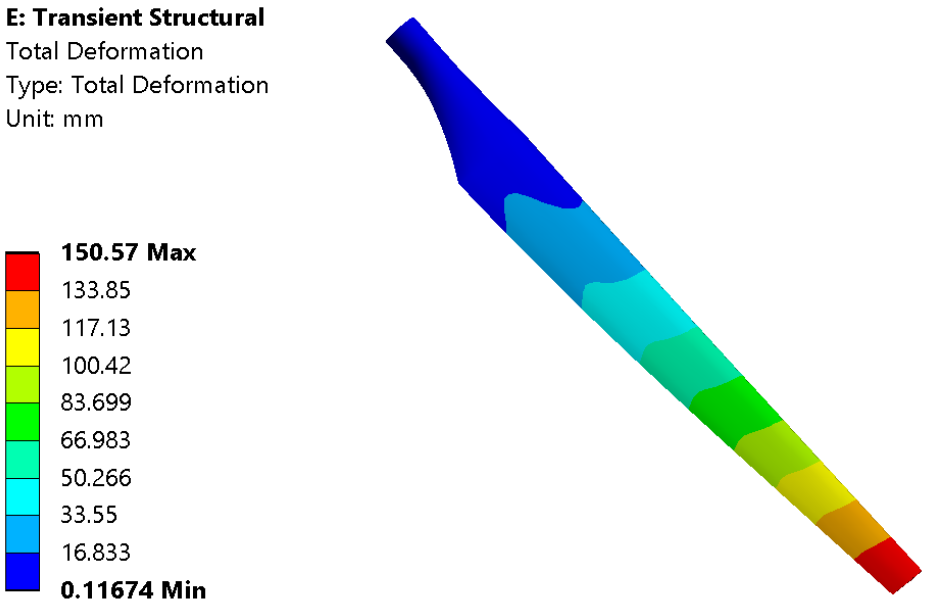

Figure (5.60) the Maximum Blade Deformation

The figure (5.61) shows the deformation fluctuation through the complete step, and the maximum values of deformation have occurred in the first half of the complete step, then the deformation has started to be more stable. the maximum deformation among the fluctuated values occurred at sub-step number 49 by 150.57 mm.

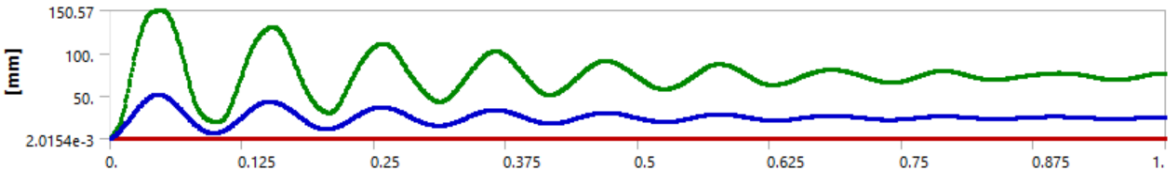

Figure (5.61) the Blade Deformation Fluctuation during the sub-steps Simulation

the simulation results have been obtained by two-way fluid-structure interaction and these results were compared with the simulation results of one-way based on the cut-out wind speed 25 m/s. those results are described in the table (5.13) and the increasing percentage is presented for the results are indicated to the one-way method.

Table (5.13) the Results Comparison Simulation of Two Methods Used

	One-way method	Two-way method	Error percentage
Maximum Blade Deformation (mm)	128.71	150.57	16.98%
Maximum Positive Normal Stress (MPa)	44.58	54.331	21.87%
Maximum Negative Normal Stress(MPa)	65.185	79.637	22.17%
Maximum Positive Shear stress (MPa)	46.681	57.226	22.59%
Maximum Negative Shear stress (MPa)	26.47	31.985	20.83%
Force reaction (N)	11533	13182	14.30%
Moment reaction (N.m)	27471	34360	25.08%

5.6 Experimental Validation

5.6.1 3D Printing Blade Model

The 3D printers can be a facilitator to impart the real-world application and knowledge in domains of most sectors science. Today the 3D printer can be used to manufacture a wide range of different material models, it is because of 3D printing today we are able to print and shape and size of any material with the most complex design which was unimaginable before.

The wind turbine blade was designed on the Catia software and then was scaled to 1: 0.24 and printed into the 3D printer in a nine of parts using plastic material, then it was collected these parts and supported by two bars of steel along the longitude axis of the blade, figure (5.62) shows the machine printer and figure (5.63) describes the printing stages of the wind turbine blade to reach the final stage of the finishing and painting.

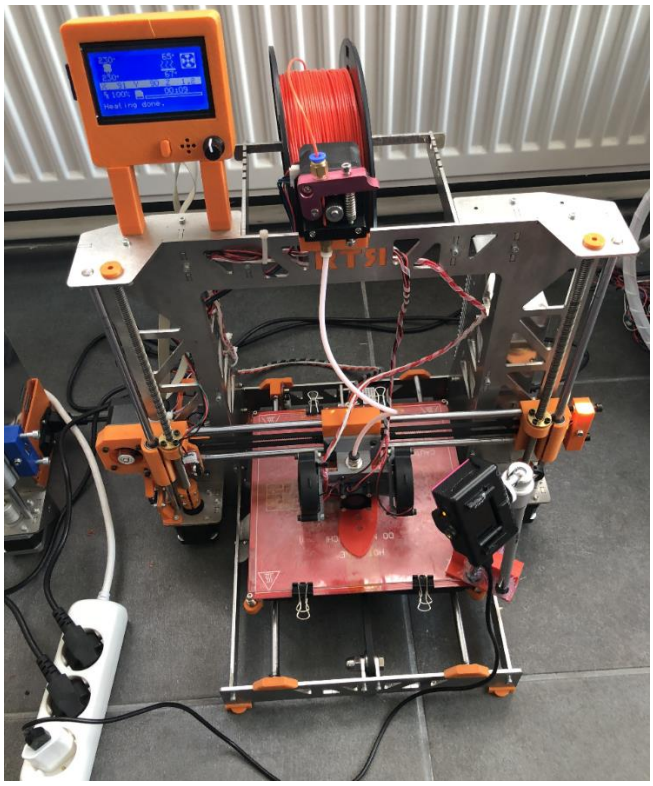

Figure (5.62) Machine Printer

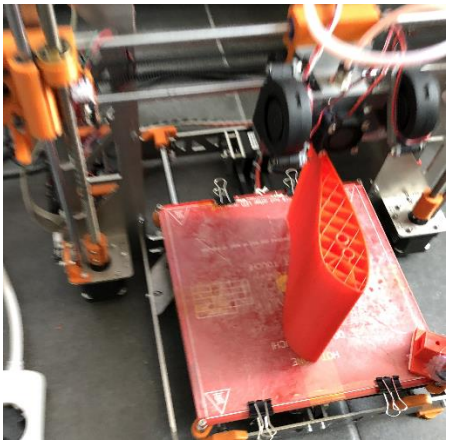

(a)

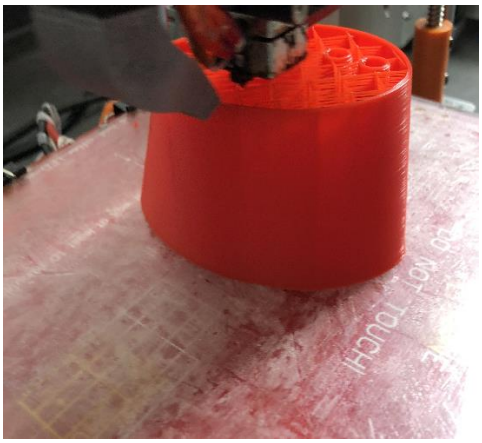

(b)

(c)

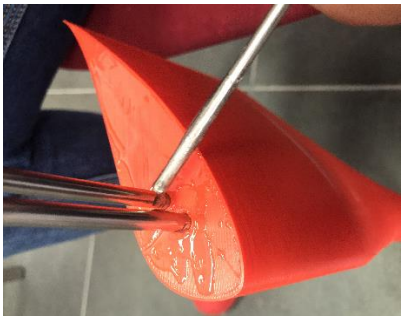

(d)

(e)

(f)

Figure (5.63) Blade Printing Stages (a) blade section (b) Hub Section (c) Complete Blade Section (d) Blade Assembly (e) Polishing Blade Surface (f) Paint and Final Model

5.6.2 Wind Tunnel Experiment

The wind turbine blade shown in the figure (5.63f) is used in the wind tunnel to test wind streamlines experimental over the blade and compare with results obtained from the simulation of CFD.

After discussion with the operational team of the wind tunnel about the way of fixation of the wind turbine blade model in the wind tunnel for a test, it was manufacturing machine of fixation the blade from the hub with an electric motor for adjustment of blade attack angle and controlled the blade height from the wind tunnel ground by the arm joints.. The machine parts manufacturing describes in figure (5.64).

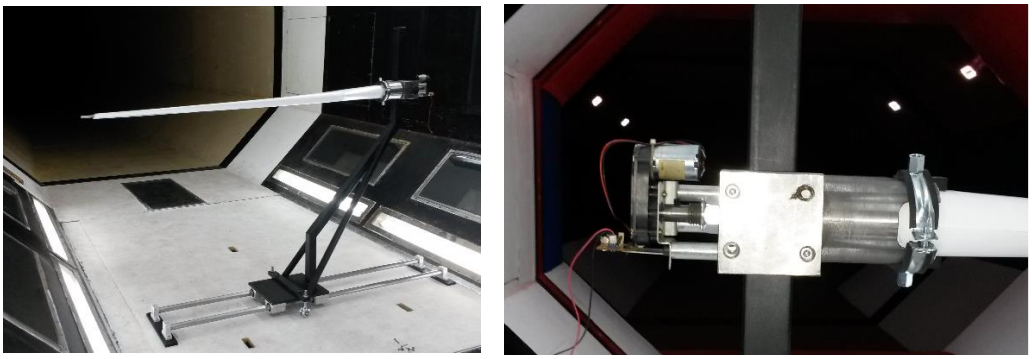

(a) Fixation Machine (b) Motorized Control of Attack Angle

Figure (5.64) Parts Description of the Blade fixation machine

1. Experiment Instruments

Can be described the Experiment Instruments as following

1. Wind tunnel with air blower and controlled of the wind speed through a computer with high specification.
2. Two of high-speed cameras picks up of the streamlines for cross-section selected on the blade and placed with an angle of a vertical plane, as well as connected with the computer to transfer the pictures has picked up.
3. High-speed laser device placed on the wind tunnel roof to provide good quality light to help the cameras to pick up in good quality.
4. Oliva oil spray connected with an air compressor to show the air streamlines more clearly on the blade cross-section.

2. The Experimental Procedure

The wind tunnel blower was started for a while to provide the wind speed selected for the test, then it started the olive oil spray in wind tunnel in front of the blade with specified distance. The laser device was started of flashing and at the same time the cameras have started to pick up the number of pictures in the cross-section selected, these pictures were transferred to the computer to analyze the wind streamlines on the blade later. The experiment procedures have performed for the operation of design wind speed and also repeated the procedure for the operation of wind speed 12 m/s and 16 m/s .figure (5.65) is shown to pick up of a picture during the test.

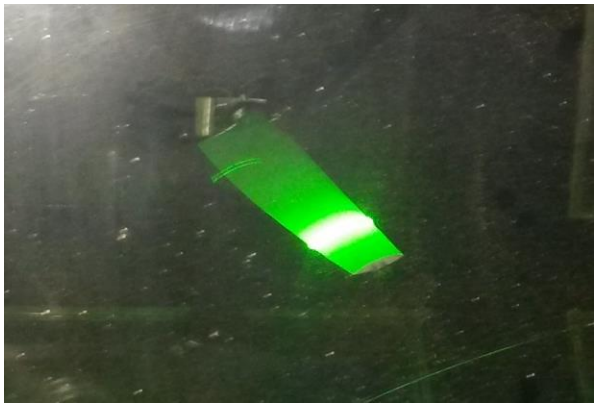

Figure (5.65) Picked up Wind Streamlines during the Test

3. Results Analysis

During the running of experimental test, it has released by visibility the fluent flow characteristic over the cross-section selected for the three operations of wind speeds 8, 12 and 16 m/s were the behavior of flow reasonable and the blade flutter was in low-level for the operation of wind speeds mentioned above. However, the experiment is focused to investigate of the blade pressure distribution or the deformation of the tip blade for the operation of wind speeds and compared these results with results were obtained from ANSYS program.

5.6.3 Digital Images correlation Experiment

For improvement of the numerical models and the precision of the structural analysis, it is important to implement experimental measurements utilizing methods allowable the measurement of displacement fields. Recently, the unconventional, non-invasive methods of experimental testing are increasingly in use - such as e.g. optical measuring system for digital image correlation. The modern experimental methods have applied for verification of numerical models achieves the emergence of models that faithfully represent the behaviour of the structure under the influence of loading under real conditions.

Using digital photography and modern software technology, a complete field of points is analysed. Digital images Correlation (DIC) systems apply a series of digital images to represent surface deformation and structural stresses.

On the other hand, due to the presence of an extremely expensive and advanced digital image link system, the movement measurement of the structure along one part of the blade surface was performed. The tape measure is affixed on around of quarter of the blade length, was tested.

1. The Experiment Instruments

1. Fixation Blade Bench: Fixation Bench is used to clamp the blade structure during the experimental procedure, this bench must be good fixing on the ground at the bench stand legs as shown in figure (5.71), the blade was clamped by the steel bars in two points to the bench fixation, and the loads were hanged by steel chains on four points as shown in the figure (5.70).

2. Digital Image Correlation System (DIC): The digital image correlation system is a non-invasive, contactless system for measuring displacement fields (and consequently deformation and stress fields). The measurement is based on taking a series of sequential photographs of the structure (in the unloaded

and loaded state or during dynamic testing), on the basis of which the field of motion and surface stress of the captured object is determined. This system is based on photogrammetry and modern computer technology to measure the full displacement field.

The three-dimensional digital image correlation (DIC) system used in Figure (5.66) consists of a sensor unit (appropriate pair of cameras), a power control device, a camera synchronization device, a data acquisition device, and an accompanying computer unit for data processing and analysis [113].

Figure (5.66) 3D DIC system used

Very important components of the DIC system used are the two ultra-fast, high-quality FASTCAM SA6 75K-M3 cameras with the following features: 50mm focal length lens, 32GB of memory, maximum recording speed of 75000 fps and maximum image resolution of 1920 × 1440 pixels is one pixel of 10 μm sensor. The weight of one camera is approximately 7 kg. Although these cameras are capable of rapid imaging, in this static test, the imaging speed was not important because individual shots were taken before and after loading (undeformed and deformed structure state). For the same reason, it was possible to take higher resolution shots, and here the image size was 1024 × 1024 pixels, which was consistent with the selected measuring surface [113].

There are a few steps to take before starting the experiment. First of all, the surface of the tested structure must be adequately prepared. It is necessary to find the appropriate pattern - stochastic pattern whose points correspond to the pixels in the photos. It should be noted that during the experiment, the pattern must remain unchanged due to tracking the displacement and collecting accurate and accurate data. This pattern contrast is usually black and white (for better recognition), so in this case, the black pattern shown in Figure (5.67) is applied to the white surface of the blade [113].

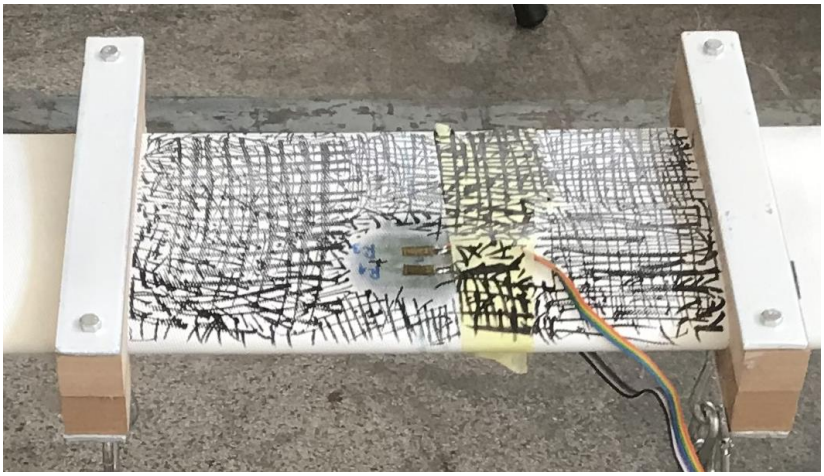

Figure (5.67) Applied Black and White Model for Test Surface

Also, it is necessary to perform the first hardware and then software adjustment, that is, system calibration. Hardware setting is primarily about setting up a sensor unit (camera). It is necessary to properly position the cameras in space so that they look at the desired part of the surface on which the movement is measured. Depending on the external illumination, the lens aperture is opened, while depending on the distance of the camera from the measuring object, the lens is properly focused. All these activities are carried out in accordance with the instructions given by the manufacturer. After the hardware setup, the system is software-calibrated using calibration bodies - objects whose characteristic lengths are known and allow the camera's field of view to be scaled to absolute dimensions. The sizes and dimensions of the calibration plates are selected according to the available cameras and the size of the measuring surface to be tested. The calibration plates, shown in Figure (5.68), contain scale data (the distance of two reference points), whereupon the calibration process itself is performed according to a very precisely defined procedure. U In this particular case, the corresponding calibration plate was set up in 13 positions different in distance from and directed towards the cameras. The necessary photographs were taken in PHOTRON, and after processing the images in ARAMIS, the necessary calibration file, shown in Figure (5.69), was formed. At each calibration step, the software must recognize the reference points of the calibration board in order for the measurement process to be correct and give accurate results. If the calibration is successfully carried out, the test process can be continued. It is a general recommendation that the deviation value is in the range of 0.01 to 0.04 pixels, but this of course depends on the size of the image. In the composite blade structure response measurements performed, the deviation (measurement accuracy) was 0.048 pixels (compared to an image dimension of 1024 pixels, the measurement error is approximately 0.005%). The dimensions of the resulting cubic measuring volume are (235 × 235 × 235) mm, which is why approximately one-fifth of the surface of the blade (about 20 cm) was recorded. At all times during the recording process, the deformed structure should not exceed the limits of the measuring volume [113].

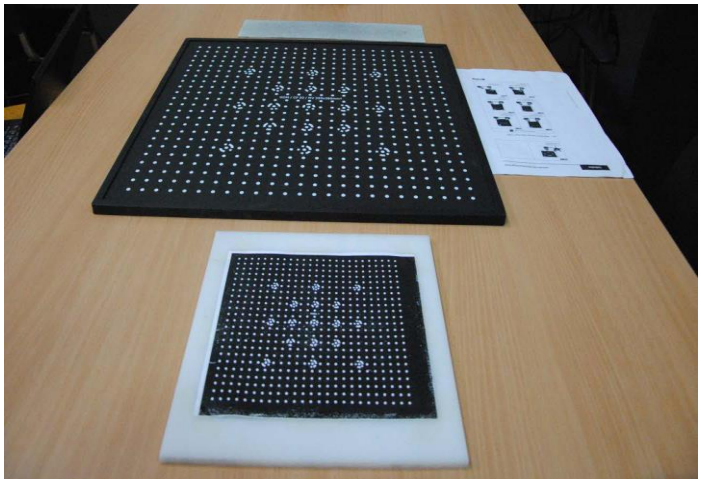

Figure (5.68) Calibration Plates of the Digital Images Correlation System

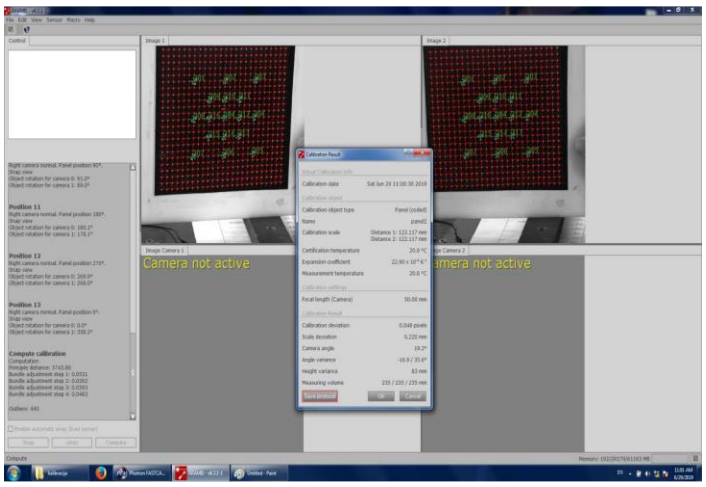

Figure (5.69) Calibration File Example

Snapshots of the structure were realized using commercial software PHOTRON. The blade was first taken in an undeformed state, and then the changed positions of the structure due to the effect of the specified loads were imaged. The photographs were then imported into a commercial software package for the processing and calculation of ARAMIS results. The software analyses and compares the state of the structure before and after deformation. ARAMIS measures deformations in the range of 0.01 to 2000%, as well as displacements up to 1 μm, which is significant when measuring three-dimensional displacements and determining the behaviour of a real structure. The advantage of the DIC procedure is the visualization of the spatial displacement field at places of geometric irregularities of the structure, so that they can be directly compared with the results obtained by the finite element method with a high degree of precision. The ARAMIS software calculates the coordinates of the highlighted structure by mathematically analysing (correlating) the "facets" - the elemental parts of the image, captured by the left and right cameras. The captured two-dimensional coordinates are translated into spatial, three-dimensional using two cameras and a calibration file. By further comparing the coordinates of the points in two consecutive stages, it is possible to obtain a complete displacement field (which was done during the show experiments). The dimensions of the "veneers" were chosen according to the size of the surface to be tested and the fineness of the applied pattern, and in this measurement were (15 × 12) pixels. In order to speed up the analysis of the images taken, it is possible to define a mask that does

not consider the part of the photographs that does not relate to the exposed surface on which the measurement is made [113].

2. Experimental Set Up

The experiment was performed in multiple locations of the forces input. The blade was clamped in two cross-sections at 25% and 75% of the blade length, while the force was applied 10 kg in four different longitudinal coordinates which are12.5%, 37.5%, 62.5% and 87.5% of the blade length. Figure (5.70) is shown the fixation points locations and applied forces. The figure (5.71) is illustrated the realistic installation of the composite blade [113].

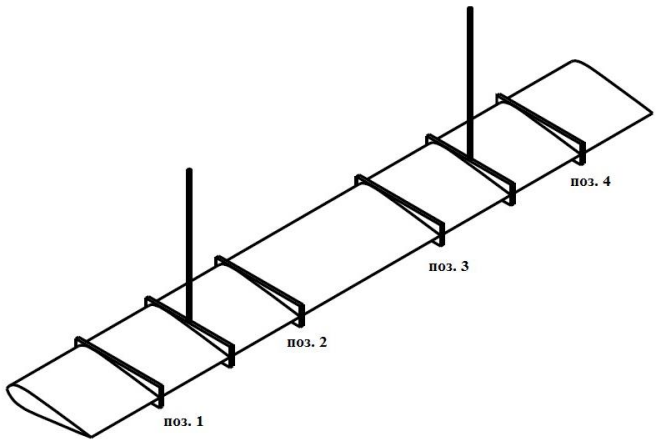

Figure (5.70) Method Fixation of the Blade and Places of Loading

Figure (5.71) Test Installation with Paddle Set

3. Results Analysis

the boundary conditions applied in the available experimental method in literature is considered, the fixation points locations and applied forces of the blade were implemented, the results of finite element are achieved and compared these results with the available experimental data were obtained by the digital image correlation. the analysis and comparison of available experimental data in literature was

performed with the finite element analysis for the structure surface deformation of the blade and spite of the procedure steps and applied the boundary conditions of the experiment as available experiment data in the literature on the finite element analysis, while the comparison results was not agree for the blade structure surface deformation. The figures (5.72) and (5.73) are shown the deformation in the finite element analysis and the digital image correlation method, respectively. In addition, the finite element analysis results are in agreement with the finite element analysis in available experiment data in the literature. Figure (5.74) illustrates the deformation result of the finite element method in literature.

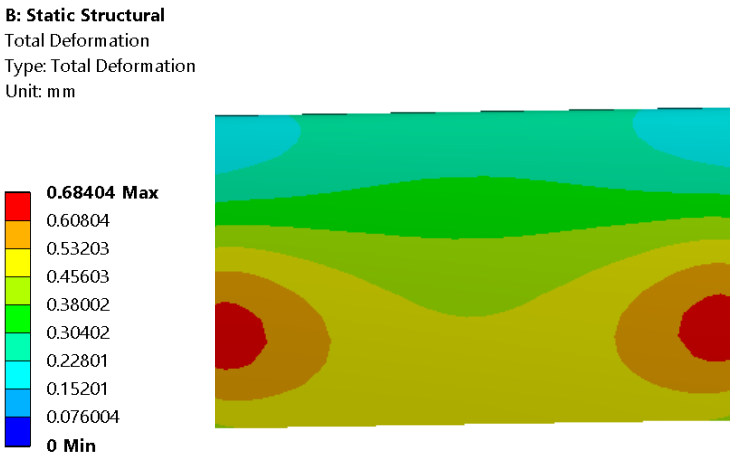

Figure (5.72) Deformation of the Blade Testing Area (FEA)

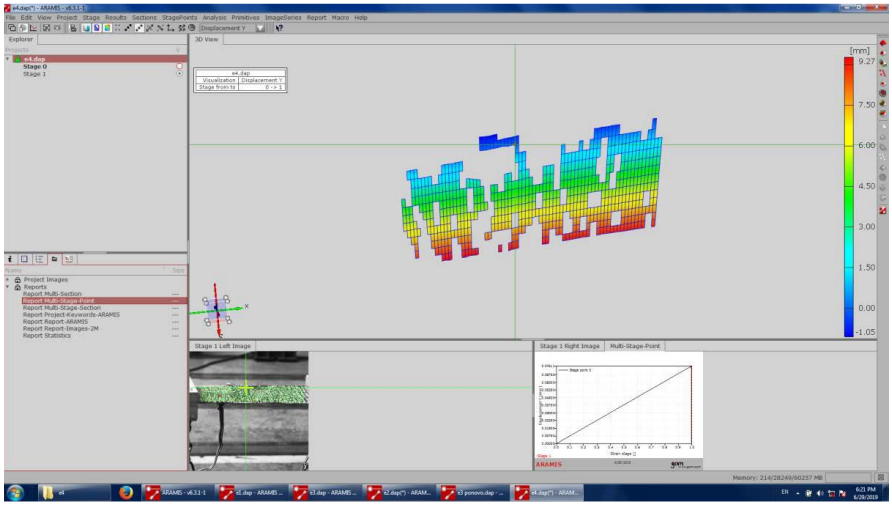

Figure (5.73) Deformation Analysis of DIC Method in ARAMIS software [113]

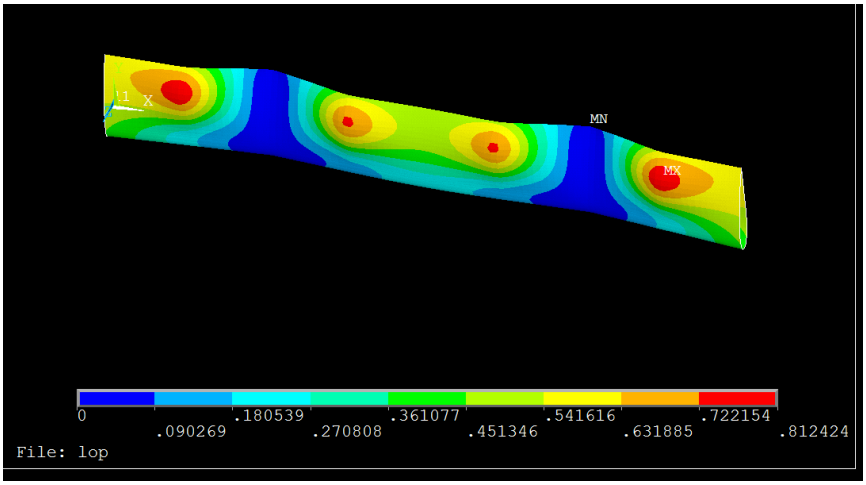

Figure (5.74) Deformation of the Blade Testing Area (FEA) [113]

CHAPTER SIX
CONCLUSION

The simulation of the fluid-structure interaction system coupling helps the designers of a wind turbine to choose the proper composites material of blades which is achieved the main requirements of the blade structure according to aerodynamic behavior, such as less weight of the blade and in the same time, it has the ability to resist the stress and shear stress during the operational wind speeds. This thesis conducted for the optimization of a composite structure of the wind turbine blade utilizing the Fluid-Structure Interaction code. In the first step, the wind turbine blade redesigned with the three different airfoils along the blade by the Catia software for improving the aerodynamic flow over the blade. Later the wind turbine model was imported to the simulation of fluid-structure interaction application. The fluid-structure interaction was performed for the five composite materials studied at cut-out wind speed and the comparison of those simulation results was executed with the properties of each one to choose which the ones will be proper for the blade structure at the applied condition. The numerical results show that the composite material ARAMID (Kevlar 49/Epoxy 5505) is the most proper composite material among the five composite material applied for this studying for many reasons as the blade less weight, the maximum value of the positive and negative normal stress 44.58, 65.185 MPa, respectively for one-way method. While, the two-way method the maximum positive and negative normal stress are 54.331, 79.537 MPa, respectively. These values are most reasonable compared with the laminate tensile strength 729.758 MPa among the other composite materials, and the maximum value represents around 10.9% of laminate tensile strength. The maximum tensile and compressive of shear stress are in the safe mode. The maximum deformation occurring on the blade is less than the recommended maximum allowable deformation value of 0.1*R=600 mm as in the reference [ ], the maximum deformation values at the cut-out wind speed are 128.71 mm in one-way method and 150.57 mm in two-way method, which are equivalent of 21.5% and 25.1% of the blade length, respectively.

A 3D unit cell FE model of low level porosity in form of closed pores is developed and compared with available experimental results. The low-level porosity has significant influence on strength of structural material.

Shape of porosity has an impact on estimated strength of structural material. For fixed volume fraction, changing shape of pores by increasing aspect ratio (AR) in general slightly decreases values for SCF which contributes to higher strength.

Volume fraction of porosity has a significant impact on strength. Less porosity in the material microstructure generally leads to noticeable higher values of strength. It is shown that values of estimated strength predicted by UCNM model for PL load case and AR=3 are in good agreement with previously published experimental data. For all other aspect ratios and load cases estimated decreases of strength were much lower than the values obtained experimentally.

Finally, presented UCNM model are capable to simulate microstructure irregularity of closed pores shape and size regarding the influence of presence of such porosity to strength of structural material.

The numerical simulations of the blade structure for one-way coupling have been implemented for the static and transient structure responses and compared those results a reference to parameters maximum normal stress, shear stress, force reaction, and moment reaction for each wind speed. The numerical results were plotted in graphs for each parameter separated for the investigation of the structural response of the blade through wind speeds applied. These graphs described the character of the growth of the trend line for each parameter individually for both the static and transient structures.

the numerical results of the transient structural demonstrated higher values than the numerical results of static structural, and sometimes, these results are roughly three times more the static structure in most results except the force reaction. While the parameters of the maximum normal stress, shear stress, and deformation fluctuated during the complete step in the transient results, these maximum values occurred in different sub-steps numbers during the operation of first the three wind speeds. But for remaining wind speeds the maximum values have occurred in the same sub-step number 2. The wind turbine blade has a reasonable distribution of normal stress but it showed the singularity points of normal stress as maximum values, this singularity values of maximum normal stress were located in different places on the blade with changing the operation of wind speeds, can be an explanation of this phenomenon the resulting of sharp edges in some parts of the blade. The wind turbine blade has a reasonable distribution of normal stress but it showed the singularity points of normal stress.

From the observation of the one-way coupling results, the normal stress, shear stress, and blade deformation distributions on the blade surface are symmetric for each parameter in different wind speeds, and the values are increased by increasing the wind speed, which is normal, because of the aerodynamic loads are increased with a rise of wind speed. The maximum positive and negative shear stress is located in the hub section because this section has been selected as a fixation part with the wind turbine rotor system. Moreover, there are other two positioning's of maximum negative shear stress, one as longitude strip in the root section and the other as singularity point on the connections of spar cup and first blade with the root section.

According to the shear stress fluctuation over the complete step of one-way coupling shows that the maximum range values occur on the first one-third of the complete step. The shear stress touches the maximum of positive and negative value 11.913 MPa at sub-step number 5, and 7.2697 MPa at sub-step number 6, respectively for the design wind speed.

According to the results of the transient structure, the blade deformation fluctuates over the complete step and touched the maximum deformation in different sub-steps numbers with changing the operational wind speeds where the maximum deformation occurs at sub-step number 6 at the design wind speed with a value of 39.128 mm, while happened at sub-step number 2 at cut-out wind speed with value of 128.71 mm. the maximum blade deformation results were plotted in the chart and represented the trend line by a parabola line over the operational wind speeds. However, the maximum deformation is less than the recommended maximum allowable deformation value of 0.1*R=600 mm as it's mentioned above.

In static structural results, there is no much of considerable changing of force reaction during operation of wind speeds. While the transient structural results, the force reaction value has increased in the operational wind speeds from 8361.1 (N) at cut-in wind speed to 8690 (N) at the cut-out wind speed. The force reaction results were plotted in a chart and represented the trend line in a parabola curve over the operational wind speeds.

Moment reaction results of both static and transient structures were raised in values during the operational wind speeds and that's normal because the aerodynamic influence on the blade has been increasing as the wind speed increase, these results trend line were represented a sharp parabola curve. The transient structural results of moment reactions for cut-in, design, and cut-out speed were 4026.0, 7439.1, and 27471 (N-m) respectively.

The two-way fluid-structure interaction was implemented at the cut-out wind speed 25 m/s to compare the structural response results to one-way Fluid-structure interaction. The FSI results of two-

way were shown higher values than one-way by around 20% except for the force reaction and tip deformation which shows higher values by around 15%. However, according to the figures results were obtained the normal stress, shear stress, and deformation two-way FSI have fluctuated to touch the maximum values for each in first of 40% of the complete step, and then the range wave values have reduced during the remaining complete step simulation to be in a semi-stable situation.

REFERENCES

[1] Global Wind Statistics 2017 by Global Wind Energy Council (GWEC). https://gwec.net/wp-content/uploads/vip/GWEC_PRstats2017_EN-003_FINAL.pdf

[2] Robert W. Righter. Wind Energy in America: A History. University of Oklahoma Press, 1996.

[3] Ahmad Y. al Hassan. Islamic Technology: An Illustrated History. Cambridge University Press,1992.

[4] Donald R. Hill.Mechanical engineering in the medieval near east. Scientific American, pages64–69,May 1991.

[5] LynnJr.White. Medievaltechnologyandsocialchange. Oxford,1962.

[6] T. Lindsay Baker. Brief history of windmills in the New World. URL http://www. windmillersgazette.com/history.html. Retrieved: 2013-05-29.

[7] Niki Nixon. Timeline: The history of wind power, Oct. 2008. URL http://www. guardian.co.uk/environment/2008/oct/17/wind-power-renewable-energy. Retrieved: 2013-05-28.

[8] Smith Putnam Wind Turbine on Grandpa's Knob in Vermont, circa 1941 Caption https://wikivisually.com/wiki/Smith-Putnam_wind_turbine

[9] https://www.mhivestasoffshore.com

[10] Xiaomin Chen,"Optimizaton of Wind Turbine Airfoils/Blades and Wind Farm Layouts" Dissertation of Doctor of Philosophy-May 2014.

[11] D.L.V.Subrahmanyam, Kuppili.Mohan Krishna, Sammala.Rajasekhar, Y.Dhana Sekhar, "Design and Material Optimization of Wind Turbine Blade" ISSN 2321-6905 October-2015.

[12] Turkey in the Wind. 2007 [cited 2013 August 20th]; Available from: http://jcwinnie.biz/wordpress/?p=2330

[13] Gipe, P. Vertical Axis Wind Turbine.Wind-works.org 2013 [cited 2013 August 20th]; Available from:http://www.windworks.org/cms/index.php?id=399&tx_ttnews[tt_news]=2194&cHash= d1b21f3bd1f35d9e 4804f1598b27bd86.

[14] Xinzi Tang, Ruitao Peng, Xiongwei Liu, Anthony Ian Broad, "Design and Finite Element Analysis of Mixed Aerofoil Wind Turbine Blades",

[15] "Wind Turbine Airfoils." Wind Turbine Airfoils. Web. 23 Nov. 2013. <http://wind.nrel.gov/airfoils/>.

[16] Seul-Ki Yeom, Tae-Jin Kang, Warn-Gyu Park, "Aerodynamic Design of 2.5 MW Horizontal Wind Turbine Blade in Combination with CFD Analysis". The 2013 world congress on ASEM13, Jeju, Korea, September 8-12, 2013.

[17] Mohammadreza Mohammadi, Alireza Mohammadi and Said Farahat," A New Method for Horizontal Axis Wind Turbine (HAWT) Blade Optimization", IJRED – ISSN: 2252-4940, February 15th, 2016.

[18] Mojtaba Tahaania, Tahmine Sokhansefata, Kiana Rahmania and Pouna Ahmadib, "Aerodynamic Optimal Design of Wind Turbine Blades using Genetic Algorithm", energyequipsys/ Vol. 2/No2/AUG 2014/ 185-193.

[19] Vipinkumar Satankar, Dr. Vilas Warudkar, "Modeling and aerodynamic analysis of small scale, mixed airfoil HAWT blade." International Research Journal of Engineering and Technology (IRJET), Volume: 03 Issue: 11/Nov-2016, e-ISSN: 2395 -0056, p-ISSN: 2395-0072, 2016.

[20] Nitin Tenguria, N.D. Mittal, Siraj Ahmed**,"** Investigation of blade performance of horizontal axis wind turbine based on blade element momentum theory (BEMT) using NACA airfoils", International Journal of Engineering, Science and Technology, Vol. 2, No. 12, 2010, pp. 25-35.

[21] Md Mehedi Hasan, "Design and Performance Analysis of Small Scale Horizontal Axis Wind Turbine for Nano Grid Application." Master Thesis 2017, Graduate Faculty of Georgia Southern University.

[22] Farhan Javed, Salman Javed, Taha Bilal and Vikas Rastogi; "Design of Multiple Airfoil HAWT Blade Using MATLAB Programming", 2016 IEEE International Conference on Renewable Energy Research and Applications (ICRERA), Birmingham, UK, DOI: 10.1109/ICRERA.2016.7884373.
[23] Dylan Perry, "Aerodynamic Design and Structural Analysis Procedure for Small Horizontal-Axis Wind Turbine Rotor Blade." Master Thesis 2015, Faculty of California Polytechnic State University.
[24] Verónica Cabanillas Sánchez, "Blade Performance Analysis and Design Improvement of a Small Wind Turbine for Rural Areas.", Master of Science 2013, Purdue University.
[25] Innovating Clean Energy Technologies in Advanced Manufacturing "Technology Assessments-Composite Materials" Quadrennial Technology Review 2015
[26] Ayşegül Akdoğan Eker, Bülent Eker, "General Assessment of Fiber-Reinforced Composites Selection in Wind Turbine Blades", Mechanical Engineering Department, Yıldız Technical University, İstanbul, Turkey, 20, December 2013.
[27] S. K. Mutkule/ P. P. Gorad/ S. R. Raut/ A. H. Nikam," Optimum and Reliable Material for Wind Turbine Blade", International Journal of Engineering Research & Technology (IJERT), ISSN: 2278-0181, Vol. 4 Issue 02, February-2015.
[28] N.Saravana Kumara, G.VinothKumarb*, C.VinothKumarc, M.Prabhud;"Experimental Investigation on Mechanical Behavior of E-Glass and S-Glass Fiber Reinforced with Polyester Resin." SSRG International Journal of Mechanical Engineering (SSRG - IJME); ISSN: 2348 – 8360, Volume 5 Issue 5 – May 2018
[29] Sowdager Moin Ahmed; "Design and Analysis of Horizontal Axis Windmill Turbine Blade."; International Journal of Innovative Research and development; ISSN 2278-0211.
[30] Amol V. Deshmukh and Prof. Dr. Sanjay P. Shekhawat;" Analysis on Wind Turbine Blade Using Composite Materials."; International Journal of Innovative Research in Science, Engineering and Technology; ISSN (Online) : 2319 – 8753; ISSN (Print) : 2347 – 6710.
[31] Souad A. M. AlBat'hi, Yose Fachmi Buys, Muhammad Hazwan Hadzari and Maizatulnisa Othman;" A Light Material for Wind Turbine Blades."; Trans Tech Publications, Switzerland Accepted: 2015-03-26; doi:10.4028/www.scientific.net/AMR.1115.308.
[32] Leon Mishnaevsky Jr., Kim Branner, Helga Nørgaard Petersen, Justine Beauson, Malcolm McGugan and Bent F. Sørensen;" Materials for Wind Turbine Blades."; www.mdpi.com/journal/materials; Materials 2017, 10, 1285; doi:10.3390/ma10111285.
[33] Hti Lar Tun Kyi, Theingi and Khaing Thida, "Design Model of Horizontal Axis Wind Turbine Blade at Technological University (Thanlyin).", International Journal of Science and Engineering Applications Volume 7–Issue 06,94-100, 2018, ISSN:-2319–7560.
[34] Nawapon Sompong and Pongtorn Prombut, "Effects of Bend-Twist Coupling Deformation on the Aerodynamic Performance of Wind Turbine Blade.", International Journal of GEOMATE, June,2017, Vol.34 Issue 34, pp. 15-20, Geotec., Const. Mat. & Env., ISSN:2186-2990, Japan, DOI: http://dx.doi.org/10.21660/2017.34.2643.
[35] Haci Sogukpinar and Ismail Bozkurt, **"**Calculation of Optimum Angle of Attack to Determine Maximum Lift to Drag Ratio of NACA 632-215 Airfoil.", Journal of Multidisciplinary Engineering Science and Technology (JMEST) ISSN: 3159-0040 Vol. 2 Issue 5, May – 2015.
[36] Richard W. Vesel Jr., "Aero-Structural Optimization of a 5 MW Wind Turbine Rotor.", Master Thesis 2012, The Ohio State University.
[37] Jelena Svorcan, Ognjen Pekovic, and Toni Ivanov, "Estimation of Wind Turbine Blade Aerodynamic Performances Computed Using Different Numerical Approaches.", Theoretical and applied Mechanics Volume 45 (2018) Issue 1, 53–65 DOI: https://doi.org/10.2298/TAM171130004S.

[38] Chenyu Zhang, "Aerodynamic, Structural and Aero-elasticity Modelling of Large Composite Wind Turbine Blades.", Doctoral Thesis 2013 Loughborough University, School of Aeronautical, Automotive, Chemical and Materials Engineering Loughborough University, March 2013.
[39] Jihoon Jeong, Kyunghyun Park, Sangook Jun, Kisun Song and Dong-Ho Lee, "Design optimization of a wind turbine blade to reduce the fluctuating unsteady aerodynamic load in turbulent wind.", Journal of Mechanical Science and Technology 26 (3) (2012) 827~838, DOI 10.1007/s12206-011-1106-4, www.springerlink.com/content/1738-494x
[40] Dr. Abdullateef A. Jadallah, Dr .Dhari Y. Mahmood and Zaid A. Abdulqader, "Optimal Performance of Horizontal Axis Wind Turbine for Low Wind Speed Regime.", International Journal of Multidisciplinary and Current Research,ISSN: 2321-3124.
[41] LinWang, Xinzi Tang, and Xiongwei Liu, "Blade Design Optimisation for Fixed-Pitch Fixed-Speed Wind Turbines.", International Scholarly Research Network, ISRN Renewable Energy, Volume 2012, Article ID 682859, 8 pages, doi:10.5402/2012/682859.
[42] Xiongwei Liu, Lin Wang and Xinzi Tang, "Optimized linearization of chord and twist angle profiles for fixed-pitch fixed-speed wind turbine blades.", Renewable Energy 57 (2013) 111e119.
[43] Robin Johny, David Solomon and Suresh Kumar , "Design Optimization and Aerodynamic Performance Analysis of a Small Wind Turbine Blade.", International Journal of Engineering Trends and Technology (IJETT), Volume-44 Number-1, February 2017, ISSN: 2231-5381.
[44] Praveen Kadlimatti, Thulasi durai and R. A. Savanur, "Composite Design Optimization and Weight Reduction for 10 KW (HAWT) Blades.", International Journal of Mechanical and Production Engineering, ISSN(p): 2320-2092, ISSN(e): 2321-2071.
[45] C. M. Meenakshi and Dr. A. Krishnamoorthy, "Design and Material Optimization of 1.5MW Horizontal Axis Wind Turbine Blades with Natural Fiber Reinforced composites using Finite Element Method.", International Journal of Electronics, Electrical and Computational System, Volume 6, Issue 8 , August 2017, IJEECS ISSN 2348-117X.
[46] Zhang Lanting, "Research on Structural Lay-up Optimum Design of Composite Wind Turbine Blade.", Energy Procedia 14 (2012) 637 – 642; International Conference on Advances in Energy Engineering (ICAEE); doi:10.1016/j.egypro.2011.12.887.
[47] Zhimin Li, Chun Li, Wei Gao and Yulong Wu; "Effect of Lay-up Design on Properties of Wind Turbine Blades." Frontiers of Engineering Mechanics Research; Aug. 2013, Vol. 2 Iss. 3, PP. 63-70.
[48] Naishadh G. Vasjaliya; "Fluid-structure Interaction and Multidisciplinary Design Analysis Optimization of Composite Wind Turbine Blade."; Master Thesis 2013, Embry-Riddle Aeronautical University.
[49] Supeni E.E., Epaarachchi J.A., Islam M.M. and Lau K.T.; "Design of Smart Structures for Wind Turbine Blades." 2nd Malaysian Postgraduate Conference (MPC2012) 7-9 July, Bond University, Gold Coast, Queensland, Australia Editors: M.M. Noor, M.M. Rahman and J. Ismail.
[50] Xin Cai, Jie Zhu,*, Pan Pan and Rongrong Gu; "Structural Optimization Design of Horizontal-Axis Wind Turbine Blades Using a Particle Swarm Optimization Algorithm and Finite Element Method."; Energies 2012, 5, 4683-4696; doi:10.3390/en5114683.
[51] Wen-Hsiang Wu & Wen-Bin Young; "Structural Analysis and Design of the Composite Wind Turbine Blade"; Appl Compos Mater (2012)19:247–257 DOI 10.1007/s10443-011-9193-z.
[52] Gabriel Saiz," Turbomachinery Aeroelasticity Using a Time-Linearised Multi Blade-row Approach" A thesis of Doctor of Philosophy-University of London Imperial College of Science, Technology and Medicine Department of Mechanical Engineering
[53] Bisplinghoff, R. L., Ashley, H., and Halfman, R. L., Aeroelasticity. 1955: Dover
[54] Drishtysingh Ramdenee, Adrian Ilinca and Ion Sorin Minea," Aeroelasticity of Wind Turbines Blades Using Numerical Simulation" http://dx.doi.org/10.5772/52281

[55] Fouad Mohammad Mohammad "Linear and non-linear deformations of a wind turbine blade considering warping and all aeroelastic load couplings"Doctoral dissertation submitted to of Wayne State University, Detroit, Michigan, 2012.
[56] Alexander McFarlane, B.Eng.;" An Algorithm for Preliminary Aeroelastic Analysis of Composite Wind Turbine Blades."; Master Thesis 2015; Carleton University Ottawa, Ontario.
[57] Ramesh Kumar and K. V. Nagendra Gopal; "CFD-FEA Coupled Simulation of the Dynamic Aeroelastic Response of a Large Scale Horizontal Axis Wind Turbine Rotor."; The Eighth Asia-Pacific Conference on Wind Engineering, December 10–14, 2013, Chennai, India; . ISBN: 978-981-07-8011-1 doi:10.3850/978-981-07-8012-8 267.
[58] Mesfin Belayneh Ageze, Yefa Hu and Huachun Wu1; "Wind Turbine Aeroelastic Modeling: Basics and Cutting Edge Trends."; Hindawi, International Journal of Aerospace Engineering, Volume 2017, Article ID 5263897, https://doi.org/10.1155/2017/5263897.
[59] Mauwafak A. Tawfik, Mohammed I. Abu-Tabikh and Farouk O.Hamdoon; "Aeroelastic Behavior of a Wind Turbine Blade by a Fluid -Structure Interaction Analysis."; Al-Khwarizmi Engineering Journal, Vol. 9, No. 3, P.P. 15- 25 (2013).
[60] Yi-Bao Chen 1, Zhi-Kui Wang 2, Gwo-Chung Tsai; "Two-way Fluid-Structure Interaction Simulation of a Micro Horizontal Axis Wind Turbine."; International Journal of Engineering and Technology Innovation, vol. 5, no. 1, 2015, pp. 33-44.
[61] Lin Wang, Robin Quant and Athanasios Kolios; "Fluid structure interaction modelling of horizontal-axis wind 1 turbine blades based on CFD and FEA."; Journal of Wind Engineering and Industrial Aerodynamic, November 2016, DOI: 10. 1016/j.jweia.2016.09.006.
[62] Kyoungsoo Lee, Ziaul Huque, Raghava Kommalapati, and Sang-Eul Han; "The Evaluation of Aerodynamic Interaction of Wind Blade Using Fluid Structure Interaction Method."; Journal of Clean Energy Technologies, Vol. 3, DOI: 10.7763/JOCET.2015.V3.207.
[63] Dong-Hyun Kim and Yoo-Han Kim; "Performance Prediction of a 5MW Wind Turbine Blade Considering Aeroelastic Effect."; International Scholarly and Scientific Research & Innovation 5(9) 2011; 1855; ISNI:0000000091950263.
[64] P.J. Moriarty, A. C. Hansen; "AeroDyn Theory Manual" Technical Report National Renewable Energy Laboratory; January 2005; NREL/TP-500-36881.
[65] Halldor Albertsson, Daniel Molnar "Optimization for Initial Design of Horizontal Axis Wind Turbines"; Master Thesis, Aalborg University; Spring 2017.
[66] Munson, B. R., T. H. Okiishi, W. W. Huebsch, and A. P. Rothmayer (2015). "Fluid Mechanics" (Seventh Edition). John Wiley & Sons. ISBN: 978-81-265-5343-3. 37
[67] Martin O. L. Hansen (2015). "Aerodynamics of Wind Turbines" (Third Edition). Taylor & Francis Group. ISBN: 978-1-138-77507-7 (hardbook), ISBN: 978-1-315-76998-1 (ebook)
[68] J. F. Manwell, J. G. McGowan and A. L. Rogers (2009). "Wind Energy Explained-Theory, Design and Application" (Second edition). John Wiley & Sons. ISBN: 978-0-470-01500-1 (Hbk)
[69] J. Jucha. "Time-Symmetry Breaking in Turbulent Multi-Particle Dispersion". Springer International Publishing Switzerland (2015). Springer Theses, DOI 10.1007/978-3-319-19192-8_2
[70] G. K. Batchelor. "An Introduction to Fluid Dynamics". Cambridge Univ.Press.Cambridge, England. (1967).
[71] J. O. Hinze. "Turbulence." McGraw-Hill Publishing Co., New York. 1975.
[72] "ANSYS Fluent Theory Guide." Release 18.2. August 2017.
[73] Fluent, ANSYS FLUENT 12.0, Tutorial 9-11-12-23-28-29. Turbulence and Discrete Phase Modeling.
[74] D. C. wilcox. "Turbulence Modeling for CFD". DCW Industries, Inc. La Canada, California. (1198)

[75] F. R. Menter. “Two-Equation Eddy-Viscosity Turbulence Models for Engineering Applications”. AIAA Journal. 32(8). 1598-1605. August 1994
[76] F. R. Menter. “Review of the SST Turbulence Model Experience from an Industrial perspective”. International Journal of Computational Fluid Dynamics. Volume 23, Issue 4. 2009
[77] Ever J. Barbero (2018). “Introduction Composite Materials Design” (Third Edition). Taylor & Francis Group. ISBN: 9781138196803 (hardback), ISBN: 9781315296494 (ebook)
[78] K. Kaw. “Mechanics of Composite Materials”. Second Edition, 2006, Taylor& Francis Group,LLC
[79] “ANSYS Mechanical APDL Theory Reference”. Release 18.2. August 2017.
[80] N. M. Newmark. “Method of Computation for Structural Dynamics”. ASCE Journal of Engineering Mechanics Division. Vol. 85. 67-94. 1959.
[81] J. Chung and G. M. Hulbert. “A Time Integration Algorithm for Structural Dynamics with Improved Numerical Dissipation: The Generalized-α method”. Journal of Applied Mechanics. Vol. 60. 371. 1993.
[82] W. L. Wood, M. Bossak, and O. C. Zienkiewicz. “An Alpha Modification of Newmark Method”. International Journal of Numerical Method in Engineering. Vol. 15.p1562. 1981.
[83] H. M. Hilber, T. J. R. Hughes, and R. l. Taylor. “Improved Numerical Dissipation for Time Integration Algorithm in Structural Dynamics”. Earthquake Engineering and Structural Dynamics. Vol. 5. 283. 1977.
[84] Somers, D. M. 1997, "Design and experimental results for the S809 airfoil", NREL/SR-440-6918 UC Category: 1213 DE97000206.
[85] Giguere, P., Selig, M. S., & Tangler, J. L. 1999, "Blade design trade-off using low lift airfoils for stall regulated HWATs", Journal of Solar Energy Engineerng, vol.121, pp. 217-223.
[86] Tangler, J. L., Somers, D. M., United States., National Renewable Energy Laboratory (U.S.), & Airfoils Incorporated. (1995). *NREL airfoil families for HAWTs*. Golden, Colo: National Renewable Energy Laboratory.
[87] "Wind Turbine Airfoils." Wind Turbine Airfoils. Web. 23 Nov. 2013. <http://wind.nrel.gov/airfoils/>.
[88] Naishadh G. Vasjaliya, Sathya N. Gangadharan, (Aero-Structural Design Optimization of Composite Wind Turbine Blade), Embry-Riddle Aeronautical University
[89] http://help.autodesk.com/view/ACMPDS/2016/ENU/?guid=GUID-2B4538D7-227F-4C9F-891F-785F90CA10CA.
[90] www.dept.aoe.vt.edu/~aborgolt/aoe3054/manual/expt5/D638.38935.pdf
[91] N. A. Fleck, R. A. Smith, Powder Metall., 24 (1981) 121.
[92] X. G. Chen, S. Engler, Amer. Foundry Soc. Trans., 92-94 (1993) 673.
[93] S. Filipović, N. Obradović, S. Marković, A. Đorđević, I. Balać, A. Dapčević, J. Rogan, V. B. Pavlović, Sci. Sinter., 50 (2018) 409.
[94] J. Hashim, Journal Teknolog., 31 (1999) 1.
[95] P. K. Ghosh, S. Ray, J. Mater. Sci., 22 (1987) 4077.
[96] J. J. Lewandowski, C. Liu, W. H. Hunt, Mat. Sci. Eng. A, 107 (1989) 241.
[97] K. Miyake, Y. Hirata, T. Shimonosono, S. Sameshima, Materials, *11* (2018) 1137.
[98] R. Garrett, P. Abhay, A. D. Panagiotis., Biomaterials, 27 (2006) 2651.
[99] Nielsen LF., Mater. and Struct., 31 (1998) 651.
[100] L. Wang, K.K. Tseng, J. Mater. Sci., 38 (2003) 3019.
[101] I. Balać, K. Colić, M. Milovancević, P. Uskoković, M. Zrilić, FME Trans., 40 (2012) 81.
[102] E. Weissenbek, H.J. Bohm, F.G. Rammerstorfer, Comp. Mater. Sci., 3 (1994) 263.
[103] E. Abdulrazag, I. Balać, K. Colić, A. Grbović, M. Milovancević, M. Jelić, Sci. Sint., 51 (2019) 153.

[104] Dj. Veljović, R. Jančić-Hajneman, I. Balać, B. Jokić, S. Putić, R. Petrović, Dj. Janaćković, Ceram. Int., 37 (2011) 471
[105] C. Xujiang, Q.Lehua, T. Wenlong, H.Xianghui, M.WenJing, L. Hejun, Comp. B 136 (2018) 72–80.
[106] M. M. Hand, D. Simms, L. Fingersh, D. Jager, J. Cotrell, S. Schreck, et al., Unsteady aerodynamics experiment phase VI: wind tunnel test configurations and available data campaigns: National Renewable Energy Laboratory Golden, Colorado, USA, 2001.
[107] http://www.arising.com.au/aviation/windturbines/wind-turbine.html; accessed on 01-06-2016.
[108] F. R. Menter, "Zonal two equation k-turbulence models for aerodynamic flows," *AIAA paper,* 731 vol. 2906, p. 1993, 1993.
[109] W. Jones and B. Launder, "The prediction of laminarization with a two-equation model of 733 turbulence," *International journal of heat and mass transfer,* vol. 15, pp. 301-314, 1972.
[110] D. Wilcox and F. by Institutions, "Formulation of the k-omega Turbulence Model Revisited."
[111] Galdamez, R. G., Ferguson, D. M., & Gutierrez, J. R. (2011). Winglet Design and Analysis for Wind Turbine Rotor Blades 100% Report. Bachelors Report, Florida International University.
[112] Brandon Burnett, "COUPLED FLUID-STRUCTURE INTERACTION MODELING OF A PARAFOIL", Master of Science in Aerospace Engineering, Faculty Of Embry-Riddle Aeronautical University, December 2016.
[113] Zorana B. Trivković. "Multi-objective Optimization of Composite Wind Turbine Blades", Doctoral Dissertation, Mechanical Engineering Faculty, Belgrade University, 2019.

Прилог 1.

Изјава о ауторству

Потписани-а Мохамед Абдуљавад Хигаег

број индекса D10/2016

Изјављујем

да је докторска дисертација под насловом

Оптимизација композитне лопатице ветротурбине са хоризонталном осовином на основу анализе интеракције флуида и структуре

- резултат сопственог истраживачког рада,
- да предложена дисертација у целини ни у деловима није била предложена за добијање било које дипломе према студијским програмима других високошколских установа,
- да су резултати коректно наведени и
- да нисам кршио/ла ауторска права и користио интелектуалну својину других лица.

Потпис докторанда

У Београду, 14.02.2020

Изјава о истоветности штампане и електронске верзије докторског рада

Име и презиме аутора _____Мохамед Абдуљавад Хигаег_____

Број индекса _____D10/2016_____

Студијски програм _____докторске студије_____

Наслов рада ___Оптимизација композитне лопатице ветротурбине са хоризонталном осовином на основу анализе интеракције флуида и структуре__

Ментор _____Проф. др Александар Грбовић_____

Изјављујем да је штампана верзија мог докторског рада истоветна електронској верзији коју сам предао/ла ради похрањена у **Дигиталном репозиторијуму Универзитета у Београду.**

Дозвољавам да се објаве моји лични подаци везани за добијање академског назива доктора наука, као што су име и презиме, година и место рођења и датум одбране рада.

Ови лични подаци могу се објавити на мрежним страницама дигиталне библиотеке, у електронском каталогу и у публикацијама Универзитета у Београду.

Потпис аутора

У Београду, _____14.02.2020._____

_____

Прилог 3.

Изјава о коришћењу

Овлашћујем Универзитетску библиотеку „Светозар Марковић“ да у Дигитални репозиторијум Универзитета у Београду унесе моју докторску дисертацију под насловом:

___Оптимизација композитне лопатице ветротурбине са хоризонталном осовином на основу анализе интеракције флуида и структуре__

која је моје ауторско дело.

Дисертацију са свим прилозима предао/ла сам у електронском формату погодном за трајно архивирање.

Моју докторску дисертацију похрањену у Дигитални репозиторијум Универзитета у Београду могу да користе сви који поштују одредбе садржане у одабраном типу лиценце Креативне заједнице (Creative Commons) за коју сам се одлучио/ла.

1. Ауторство

2. Ауторство - некомерцијално

3. Ауторство – некомерцијално – без прераде

4. Ауторство – некомерцијално – делити под истим условима

5. Ауторство – без прераде

6. Ауторство – делити под истим условима

(Молимо да заокружите само једну од шест понуђених лиценци, кратак опис лиценци дат је на полеђини листа).

Потпис докторанда

У Београду, ___14.02.2020_____

_____

1. Ауторство - Дозвољавате умножавање, дистрибуцију и јавно саопштавање дела, и прераде, ако се наведе име аутора на начин одређен од стране аутора или даваоца лиценце, чак и у комерцијалне сврхе. Ово је најслободнија од свих лиценци.

2. Ауторство – некомерцијално. Дозвољавате умножавање, дистрибуцију и јавно саопштавање дела, и прераде, ако се наведе име аутора на начин одређен од стране аутора или даваоца лиценце. Ова лиценца не дозвољава комерцијалну употребу дела.

3. Ауторство - некомерцијално – без прераде. Дозвољавате умножавање, дистрибуцију и јавно саопштавање дела, без промена, преобликовања или употребе дела у свом делу, ако се наведе име аутора на начин одређен од стране аутора или даваоца лиценце. Ова лиценца не дозвољава комерцијалну употребу дела. У односу на све остале лиценце, овом лиценцом се ограничава највећи обим права коришћења дела.

4. Ауторство - некомерцијално – делити под истим условима. Дозвољавате умножавање, дистрибуцију и јавно саопштавање дела, и прераде, ако се наведе име аутора на начин одређен од стране аутора или даваоца лиценце и ако се прерада дистрибуира под истом или сличном лиценцом. Ова лиценца не дозвољава комерцијалну употребу дела и прерада.

5. Ауторство – без прераде. Дозвољавате умножавање, дистрибуцију и јавно саопштавање дела, без промена, преобликовања или употребе дела у свом делу, ако се наведе име аутора на начин одређен од стране аутора или даваоца лиценце. Ова лиценца дозвољава комерцијалну употребу дела.

6. Ауторство - делити под истим условима. Дозвољавате умножавање, дистрибуцију и јавно саопштавање дела, и прераде, ако се наведе име аутора на начин одређен од стране аутора или даваоца лиценце и ако се прерада дистрибуира под истом или сличном лиценцом. Ова лиценца дозвољава комерцијалну употребу дела и прерада. Слична је софтверским лиценцама, односно лиценцама отвореног кода.